Summer 2011

Interface Circuit for a Multiple-Beam Tuning-Fork Gyroscope with High Quality Factors

Ren Wang
Old Dominion University

INTERFACE CIRCUIT FOR A MULTIPLE-BEAM TUNING-FORK GYROSCOPE WITH HIGH QUALITY FACTORS

by

Ren Wang
B.S. August 2004, Wuhan University, China
M.S. August 2006, Delft University of Technology, Netherlands

A Dissertation Submitted to the Faculty of
Old Dominion University in Partial Fulfillment of the
Requirement for the Degree of

DOCTOR OF PHILOSOPHY

MECHANICAL ENGINEERING

OLD DOMINION UNIVERSITY
August 2011

Approved by:

Julie Hao (Director)

Shirshak Dhali (Member)

Ali Beskok (Member)

Keejoo Lee (Member)

ABSTRACT

INTERFACE CIRCUIT FOR A MULTIPLE-BEAM TUNING-FORK GYROSCOPE WITH HIGH QUALITY FACTORS

Ren Wang
Old Dominion University, 2011
Director: Dr. Julie Hao

This research work presents the design, theoretical analysis, fabrication, interface electronics, and experimental results of a Silicon-On-Insulator (SOI) based Multiple-Beam Tuning-Fork Gyroscope (MB-TFG). Based on a numerical model of Thermo-Elastic Damping (TED), a Multiple-Beam Tuning-Fork Structure (MB-TFS) is designed with high Quality factors (Qs) in its two operation modes. A comprehensive theoretical analysis of the MB-TFG design is conducted to relate the design parameters to its operation parameters and further performance parameters. In conjunction with a mask that defines the device through trenches to alleviate severe fabrication effect on anchor loss, a simple one-mask fabrication process is employed to implement this MB-TFG design on SOI wafers. The fabricated MB-TFGs are tested with PCB-level interface electronics and a thorough comparison between the experimental results and a theoretical analysis is conducted to verify the MB-TFG design and accurately interpret the measured performance. The highest measured Qs of the fabricated MB-TFGs in vacuum are 255,000 in the drive-mode and 103,000 in the sense-mode, at a frequency of 15.7kHz. Under a frequency difference of 4Hz between the two modes (operation frequency is 16.8kHz) and a drive-mode vibration amplitude of 3.0μm, the measured rate sensitivity is 80μV_{PP}/°/s with an equivalent impedance of 6MΩ. The calculated overall rate resolution of this device is 0.37°/hr/√Hz, while the measured Angle Random Walk (ARW) and bias

instability are 6.67°/√hr and 95°/hr, respectively.

This thesis is dedicated to my parents.

ACKNOWLEDGMENTS

First I would like to express my sincere and utmost gratitude to my Ph.D. advisor Dr. Julie Zhili Hao, for offering me this excellent opportunity in graduate research. Her insightful observations and incisive questions have guided me throughout the course of my Ph.D. work. I am also grateful to her for providing me with all the valuable resources in the experimental work.

I would like to thank Dr. Shirshak Dhali, Dr. Ali Beskok and Dr. Keejoo Lee for taking an interest in my work and serving on my Ph.D. dissertation committee. It has been a privilege to benefit from their feedback and advice in the construction of my dissertation. I am very grateful to Dr. J. K. Huang and Dr. Gene Hou for their continuous support in my graduate research. Also, many thanks go to Diane Mitchell and June Blount for all their administrative help.

I would like to express my appreciation to the members of the entire MEMS group, both past and present, for their help and useful discussions. Thanks go to Peng, Fei, Yujie and Wenting, for providing a friendly and stimulating atmosphere in research, as well as brightening the long hours spent in the lab.

I would like to give my special thanks to He Chong, whose patience, support and encouragement pulled me through my graduate studies here at ODU.

Finally, I owe my deepest gratitude to my parents. Over the years in my life, I have learnt academic lessons from school, and more importantly, life lessons from my parents. Without their understanding and support, I couldn't have gone this far in my academic pursuit. To them, I owe everything.

TABLE OF CONTENTS

Page

LIST OF TABLES

LIST OF FIGURES

CHAPTER I

INTRODUCTION TO MEMS GYROSCOPES

A gyroscope, by definition, is a sensor that can measure an angular rate or velocity. Traditional spinning wheel gyroscopes that are based on the conservation of angular momentum were widely used in the past century. Optical gyroscopes, which are most commonly ring laser gyroscopes, are a great improvement to the spinning gyroscopes because of their great reliability, relatively small size and weight, as well as no wear [1]. In more recent years, with the advent of the micromachining technology, Micro-Electromechanical System (MEMS) gyroscopes have emerged and proven to be advantageous over traditional macro-scale gyroscopes.

The technology used to implement the MEMS gyroscope is crucial considering a MEMS gyroscope system needs to combine the mechanical element with its interface circuit in a compact way. Since there are no rotating parts or bearings in a MEMS gyroscope, it can be inexpensively batch-fabricated for potential integration with Complementary Metal-Oxide-Semiconductor (CMOS) electronics [2], thus making a MEMS gyroscope sensor possible. In this work, a MEMS gyroscope with its interface circuit is designed and the implemented angular rate senor is evaluated for its performance.

1.1 Applications of MEMS Gyroscopes

MEMS gyroscopes are an important type of silicon-based sensors used for angular velocity measurement. Because of their small size, low cost, low power consumption and

the capability of integration with electronics, they have been used in a wide range of applications, and therefore become one of the fastest growing market segments in the micro-sensor industry.

Micromachined gyroscopes are traditionally used in the automobile industry for anti-skid control, rollover detection and Anti-lock Brake Systems (ABS). Applications in the consumer electronics field include Global Positioning System (GPS) navigation, image stabilization in digital cameras, gaming and inertial pointing devices. The consumer electronics is a field with great potential and some of the major commercial manufacturers are ST Microelectronics, Analog Devices, InvenSense and Honeywell. Fig. 1.1 illustrates a MEMS gyroscope from ST Microelectronics and its size comparing to a quarter dollar.

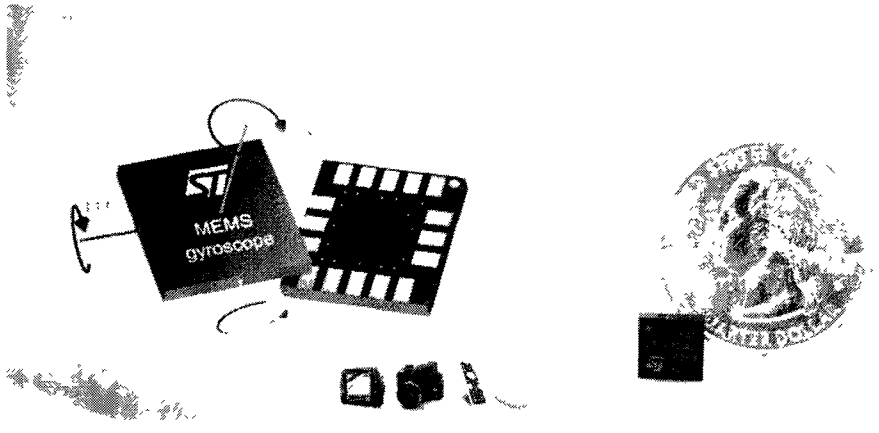

Figure 1.1: A commercial MEMS gyroscope from ST Microelectronics

Ever since its invention, the gyroscope has always been an integral part of all the Inertial Measurement Units (IMU) and Inertial Navigation Systems (INS). Inertial navigation is performed to determine the space position of a subject by using

accelerometers and gyroscopes installed on the subject. The measured acceleration and rotation rate can be combined to yield the accurate position of the subject in space [3]. The IMU is an independent system that can perform accurate short-term navigation of an object in the absence of GPS assisted inertial navigation [4]. It typically contains three accelerometers and three gyroscopes that are placed along their respective sensitive axes to gather information about the object's direction and heading. IMUs are very important components in aircrafts, unmanned vehicles, GPS augmented navigation, etc. In the petroleum industry, a high precision IMU is needed in down-hole electronics for real-time monitoring and correction of drilling in offshore rigs.

In general, MEMS gyroscopes can be classified into three different categories based on their performance: rate-grade, tactical grade, and inertial-grade gyroscopes. Table 1.1 summarizes the requirements for each of these categories. In the past, much effort had been dedicated to developing micromachined silicon gyroscopes of the rate-grade, primarily because of their use in automotive applications. Nowadays, the majority of applications in consumer electronics also fall into this category, while the higher precision tactical-grade and inertial-grade devices are needed in aerospace, military and petroleum industry.

Table 1.1: Performance requirements for gyroscopes of different categories

Parameter	Rate Grade	Tactical Grade	Inertial Grade
Angle Random Walk, °/√h	>0.5	0.5-0.05	<0.001
Bias Drift, °/h	10-1000	0.1-10	<0.01
Scale Factor Accuracy, %	0.1-1	0.01-0.1	<0.001
Full Scale Range (°/sec)	50-1000	>500	>400
Max. Shock in 1msec, g's	10^3	10^3-10^4	10^3
Bandwidth, Hz	>70	~100	~1-100

The most commonly used high precision (tactical-grade and inertial-grade) gyroscopes are Fiber-Optic Gyroscopes (FOG), Ring-Laser Gyroscopes (RLG) and the Hemispherical Resonator Gyroscope (HRG). Although FOGs and RLGs have higher accuracy, they are comparatively bulky and expensive gyroscopes that rely on optical means to detect rotation. Thus, they cannot be micromachined or integrated with CMOS ICs, which makes them inappropriate for small form-factor sensors. HRGs use mechanical means for rotation detection, but have a bulky quartz-based structure which is not suitable in ultra low-power applications [3]. Given all these limitations of the above-mentioned high precision gyroscopes, ongoing research has been conducted to investigate low-cost and low-power MEMS gyroscopes targeting at tactical or inertial grade performance. The work done at Georgia Institute of Technology in 2007 showed a mode-matched tuning-fork gyroscope with a 0.1°/hr bias stability, which was two orders of magnitude better than commercially available MEMS gyroscopes at that time.

1.2 Coriolis Effect

Known as the Coriolis Vibratory Gyroscopes (CVG) [5], MEMS gyroscopes are based on the Coriolis Effect, where vibration energy of a microstructure is transferred from one vibration mode (drive mode) to another (sense mode) in response to an input rotation rate signal. The two vibration modes are orthogonal to the axis of rotation and to each other. Fig. 1.2 illustrates the Coriolis Effect conceptually. Coriolis Acceleration arises in a rotating reference frame and is proportional to the rate of rotation. In the example of a simple tuning fork, as shown in Fig. 1.3, the tines of the tuning fork are driven into resonance along the x-axis and this vibration mode is called as the drive mode. At the

same time when the tuning fork is rotated around the z-axis with a rotation rate of $\overrightarrow{\Omega_z}$, there will be a force applied on the tines causing them to deflect along the y-axis with an acceleration equal to $2\overrightarrow{v_x} \times \overrightarrow{\Omega_z}$, where $\overrightarrow{v_x}$ is the velocity of the tines along the x-axis. This force is referred to as the Coriolis Force and the resulting deflection of the tines along the y-axis is referred to as the sense mode. The deflection in the sense mode is proportional to the input rotation rate and it will lead to an output voltage signal, based on which the input rotation rate can be told.

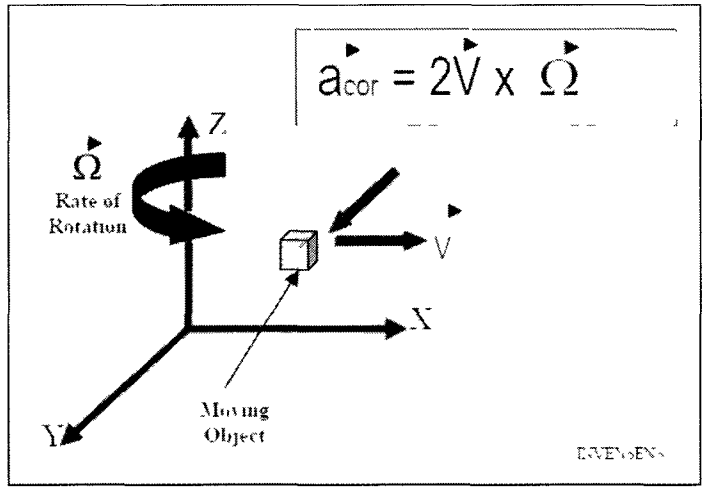

Figure 1.2 [6]: Concept of Coriolis Effect

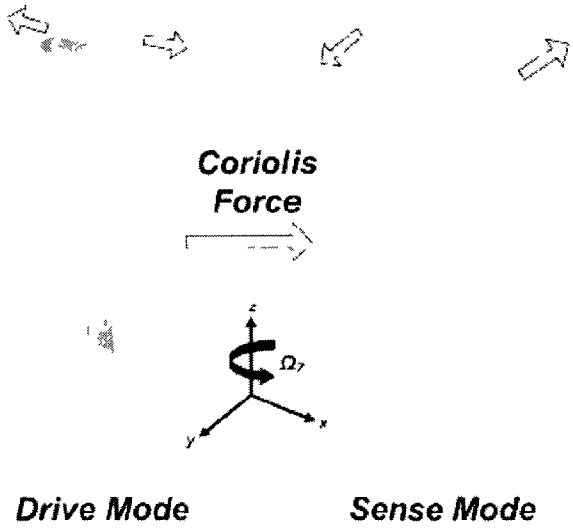

Figure 1.3: Tuning fork demonstration of Coriolis Force

Vibratory gyroscopes can work either in matched-mode or split-mode condition [7]. In this work, only matched-mode gyroscopes are investigated because in a matched-mode condition, the resonant frequencies of the drive mode and the sense mode are identical or in close proximity so that the rotation-induced Coriolis Signal can be amplified by the mechanical Quality (Q) factor of the sense mode, resulting in higher rate sensitivity and better resolution than in the split-mode condition.

1.3 Motivation

While the MEMS gyroscopes have smaller size and weight and are much more cost-effective, they have yet to break into the high-precision market currently dominated by the bulky mechanical and optical gyroscopes. The survey in Table 1.2 demonstrates the performance differences between two categories of gyroscopes manufactured by Honeywell. The GG1320AN [8] is a single-axis RLG with a variety of military

applications, while the GG5300 [9] is a three-axis MEMS rate gyroscope for pointing, stabilization and guidance applications.

Table 1.2: Performance comparison between Honeywell's RLG and MEMS gyroscopes

Specifications	GG1320AN (RLG)	GG5300 (MEMS)
Size	Height: 4.5cm Diameter: 8.8cm	Height: 3.3cm Diameter: 5.1cm
Weight	454g	136g
Start-up time	1~4s	<1s
Bias stability	0.0035deg/hr	<70deg/hr
Angle random walk (Noise)	0.0035deg/root hr	<0.2deg/root hr
Bandwidth	1000Hz	100Hz

Apparently, the performance of the MEMS gyroscope GG5300 is a few orders of magnitude away from that of the RLG GG1320AN in terms of bias stability and noise, which dictates their different application fields. One objective of this research work is to present a comprehensive theoretical and practical analysis of the design and performance evaluation of a MEMS gyroscope system, which lays the foundation and provides some insight on how to improve MEMS gyroscopes so as to approach high precision performances.

Among various kinds of MEMS gyroscopes, the tuning-fork gyroscope has drawn a lot of interest because of its promising design features for high precision performance and relative ease with fabrication [2, 10]. One of the first micromachined tuning-fork gyroscopes was demonstrated by Draper Laboratory in the early 1990s [11], which had a resolution of 5000°/hr a nd a rate sensitivity of 1.57mV/°/sec. In 1997, Draper Lab improved the resolution to 25°/hr [12]. Analog Devices Inc. developed a single-chip integrated tuning-fork gyroscope in 2002. Its measured results showed a resolution of

50°/hr and a rate sensitivity of 12.5mV/°/sec [13]. Since 2004, the Integrated MEMS laboratory at Georgia Institute of Technology has reported a series of works on the silicon-on-insulator (SOI) mode-matched tuning-fork gyroscope with the device thickness varying from 40μm to 60μm [14-16]. The highest rate sensitivity and the best bias stability reported from these were 88mV/°/sec and 0.15°/hr, respectively, in 2008.

The key performance parameters of a MEMS gyroscope include the rate resolution, rate sensitivity (or scale factor), bias drift (or bias stability), and operation bandwidth. Many tradeoffs exist in a gyroscope design for these parameters. For instance, high Quality factors in the two vibration modes and matched-mode operation are critical for a tuning-fork gyroscope to achieve high performance [10, 17-19], including high rate sensitivity, improved rate resolution, and lower bias drift. Therefore, tuning-fork gyroscopes with high Qs and matched-mode operation have been pursued. However, such high performance is typically obtained with a narrow operation bandwidth [17]. In contrast, a tuning-fork gyroscope with a wide operation bandwidth usually needs to sacrifice its rate sensitivity and bias drift [19, 20].

In pursuit of high performance, another objective of this research work is to fabricate tuning-fork gyroscopes with ultra-high Qs, and to design and implement the interface electronics for operating them. Comparing to the reported drive-mode Q of 81k and sense-mode Q of 64k in [14], and drive-mode Q of 67k and sense-mode Q of 125k in [19], the quality factors in this work are expected to be typically over 200k for drive mode and 100k for sense mode. In conjunction with its interface circuit, the fabricated tuning-fork gyroscope makes an angular rate sensor, of which the overall performance is characterized in detail.

1.4 Dissertation Organization

The remainder of this dissertation is organized as follows.

Chapter 2 presents an overview of the MEMS tuning-fork gyroscope itself. It provides fundamentals of this gyroscope device including its operation principle, performance specifications and theoretical model analysis. Design challenges such as quadrature error and mode-matching are also elaborated.

Chapter 3 focuses on the fabrication process of the tuning-fork gyroscope. Only a single mask is used and the fabricated devices prove to be very robust. The simple two-step process, namely DRIE and HF acid etching, is discussed in detail. One noteworthy improvement of the fabrication mask is to add a trench feature surrounding the gyroscope in order to significantly increase its quality factors in both operation modes.

Chapter 4 discusses the interface circuit design for the tuning-fork gyroscope. The interface circuit consists of a drive loop for electrostatic actuation of the gyroscope, and a sense channel for capacitive sensing of the gyroscope output. In the context of gyroscope interfacing, the Transimpedance Amplifier (TIA) is proposed as a low-noise front-end for motional current detection in this gyroscope. The drive loop circuitry is based on a series resonant electromechanical oscillator approach and the sense channel utilizes a synchronous demodulator.

Chapter 5 presents Printed Circuit Board (PCB) implementation of the drive and sense electronics for the tuning-fork gyroscope. A gyro-mounted PCB in vacuum is evaluated for its performance as an angular rate sensor. Frequency characterization results are provided to confirm the ultra-high Qs in both operation modes of the

gyroscope. The rate sensitivity measurement is then performed to demonstrate this important behavior of the gyroscope.

Chapter 6 provides a detailed analysis of bias drift in micromachined gyroscopes. Bias drift and angle random walk, which represent the overall system resolution, have become the two vital performance parameters in MEMS-based Inertial Measurement Units (IMU) such as gyroscopes. An important technique for characterizing the bias drift, Allan Variance, is introduced. The bias drift of the micro-system implemented here is compared with results from other research work.

At last, Chapter 7 concludes this work with an overview of the contributions of this research and proposes possible future directions in performance optimization of this tuning-fork gyroscope.

CHAPTER II

TUNING-FORK GYROSCOPE FUNDAMENTALS

This chapter discusses the basics of the tuning-fork gyroscope including its operation principle and performance parameters. Since the fundamental knowledge for any Coriolis Vibratory Gyroscope (CVG) remains the same [3], the analyses here for tuning-fork gyroscopes, with slight modifications if any, can be applied to other CVGs as well.

2.1 Operation Principle

Fig. 2.1 shows a SEM picture of the multiple-beam tuning-fork gyroscope (MB-TFG) design for z-axis rotation detection. The multiple-beam tuning-fork structure (MB-TFS) consists of two large proof masses and a flexural structure of four beams in parallel. The flexural structure functions as mechanical springs along the x-axis and the y-axis. The whole structure is fixed on the substrate through the anchor located at its center. A collection of electrodes is distributed around the proof masses for operating this device. The MB-TFG here uses electrostatic actuation and capacitive sensing. Comb-drive electrodes are placed at both sides of the MB-TFS for electrostatic actuation, while parallel-plate sense electrodes surround the two proof-masses for capacitive sensing. In addition, tuning electrodes are also incorporated like in the micromachined gyroscope reported in [14]. The tuning electrodes are exactly the same in size, but serve a different purpose as the sense electrodes, as will be explained later.

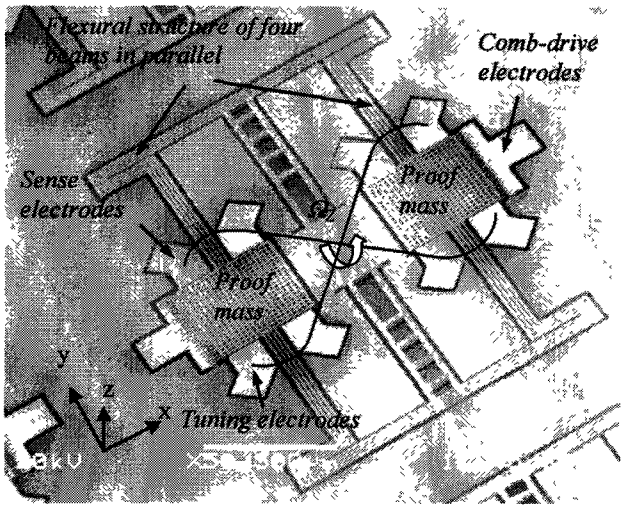

Figure 2.1: A SEM picture of the multiple-beam tuning-fork gyroscope (MB-TFG) design

As previously mentioned, the operating principle of this gyroscope is based on Coriolis Effect and the two proof-masses function as the tines of a tuning fork, hence the name "tuning-fork gyroscope". The MB-TFS is operated in two in-plane vibration modes: one along the x-axis (drive-mode) and the other along the y-axis (sense-mode). A constant DC polarization voltage, V_P, is applied to the anchor and the whole MB-TFS. This DC voltage is the bias voltage for the gyroscope. Comb-drive electrodes are employed to establish in-plane vibrations in the drive-mode, while a rotation rate signal, Ω_Z, normal to the device plane (z-axis) induces a Coriolis Acceleration along the y-axis and excites in-plane vibrations in the sense-mode. Fig. 2.2 illustrates the two vibration modes simulated in COMSOL Multiphysics. Note that the two vibration modes are orthogonal and the two proof-masses vibrate in opposite directions in both vibration modes.

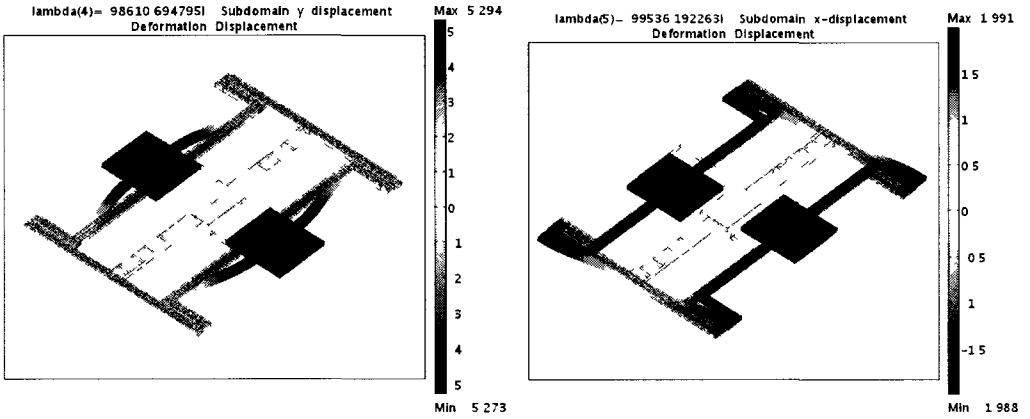

Figure 2.2: COMSOL simulation of two vibration modes of a multiple-beam tuning-fork structure (MB-TFS) (a) drive-mode and (b) sense-mode

Mathematically, the magnitude of the Coriolis Acceleration is given by the cross product of the velocity of the proof-masses in the drive-mode and the input rotation rate. If the proof-masses, when driven into resonance in the drive-mode, are in sinusoidal oscillation, which is given by $q_d \sin(\omega_x t)$, then the Coriolis Acceleration is

$$a_y = 2\Omega_z(t)v_x(t) = 2\Omega_z(t)q_d\omega_x \cos(\omega_x t) \tag{2.1}$$

where Ω_z is the z-axis input rotation rate, v_x is the drive-mode velocity of the proof-masses, q_d is the amplitude of oscillation in the drive-mode and ω_x is the drive-mode resonant frequency. This expression shows that the Coriolis Acceleration generated in the CVG is an Amplitude Modulated (AM) sinusoid signal in which the drive-mode velocity serves as the carrier signal and the rotation rate signal is the modulating signal.

The rotation-induced vibration in the sense-mode causes the gap between the parallel-plate electrode and the proof-mass to change. This capacitive gap change is proportional to the input rotation rate and can be detected by measuring the generated current as a

result of this parallel-plate capacitance change. Because of its amplitude-modulated characteristic, the measured output from the four parallel-plate sense electrodes along the y-axis needs to be demodulated in the sense channel in order to extract the final output that is proportional to the input rotation rate Ω_z.

As will become clear later on, the MB-TFG has maximum rate sensitivity when it is working under perfect matched-mode condition, that is, the resonant frequencies of the drive-mode and sense-mode are identical. Although these frequencies are designed to be the same or very close to each other, due to fabrication variations, there always exists a frequency difference between the two, which usually ranges from 100Hz to 300Hz. To compensate for fabrication variations and increase the rate sensitivity, a DC tuning voltage is applied on the four parallel-plate tuning electrodes shown in Fig. 2.1 to reduce this frequency difference between the drive-mode and the sense-mode, so that the rate sensitivity can be significantly increased, roughly by a factor of the Q in the sense-mode.

2.2 Performance Specifications

A number of different parameters are used to specify the performance of a MB-TFG system. The main performance parameters include resolution, sensitivity (scale factor), bias stability and operation bandwidth.

2.2.1 Resolution

The resolution of a gyroscope is the minimum detectable input rotation rate that can be distinguished from the noise floor of the system per square root of bandwidth of detection. It is usually expressed in units of °/sec/√Hz or °/hr/√Hz. The overall resolution

of a MEMS gyroscope system, which is given by the total noise equivalent rotation (TNEΩ), is determined by two uncorrelated components: the mechanical (Brownian) noise equivalent rotation (MNEΩ) and the electronic noise equivalent rotation (ENEΩ). Their relation is given by Eq. 2.2.

$$TNE\Omega = \sqrt{MNE\Omega^2 + ENE\Omega^2} \tag{2.2}$$

The mechanical noise source for the gyroscope is the Brownian Motion of the tuning-fork structure caused by molecular collisions from the surrounding medium [2]. It can be found by equating the displacement caused by the Brownian Motion to the displacement caused by the Coriolis Force. The mechanical resolution of the gyroscope is given by [21]

$$MNE\Omega = \frac{1}{2q_d}\sqrt{\frac{4k_BT}{\omega_0 M Q_{EFF}}}\sqrt{BW} \times \frac{180^\circ}{\pi} \tag{2.3}$$

where q_d is still the amplitude of oscillation in the drive-mode, k_B is the Boltzmann Constant (1.38×10^{-23}Joules/K), T is the absolute temperature, ω_0 is the resonant frequency of the sensor, M is the effective mass of the tuning-fork structure, Q_{EFF} is the effective quality factor of the gyroscope system and BW is the measurement bandwidth. Obviously, large oscillation amplitudes in the drive-mode, large effective mass and high effective quality factors would all benefit the mechanical resolution. For a given MB-TFS, Q_{EFF} can be maximized by matching the resonant frequencies of the drive-mode and sense-mode. When the two frequencies are very close to each other, the Q in the sense-mode is used as the Q_{EFF} for theoretical performance estimation.

The electronic noise floor depends on the minimum detectable capacitance change of the sense channel interface electronics and the sense capacitive sensitivity to the rotation rate. For a parallel-plate capacitive transducer, the minimum detectable capacitance change is proportional to the input-referred current noise of the interface electronics integrated over the bandwidth of interest [21]. Assuming that a Transimpedance Amplifier (TIA) with feedback impedance R_{TIA} is employed as the front-end interface in the sense channel, then the ENEΩ of the MB-TFG is calculated as

$$ENE\Omega = \frac{d_{S0}\sqrt{4k_BT/R_{TIA}}}{2V_PC_{S0}Q_{EFF}q_d}\sqrt{BW} \tag{2.4}$$

where V_P is the bias voltage for the MB-TFS, d_{S0} and C_{S0} are the static sense gap and static sense capacitance, respectively. It is evident that oscillation amplitude of the drive-mode, effective quality factor and static sense gap all affect the electronic noise floor.

Angle Random Walk (ARW) is more often used to represent the noise floor of a gyroscope. Typically expressed in unit of °/√hr, it is a measure of the angular error buildup with time that is due to the white noise in the angular rate. The ARW and the noise floor per unit bandwidth are related by [3]

$$ARW\left(°/\sqrt{hr}\right) \times 60 \equiv Noise\ floor\left(°/hr/\sqrt{Hz}\right) \tag{2.5}$$

2.2.2 Sensitivity

Coriolis-induced sense-mode deflections of the proof-masses can be detected through capacitive, piezoresistive, piezoelectric or optical means. The sensitivity, also known as scale factor, of a gyroscope is the ratio of the change in the output to a unit change in the

input that is to be measured, typically expressed in volts/°/sec. It measures how sensitive the device is in response to an input rotation rate signal. The MB-TFG in this work uses capacitive detection and the direct output generated at a sense electrode is a motional current given by

$$I_{sense} = \frac{2V_P C_{S0}}{d_{S0}} q_d Q_{EFF} \Omega_z \tag{2.6}$$

where the meanings of the parameters in Eq. 2.6 are the same as above. Note that the input rotation rate information Ω_z is incorporated in this output signal and will be extracted at a later stage.

As mentioned above, in order to amplify and convert the current output from the sense electrodes to a voltage signal, TIA is chosen as the front-end interface in the sense channel for the MB-TFG, primarily because of its immunity to parasitic capacitances at its inverting input and hence reduction of signal loss. The rate sensitivity of the MB-TFG can be calculated as

$$\frac{V_{sense}}{\Omega_z} = \frac{2V_P C_{S0}}{d_{S0}} q_d Q_{EFF} R_{TIA} \tag{2.7}$$

where R_{TIA} is the feedback resistance of the TIA.

Intuitively, for a given input rotation rate, larger deflection in the sense-mode causes larger change in the sense capacitances, generating larger electrical output which leads to higher sensitivity. The sense-mode deflection of the proof-masses is proportional to the oscillation amplitude in the drive-mode q_d and the effective quality factor Q_{EFF}. Furthermore, a high aspect ratio of the capacitive sensing gap allows for large changes in

the sense capacitances. Therefore, all these factors would contribute to a high rate sensitivity, according to Eq. 2.7.

2.2.3 Zero Rate Output and Bias Stability

Zero Rate Output (ZRO) is the output signal from the gyroscope system when there is no input rotation, in other words, zero rate input. The drift of this ZRO bias is a vital performance parameter that determines the long-term stability of a micromachined gyroscope. The term "bias drift" is used interchangeably with another term, bias stability, or instability in some of the literature, and is usually defined in units of °/hr.

To understand the importance of bias drift, consider that in inertial navigation systems, gyroscopes and accelerometers are used together to collect heading information, which is, orientation and position. The rate information obtained from the gyroscope is integrated to give the angle value. To ensure precise angle information, the variation of the ZRO signal must be kept at a minimum level, which otherwise may result in a huge error in angle information. Bias drift, is such an accurate measure of how large the variation in the ZRO is. Nowadays, modern gyroscope systems rely on periodic calibration with GPS to ensure accurate heading information. However, in circumstances such as deep sea navigation and oil exploration, when frequent surfacing to calibrate with a GPS is not possible, long-interval calibration is a must. In such cases, a gyroscope system with lower bias drift can function accurately for a longer time, without the need for calibration.

The bias drift of a gyroscope is comprised of systematic and random components. The systematic components are due to temperature variations, linear accelerations,

vibrations and other environmental factors [5]. The random component depends significantly on the noise floor of the gyroscope and has a 1/f characteristic [3]. Therefore, improvement in gyroscope resolution also results in lower bias drift. An empirical expression to predict the bias drift in gyroscopes is given in [22]

$$Bias\ drift \propto \frac{\omega_0^2}{Q_{Drive} Q_{Sense} Area_{Electrodes}} \tag{2.8}$$

where $Area_{Electrodes}$ is the total capacitive area of all the sense electrodes.

Since bias drift is related to the noise floor of a gyroscope, a Power Spectral Density (PSD) method was used to measure bias drift. However, the Allan Variance Technique has become more common in specifying the bias drift of a gyroscope [5]. Chapter 6 is dedicated to a detailed analysis of bias drift.

2.2.4 Operation Bandwidth

The rate gyroscope used in this dissertation is a CVG operated in the open-loop mode, in which the driven mode is excited and inertial rotation about the input axis results in the excitation of the readout mode. The motion in the readout mode is only monitored but not controlled and the amplitude of the readout-mode vibration is proportional to the input rate [7]. The operation bandwidth of this CVG in the open-loop mode is directly related to the separation of the natural frequencies of the two vibration modes. Also, bandwidth can be regarded as an indicator of how many measurements can be made per second. It reflects the response time required for the system output to take on its new steady-state value after a step change in the input rotation rate. Since the bandwidth is found to be inversely proportional to the effective quality factor (Q_{EFF}) of the system,

larger bandwidths can be achieved either by increasing the system damping, or by further separating the two natural frequencies, both of which would lower Q_{EFF}.

However, there is a tradeoff between bandwidth and sensitivity, since sacrificing Q_{EFF} for more bandwidth apparently results in a smaller steady-state response to a given inertial input rotation rate. The bandwidth requirement for a CVG depends on its application. In gyrocompass navigation where a very high rate resolution is necessary, high Q_{EFF} and, hence, high sensitivity has the priority, so a small bandwidth and a long response time are tolerable. Conversely, in other cases such as the automotive roll-over situation where high yaw rates associated with vehicular skidding need to be detected, minimum response time of the CVG system is crucial and therefore a larger bandwidth is required [3].

2.3 Theoretical Model Analysis

A tuning-fork gyroscope is equivalent to a coupled resonator system and the rotation-induced Coriolis Effect is the coupling element between the two vibration modes - drive and sense modes [23]. Each vibration mode corresponds to a two-port resonator system, which can be driven by an input voltage and outputs a current. The input voltage is converted into a driving force through the drive electrodes, which can either be comb-drive or parallel-plate. The driving force causes the mechanical structure to vibrate and as a result of this vibration, current output can be generated from the capacitive sense electrodes, which also can be comb-drive or parallel-plate, and is picked up by the front-end interface electronics. There is an electromechanical coupling effect at both the

conversions from the input voltage to driving force and from the structure motion to output current.

Newton's Second Law of Motion governs the dynamics of the tuning-fork gyroscope. To analyze the system behavior in each mode, the vibration is excited from input and the signal from output is observed.

2.3.1 Drive Mode

The drive-mode of the MB-TFG relies on comb-drive electrodes on one side for generating electrostatic force to activate the MB-TFS and the output current is detected from the comb-drive electrodes on the other side. Fig. 2.3 shows typical comb-drive structures using Deep Reactive Ion Etching (DRIE) process.

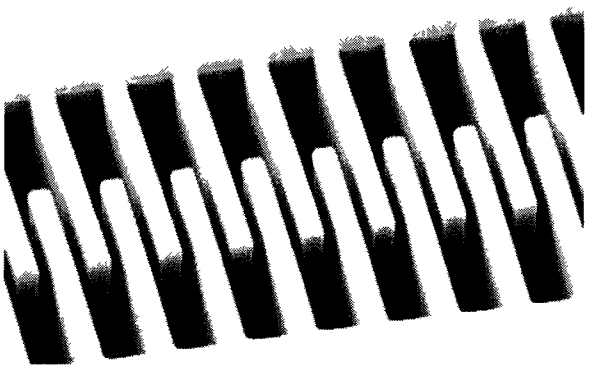

Figure 2.3: DRIE fabricated comb-drive structures

In comb-drive electrodes, one comb structure is fixed while the other one is mobile. When a voltage difference is established be tween these two combs and the mobile electrode is moving so that the overlapping capacitive area of two opposite comb fingers

is changing, electrostatic force is generated along the displacement of the mobile electrode. The derivation of this electrostatic force is based on the stored electrical energy change of a capacitor and its expression is given by

$$F_e = n\varepsilon_0 V^2 \frac{h}{d_d} \tag{2.9}$$

where n is the number of the fingers on one comb electrode, ε_0 is the permittivity of free space (8.85419 x 10^{-12} C^2/Jm), V is the voltage difference, h/d_d is the aspect ratio of the comb fingers, h is the structure thickness and d_d is the gap between two opposite comb fingers.

In this MB-TFG, as shown in Fig. 2.4, a polarization DC voltage V_P is applied to the MB-TFS and, hence, the mobile comb-drive electrode. Its purpose is for capacitive transduction and preventing frequency doubling of the drive force [24]. In the meantime, an AC voltage v_d is applied to the fixed comb-drive electrode at one side in order to excite the drive-mode vibration, and output current is generated from the fixed comb-drive electrode at the other side. Likewise, if the AC voltage is applied to the four parallel-plate tuning electrodes to excite the sense-mode vibration, output current can be detected from the other four parallel-plate sense electrodes.

In the drive-mode, the equivalent lumped-element mechanical model is illustrated in Fig. 2.5, where M is the effective mass of the MB-TFS, D_d is the damping in the drive-mode, k_d is the effective mechanical stiffness of the flexural beams in the drive-mode.

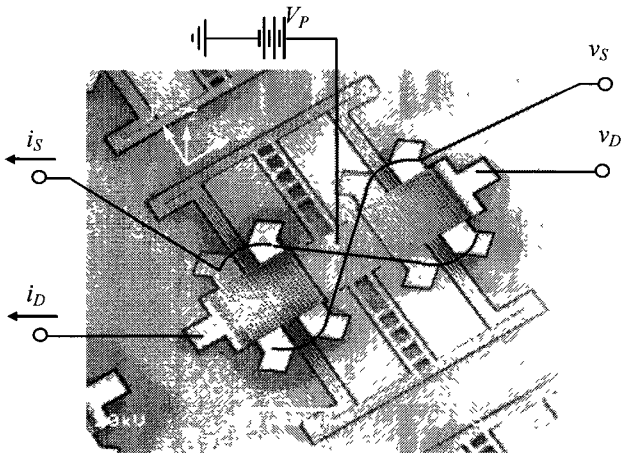

Figure 2.4: Signal configuration of the MB-TFG for characterizing its drive-mode and the sense-mode vibration behavior

The second-order ordinary differential equation (ODE) describing the relationship between the proof-mass displacement along the x-axis (x) and the driving AC voltage for the MB-TFG (v_d) is given by

$$M\frac{d^2x}{dt^2} + D_d\frac{dx}{dt} + k_d x = -2n\varepsilon_0\frac{h}{d_d}V_P v_d \tag{2.10}$$

$$D_d = \frac{\omega_d M}{Q_d} \tag{2.11}$$

$$k_d = \omega_d^2 M \tag{2.12}$$

The electrostatic force in Eq. 2.10 is the total force from the comb-drive electrodes both at the input and output. It is similar to Eq. 2.9 except that V_P is the DC polarization voltage on the mechanical structure and v_d is the AC driving voltage at the input port.

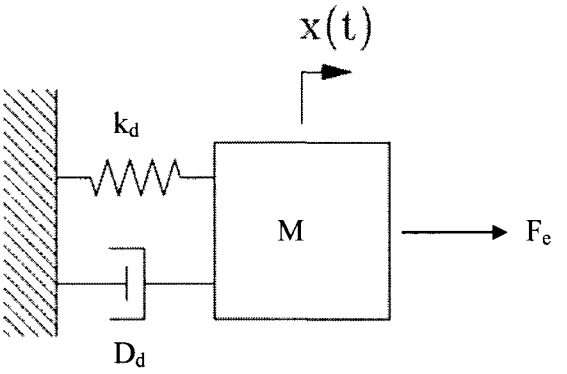

Figure 2.5: Equivalent mechanical model of the MB-TFG in the drive-mode

The natural resonant frequency of this system is given by

$$f_d = \frac{1}{2\pi}\sqrt{\frac{k_d}{M}} \tag{2.13}$$

As mentioned before, electromechanical coupling effect exists at both the conversions from the input voltage to driving force and from the structure motion to output current. In the drive-mode, the electromechanical coupling coefficient is found to be

$$\eta_d = -2n\varepsilon_0 \frac{h}{d_d} V_P \tag{2.14}$$

and it is the same at both input and output ports.

Since the MB-TFG needs to be incorporated into the drive-loop electronics for operation, its model in the electrical domain is also important. For electrical system simulation using PSPICE, the drive-mode ODE can be modeled as an equivalent series-RLC circuit [25]. As shown in Fig. 2.6, R_d, L_d and C_d are referred to as the motional resistance, inductance and capacitance of the drive-mode, respectively. C_{d0} is the static

capacitance from the comb-drive electrodes and i_d is the generated motional current because of the proof-mass motion.

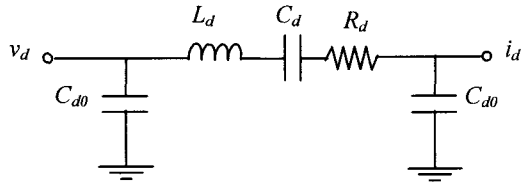

Figure 2.6: Equivalent series-RLC circuit model of the MB-TFG in drive-mode

The motional parameter values of the circuit model are given by

$$R_d = \frac{D_d}{\eta_d^2} = \frac{\omega_d M d_d^2}{4Q_d(n\varepsilon_0 h V_P)^2} \qquad L_d = \frac{M}{\eta_d^2} \qquad C_d = \frac{\eta_d^2}{k_d} \tag{2.15}$$

In order to obtain the vibration information of the MB-TFS from the input and output electrical signals, the drive-mode vibrations must be related to the electrical signals of the comb-drive electrodes. The drive-mode vibration amplitude, q_d, of the proof-masses is related to the ac voltage, v_d, at the input port by

$$q_d = \frac{v_d \eta_d Q_d}{k_d} = \frac{2n\varepsilon_0 h V_P v_d Q_d}{d_d k_d} \tag{2.16}$$

where Q_d is the quality factor of the drive-mode.

The current, i_d, at the output port is related to the drive-mode vibration amplitude by

$$i_d = q_d \eta_d \omega_d = -2n\varepsilon_0 \frac{h}{d_d} V_P q_d \omega_d \tag{2.17}$$

where ω_d is the angular resonant frequency of the drive-mode. Note that the current at the output port is proportional to the drive-mode velocity of the proof-masses.

2.3.2 Sense Mode

Different from the comb-drive electrodes in the drive-mode, the sense-mode uses parallel-plate electrodes to actuate and detect the proof-mass motion. Fig. 2.7 shows the parallel-plate electrode employed in this MB-TFG, which is also DRIE fabricated.

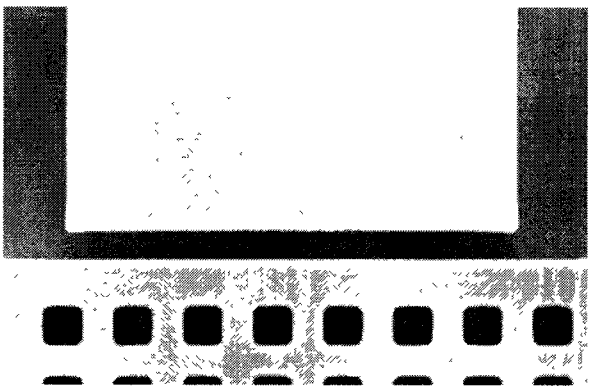

Figure 2.7: DRIE fabricated parallel-plate electrode

In Fig. 2.7, the upper plate is fixed on the substrate while the lower plate is just the movable proof-mass. When a voltage difference is established between the two plates and the proof-mass is vibrating thus changing the gap between the two plates, electrostatic force is generated and is given by

$$F_e = \frac{1}{2} C_{s0} \frac{V^2}{d_s} + C_{s0} \frac{V^2}{d_s^2} y \tag{2.18}$$

where C_{s0} is the static sense capacitance, d_s is the sense gap and y is the displacement of the proof-mass towards the upper plate. Note that this electrostatic force includes a linear term that is proportional to the displacement of the proof-mass in the sense direction.

The equivalent lumped-element mechanical model of the sense-mode is the same as that of the drive-mode, shown in Fig. 2.5, expect that the effective mechanical stiffness depends on an electrostatic stiffness k_e The second-order ODE relating the proof-mass displacement along the y-axis (y) to the input AC voltage (v_s) in the sense-mode is given by

$$M\frac{d^2y}{dt^2} + D_s\frac{dy}{dt} + (k_s - k_e)y = -\frac{C_{s0}}{d_s}V_P v_s \tag{2.19}$$

$$k_e = 2\frac{C_{s0}}{d_s^2}V_P^2 \tag{2.20}$$

The electrostatic force in Eq. 2.19 is the total force of the input and output ports. Its derivation automatically leads to the electrostatic stiffness in Eq. 2.20. The dependence of the effective mechanical stiffness on k_e is referred to as the electrostatic spring-softening effect since the electrostatic stiffness always reduces the effective mechanical stiffness. The other motional parameters and the resonant frequency in the sense-mode take the same forms as those in the drive-mode.

In the sense-mode, the electromechanical coupling coefficient is found to be

$$\eta_s = -\frac{C_{s0}}{d_s}V_P \tag{2.21}$$

and it is the same at both input and output ports.

The equivalent series-RLC circuit model in the sense-mode is the same as that in the drive-mode, shown in Fig. 2.6. Its motional parameters are given by

$$R_s = \frac{D_s}{\eta_s^2} = \frac{\omega_s M d_s^4}{Q_s(\varepsilon_0 l_s h V_P)^2} \qquad L_s = \frac{M}{\eta_s^2} \qquad C_s = \frac{\eta_s^2}{k_s - k_e} \tag{2.22}$$

Similarly, the relations between the electrical signals, v_s and i_s, at the input and output ports and the sense-mode vibration amplitude, y_s, are given as below

$$y_s = \frac{v_s \eta_s Q_s}{k_s - k_e} = \frac{C_{s0} V_P v_s Q_s}{d_s(k_s - k_e)} \tag{2.23}$$

$$i_s = y_s \eta_s \omega_s = -\frac{C_{s0}}{d_s} V_P y_s \omega_s \tag{2.24}$$

where Q_s and ω_s are the quality factor and angular resonant frequency of the sense-mode, respectively.

The above analysis on the sense-mode is based on the actuation using AC voltage signal, in real operation of the MB-TFG, however, the excitation signal for the sense-mode vibrations is a rotation rate signal Ω_z. The actuation force is a Coriolis Force given by

$$F_\Omega = 2M\Omega_z \frac{dx}{dt} = 2M\Omega_z q_d \omega_d \tag{2.25}$$

After substituting the electrostatic force in Eq. 2.19 with this Coriolis Force, the output current of Eq. 2.24 can be derived again and this is already given in Eq. 2.6.

The other noteworthy point is that since a DC tuning voltage V_T is applied on the four tuning electrodes while operating the MB-TFG, the actual electrostatic stiffness of the sense-mode is

$$k_e = \frac{C_{s0}}{d_s^2} V_P^2 + \frac{C_{s0}}{d_s^2} (V_P - V_T)^2 \tag{2.26}$$

It can be seen that both the polarization voltage and the tuning voltage can adjust the electrostatic stiffness and therefore the resonant frequency of the sense-mode. This dependence on the polarization voltage and the tuning voltage is the basis of the electrostatic frequency tuning in the mode-matching of this MB-TFG.

2.4 Quadrature Error and Mode-Matching

Fabrication imperfections of the micromachined structure in MB-TFG result in spatial misalignments of the proof-masses and a mechanical resonant frequency separation between the two vibration modes. These errors are detrimental to gyroscope performance and will be discussed next.

2.4.1 Quadrature Error

Due to fabrication imperfections of the mechanical structure, there is an error signal common to all CVGs. Referred to as the quadrature error, it causes off-axis movement of the proof-masses, resulting in a residual displacement along the sense axis even in the absence of rotation [26]. A single proof-mass is illustrated in Fig. 2.8, which is allowed to move along both the drive and sense axes (x-axis and y-axis). Ideally, the motion of the proof-mass in the drive-mode resonance should be strictly restricted along the x-axis,

while motion along the y-axis occurs only when the sense-mode is excited due to rotation-induced Coriolis Acceleration. However, imbalances present in the mechanical structure cause the proof-mass to vibrate at an angle θ_Q from the actual drive-axis as shown. This off-axis displacement of the proof-mass leads to mechanical coupling of the drive-mode resonant motion to the sensitive y-axis, and consequently an unwanted oscillatory deflection along the sense axis. Comparing to the Coriolis-induced deflection, this spurious mechanical coupling is the quadrature error, which produces an output signal even in the absence of any input rotation, contributing to the zero rate output (ZRO).

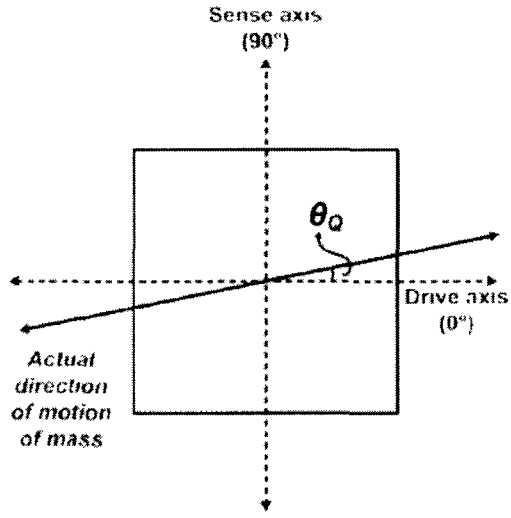

Figure 2.8: Origin of quadrature error in the MB-TFG proof-mass

Assuming that the proof-mass in Fig. 2.8 is driven into sinusoidal oscillation along the drive axis with the drive amplitude q_d and resonant frequency ω_d

$$x_d(t) = q_d \sin(\omega_d t) \tag{2.27}$$

The misaligned motion of the proof-mass by the off-axis angle θ_Q results in a displacement component along the sense axis, which is given by

$$y_{quad}(t) = \sin(\theta_Q) q_d \sin(\omega_d t) \approx \theta_Q q_d \sin(\omega_d t) \tag{2.28}$$

where $\sin(\theta_Q) \approx \theta_Q$ is the small angle approximation. However, consider the Coriolis-induced acceleration of the proof-mass that is given by $2v_x \times \Omega_z$ and the proof-mass velocity along the drive axis that is given by $\omega_d q_d \cos(\omega_d t)$, the Coriolis-induced proof-mass displacement along the sense axis is therefore

$$y_{Coriolis}(t) = \frac{2\Omega_z Q_{EFF} \omega_d q_d \cos(\omega_d t)}{\omega_s^2} = \frac{2\Omega_z Q_{EFF} q_d \cos(\omega_d t)}{\omega_d} \tag{2.29}$$

where matched-mode operation is assumed (ω_d=ω_s) and the MB-TFG leverages on the effective quality factor Q_{EFF} under matched-mode condition to gain the maximum Coriolis-induced proof-mass deflection in the sense axis.

A comparison between Eq. 2.28 and Eq. 2.29 demonstrates that although both the quadrature error and the Coriolis-induced deflections are amplitude modulated (AM) signals centered at the drive-mode resonant frequency, there is an inherent 90° phase shift between the two, and hence comes the term "quadrature error". This phase difference originates from the fact that the Coriolis Acceleration is proportional to the proof-mass velocity along the drive axis, while the quadrature error is proportional to the proof-mass position along the drive axis.

If considering the relative magnitude of the quadrature error signal to that of the Coriolis Signal, the level of the quadrature error signal could be significantly high. Eq. 2.30 shows the ratio of the quadrature error displacement to the Coriolis Displacement

$$\frac{y_{quad}}{y_{Coriolis}} = \frac{\omega_d \theta_Q}{2\Omega_z Q_{EFF}} \tag{2.30}$$

This indicates that when Q_{EFF} is low, even a small misalignment angle θ_Q could lead to a quadrature error that is much greater than the Coriolis Displacement.

To deal with the quadrature error signal in the sense channel, a phase-sensitive I-Q synchronous demodulation scheme is applied and will be discussed in Chapter 4. Nevertheless, the role of the quadrature error in preventing perfect mode-matching, i.e. zero Hz frequency separation between the two vibration modes, must be investigated. The influence of the quadrature error on the dynamics of the gyroscope system can be effectively demonstrated by the cross-coupling coefficients in the 2-DOF spring stiffness matrix K [26]

$$K = \begin{pmatrix} k_{xx} & k_{xy} \\ k_{yx} & k_{yy} \end{pmatrix} \tag{2.31}$$

where k_{xx} and k_{yy} denote the mechanical spring stiffness terms along the drive (x) and sense (y) axes respectively, while k_{xy} and k_{yx} are the cross-diagonal spring stiffness terms that model the quadrature error induced mechanical coupling. Quadrature error in CVGs has been identified as the single most important factor that precludes perfect mode-matching, since these cross-diagonal terms make a non-degenerate 2-DOF system. A mode-matched 2-DOF gyroscope system should be a degenerate system in which the mass and spring stiffness matrices are diagonal [26]. The quadrature induced off-diagonal terms in the spring stiffness matrix prevent this mode degeneracy leading to a mismatch in the resonant frequencies. Therefore, quadrature nulling techniques are required to eliminate the off-diagonal terms so that the spring stiffness matrix is diagonalized. In

practice, however, since perfect alignment of the proof-masses is not possible, the goal of quadrature nulling is to reduce the quadrature error as much as possible.

The minimization of the quadrature error is the first step in achieving perfect mode-matching. Reported CVGs in literature [13, 26-28] all use certain form of quadrature nulling technique that involves either electronic or mechanical compensation of the quadrature error signal. The work at Georgia Institute of Technology in 2007 [3] suggests an efficient and repeatable electrostatic nulling technique of the quadrature error. Dedicated quadrature nulling electrodes were added at the corners for each proof-mass. As illustrated in Fig. 2.9, the generated electrostatic balancing torques from these quadrature nulling electrodes can rotate the proof-masses, thereby correcting for any spatial misalignment and suppressing the quadrature error.

Considering the spring stiffness matrix K in Eq. 2.31, the quadrature error nulling technique eliminates the cross-diagonal terms as below

$$K(QN) = \begin{pmatrix} k_{xx} & k_{xy} - k_{xy-elec} \\ k_{yx} - k_{yx-elec} & k_{yy} \end{pmatrix} = \begin{pmatrix} k_{xx} & 0 \\ 0 & k_{yy} \end{pmatrix} \tag{2.32}$$

where $k_{xy\text{-}elec}$ and $k_{yx\text{-}elec}$ are the electrostatic stiffness generated from the balancing torques of the quadrature nulling electrodes.

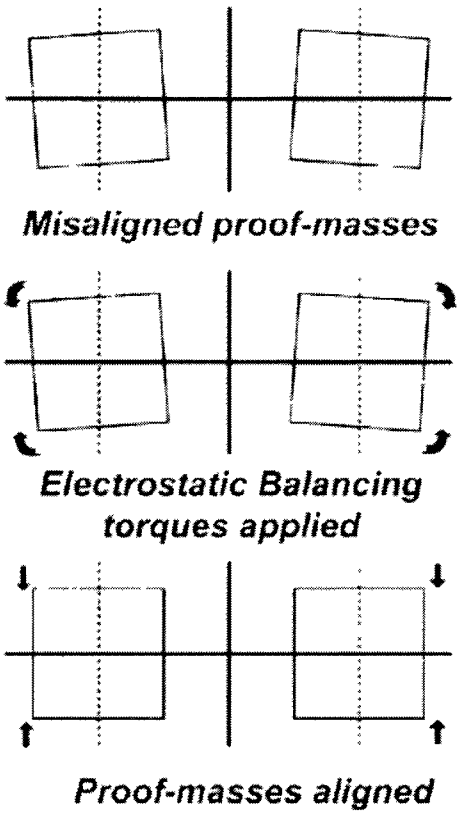

Figure 2.9: Illustration of quadrature error nulling using electrostatic balancing torques

Once the quadrature error has been minimized, the mechanical stiffness terms of the drive and sense modes can be made equal to ensure that their resonant frequencies are equalized. This is achieved by electrostatic frequency tuning as mentioned before.

2.4.2 Mode Matching

Fabrication imperfections, in addition to causing the quadrature error, also result in a resonant frequency separation between the two vibration modes. This is because of the deviation of the mechanical spring width from its original design value, which in turn leads to resonant frequency deviation. To compensate for this frequency variation,

electrostatic tuning of the resonant frequency in the sense-mode is performed. From the above analysis, the sense-mode resonant frequency can be given as

$$f_s = \frac{1}{2\pi}\sqrt{\frac{k_s - k_e}{M}} \tag{2.33}$$

Given by Eq. 2.26, k_e is the electrostatic stiffness along the sense axis that is induced by the use of parallel-plate electrodes in the sense-mode. Increasing the polarization voltage V_P lowers the sense-mode frequency, while the drive-mode frequency is relatively independent of the polarization voltage change because the drive-mode oscillations are excited using comb-drive electrodes and hence no electrostatic stiffness [29]. Eq. 2.33 also shows that since the electrostatic stiffness always lowers the sense-mode resonant frequency (therefore referred as electrostatic spring-softening effect), the sense-mode frequency is typically designed to be slightly higher than the drive-mode frequency, so as to enable frequency tuning and mode matching in presence of fabrication variations.

Mathematically, in mode-matching, electrostatic frequency tuning complements quadrature nulling by electronically equalizing the remaining diagonal terms in the spring stiffness matrix K, which can be represented as

$$K(V_P) = \begin{pmatrix} k_{xx} & 0 \\ 0 & k_{yy} - k_e \end{pmatrix} = \begin{pmatrix} k_{xx} & 0 \\ 0 & k_{xx} \end{pmatrix} \tag{2.34}$$

In summary, both quadrature error nulling and electrostatic frequency tuning are necessary to achieve the matched-mode operation. Improper quadrature error nulling technique does not suppress the off-diagonal terms in the spring stiffness matrix K and a minimum achievable separation between the two resonant frequencies will result even

after the electrostatic frequency tuning step. A lack of dedicated quadrature error nulling electrodes in [30] led to a minimum achievable frequency separation of 12Hz.

The primary motivation for mode-matching is to take advantage of the mechanical signal amplification provided by the effective quality factor (Q_{EFF}) of the gyroscope system. Since the Coriolis-induced energy transfer takes place at the drive-mode resonant frequency, Q_{EFF} represents the effective mechanical gain that the sense-mode can offer at the drive-mode resonant frequency. It therefore depends on the inherent quality factors of the mechanical structure, and the frequency separation between the drive and sense modes. For a given mechanical structure, Q_{EFF} is maximized under matched-mode condition. Although typical mechanical quality factors are in the range of 10,000 – 50,000 [31], higher effective Qs of around 100,000 are reported in [32] and more recently, quality factors in the scale of one million have been demonstrated at the Microsystems Lab of University of California at Irvine [33-36].

A high Q_{EFF} can improve the sensor performance in many ways. Most importantly, it lowers the overall noise floor of the system, as can be seen from Eq. 2.3 and Eq. 2.4. In particular, the capacitive sensitivity of the sensor is proportional to the amount of the proof-mass displacement along the sense axis, which is strongly dependent on the mode separation. In the unmatched mode condition, Q_{EFF} is low and very small mechanical gain, if any, is provided by the sense-mode, whereas in the matched mode condition, the capacitive sensitivity is amplified by a fairly higher Q_{EFF}, as given by

$$\frac{\Delta C}{\Omega_z} = \frac{2C_{s0}Q_{EFF}q_d}{\omega_0 d_{s0}} \tag{2.35}$$

where ω_0 is the sensor frequency. The enhancement in the capacitive sensitivity lowers the electronic noise floor and therefore alleviates the constraints on the interface electronics in terms of noise, gain and power [3].

However, with high Q_{EFF} mode-matching comes many other challenges. While a high Q_{EFF} amplifies the Coriolis Acceleration signal, unwanted signal like quadrature error gets amplified as well. Mode-matching also needs to be stable over time and temperature, and should be realized automatically for commercialization. Nowadays, a mismatched mode of 5-10% in resonant frequencies when operating the gyroscope is often preferred because of the significant challenges involved with the mode-matching of high-Q resonant modes of a mechanical structure [3].

CHAPTER III

FABRICATION

The fabrication technology of the micromachined gyroscopes mainly falls into two categories – surface micromachining technology and bulk micromachining technology. The Multiple-Beam Tuning-Fork Gyroscope (MB-TFG) in this work was fabricated using the surface micromachining technology with only one mask. After the initial performance characterization of the fabricated devices, a critical improvement was made to the MB-TFG design to significantly increase the quality factors of both vibration modes.

3.1 Fabrication Procedure

Tuning-fork gyroscopes in various derived forms have been designed and implemented using either surface micromachining technology [13, 26] or bulk micromachining technology [17-20, 37-39]. The MB-TFG design in this work was implemented using the surface micromachining technology since it generally can create much more complicated devices than can bulk micromachining. Though MB-TFG is a device with very delicate features, its fabrication procedure is quite simple and the yield percentage of one wafer is relatively high. Only one mask of Deep-Reactive-Ion-Etching (DRIE) is needed and the following Hydrofluoric (HF) acid etching completes the fabrication process.

The MB-TFG prototypes were fabricated on Silicon-On-Insulator (SOI) wafers with a 30μm-thick heavily-doped device layer and a 2μm-thick buried dioxide layer. A SOI wafer has a layered "silicon – insulator – silicon substrate" structure and its main

advantages over the conventional silicon processing include [40]: (1) lower parasitic capacitance due to isolation from the bulk silicon, which improves power consumption at matched performance, and (2) resistance to latchup due to complete isolation of the n- and p-well structures. In general, SOI substrates are compatible with most conventional fabrication processes. Fig. 3.1 illustrates the two-step fabrication process.

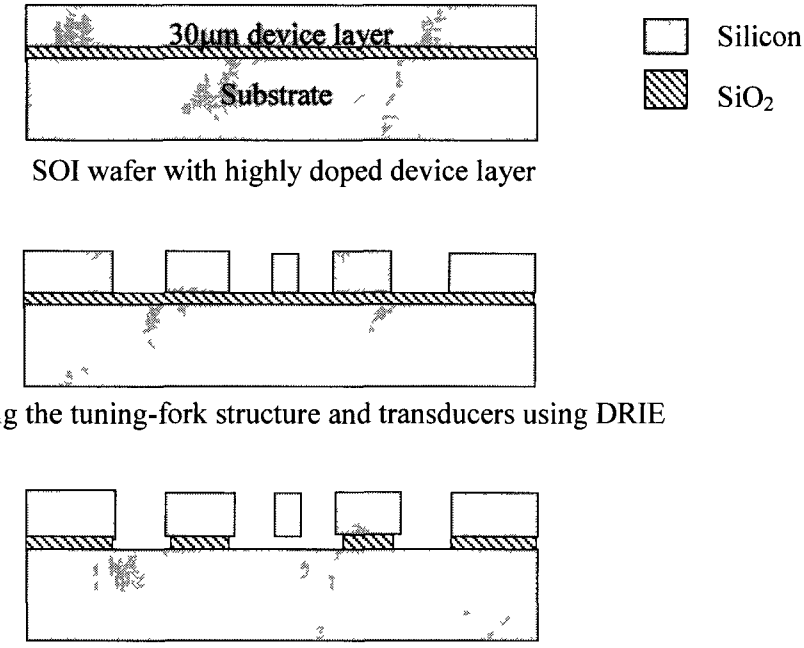

Figure 3.1: One-mask fabrication process of 30μm-thick tuning-fork gyroscopes on a SOI wafer

Deep Reactive Ion Etching (DRIE) is a micromachining technique that etches mechanical elements onto a silicon wafer. Unlike a wet chemical etch, DRIE micromachining uses a plasma etch to create features. This allows greater flexibility in etch profiles, enabling a wider array of mechanical elements [41]. A DRIE step with a

modest aspect ratio of 10:1 is first employed to transfer the design patterns of the MB-TFG on the single mask into the device layer. The time-controlled HF acid etching step is followed to etch away silicon dioxide underneath the MB-TFS, which as a result is released for mechanical motion. Meanwhile, the silicon dioxide under all the electrodes should be retained as much as possible with the purpose of strongly holding the electrodes for electrical connections. The DRIE step was performed at Cornell Nanofabrication Facility (CNF) using PT770 etcher and the HF acid etching step was performed at Micro Devices and Micromechanics Laboratory of Old Dominion University.

3.2 Design Improvement

The original design [42] kept only the MB-TFGs in the device layer and etched away all the surrounding silicon, as shown by a fabricated device in Fig. 3.2. From the analysis on the measured Qs, the main drawback of this design is that while the tuning-fork structure can be completely released for mechanical motion, the large openings next to the anchor increase the exposure of the silicon dioxide underneath the anchor to the HF acid and result in severe over-etch of this silicon dioxide. This undesirable side effect leads to significant amount of anchor loss and thus a much lower quality factor.

In order to overcome the anchor loss problem, an improved mask design defines the MB-TFG by its surrounding trenches, as shown by a fabricated device in Fig. 3.3. The idea is to create smaller openings next to the anchor so that the silicon dioxide underneath is less exposed to the HF acid. In this design, however, precise time control of HF acid etching is vital and sometimes very challenging since the complete release of the tuning-

fork structure and the maximal preservation of the silicon dioxide underneath the anchor need to be guaranteed simultaneously. The optimal etching time is verified through repetitive experiment.

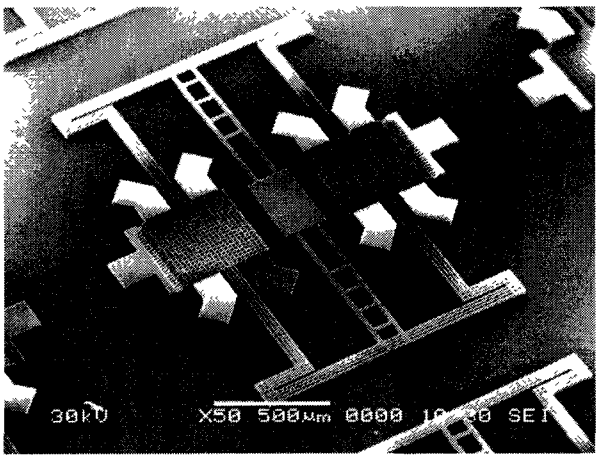

Figure 3.2: A fabricated MB-TFG from the original design

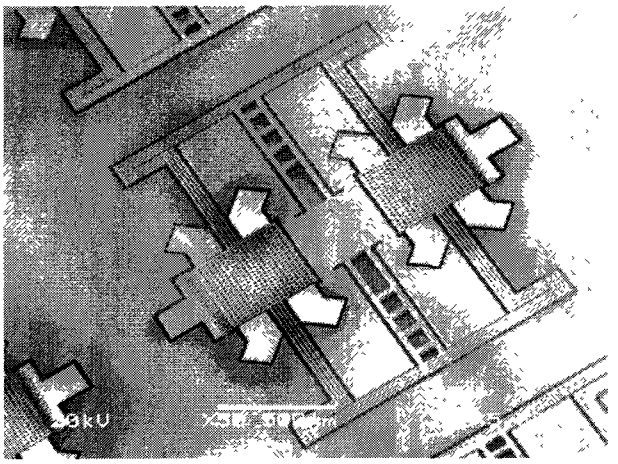

Figure 3.3: A fabricated MB-TFG from the improved design

After fabrication, each MB-TFG device needs to be checked for proof-mass motion using the probe station before mounted onto Printed-Circuit-Board (PCB) for

characterization. Fig. 3.4 shows a device under a probe. The proof-masses and the beams should be able to move with ease under a small force from the probe.

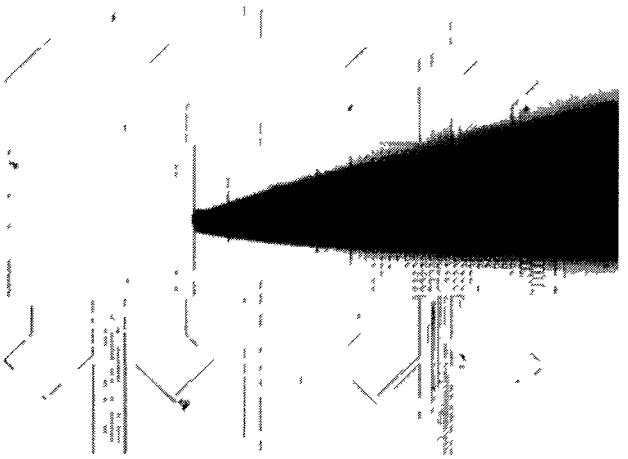

Figure 3.4: A MB-TFG device under probe

The fabricated gyroscope is shown in Fig. 3.5 in different views. Fig. 3.5 (a) shows a top view of the trench feature in this MB-TFG, which acts as a protection measure to limit the over-etching of silicon dioxide underneath the anchor and electrodes. The close-up view in Fig. 3.5 (b) shows the sense gap, the comb-drive fingers and the release holes on a proof mass. Fig. 3.5 (c) shows a cross-section view that illustrates the removal of silicon dioxide between the proof-mass and the substrate, which confirms that the proof-mass is completely released. Also shown in this figure is the over-etching effect in DRIE, which can be made negligible through process optimization. The cross-section view of Fig. 3.5 (d) illustrates the HF acid over-etching effect under an anchor. The surrounding trenches reduced the effect but inevitably some silicon dioxide under the anchor has been etched away at the sides.

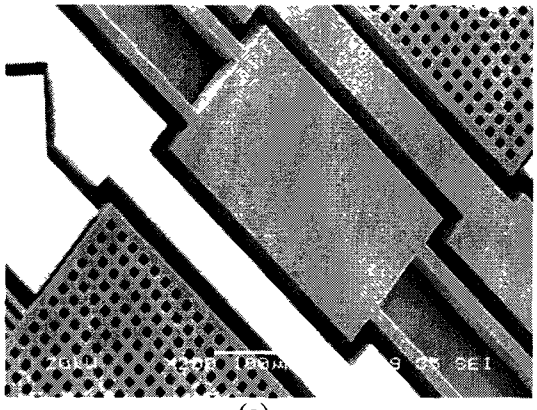

(a)

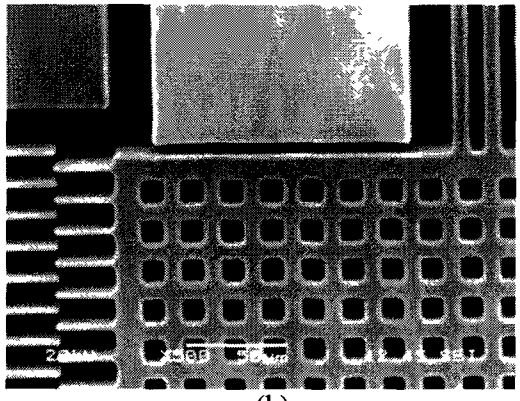

(b)

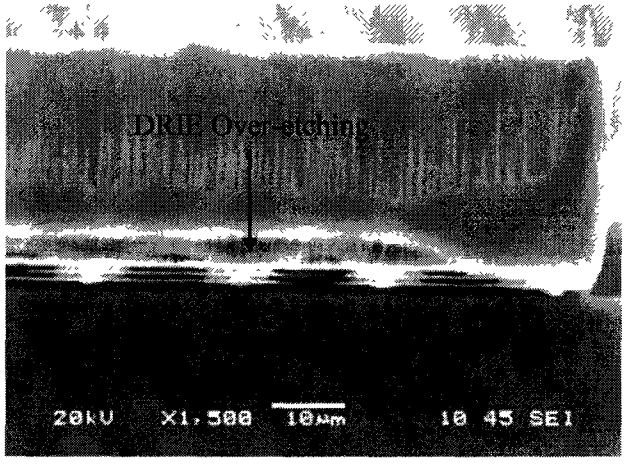

(c)

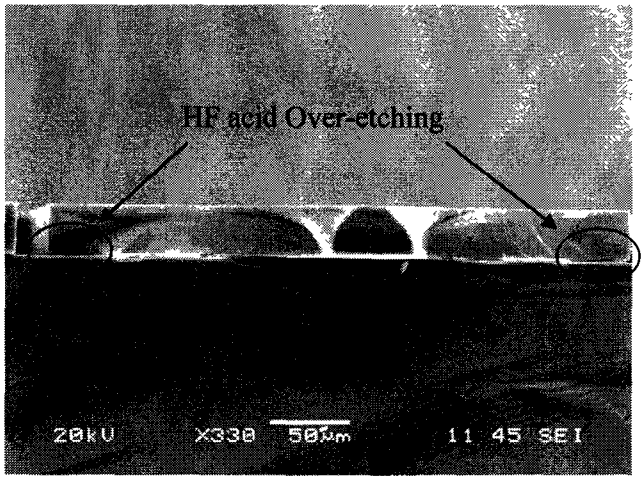

(d)

Figure 3.5: SEM pictures of the MB-TFG showing its different features

Table 3.1 summarizes the key design parameters of the MB-TFG in order to provide a general idea on this device.

Table 3.1: Summary of the key design parameters of the MB-TFG

Parameter	Value	Symbol	Unit
Dimension of a device	1.7×1.7	-	mm^2
Thickness	30	h	μm
Beam width	10	b	μm
Dimension of a proof mass	400×400	-	μm^2
Number of comb fingers	25	n	-
Gap between fingers	4	g	μm
Initial sense/tuning capacitance	0.046	C_{S0}/C_{T0}	pF
Sense/tuning gap	3	d_{S0}/d_{T0}	μm
Width of the sense/tuning electrodes	130	W_e	μm
Number of the sense/tuning electrodes	4	n_S/n_T	-

The whole MB-TFG device has an in-plane dimension of 1.7mm×1.7mm. The in-plane dimension of the proof masses is 400μm×400μm and the beam width of the flexural structure is 10μm. The thickness of the MB-TFG is 30μm because the device was fabricated on a 30μm-thick device layer of a SOI wafer. The release holes in the proof-masses are all 10μm×10μm in size and they are used for ensuring full release of the proof-masses. The key design parameters of the electrostatic electrodes are illustrated in Fig. 3.6. The minimum design feature is 3μm at the sense gap and the tuning gap between the parallel-plate electrodes and the proof masses. Note that the tuning electrodes and the sense electrodes have an identical design dimension.

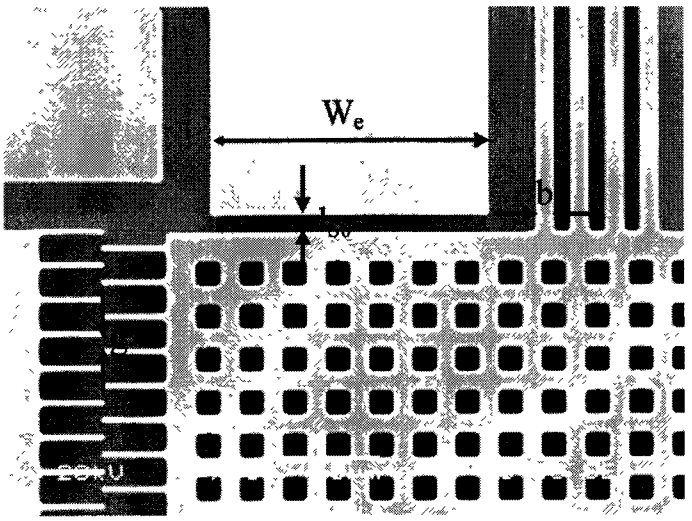

Figure 3.6: Key design parameters of the electrostatic electrodes

Due to fabrication imperfections, the actual fabricated dimensions of the sense/tuning gap and the gap between comb fingers are much larger, which can be confirmed by the SEM pictures in Fig. 3.7. Although the design feature for the sense/tuning gap is 3μm, it is actually about 5μm in Fig. 3.7 (a). Likewise, in Fig. 3.7 (b), the actual gap between the comb-drive fingers is about 7μm, while its design value is 4μm. These fabrication variations will be taken into consideration in the theoretical evaluation of the gyroscope performance.

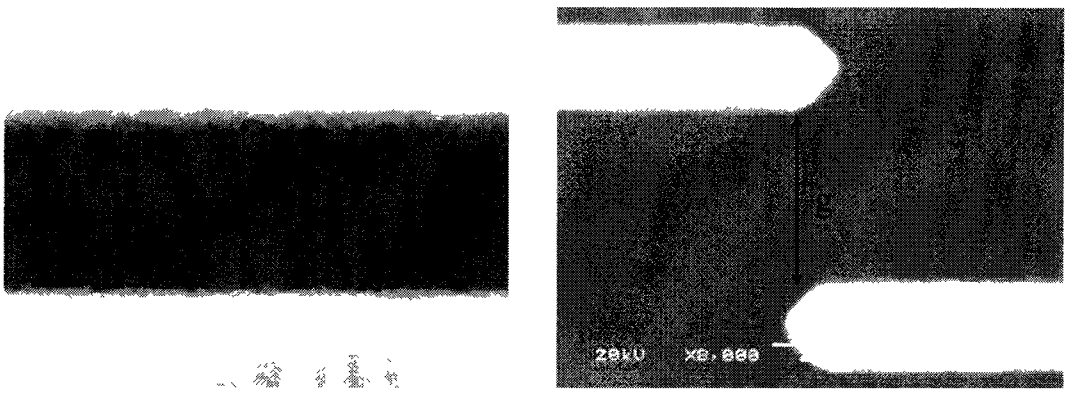

(a) Sense gap (b) Comb finger gap

Figure 3.7: SEM pictures of the actual gaps in the MB-TFG

In summary, using surface micromachining technology, the MB-TFG was fabricated based on the mask which defines small openings next to the anchor for the purpose of alleviating the fabrication effect on the anchor loss of the MB-TFG, thus significantly increasing its quality factors.

CHAPTER IV

INTERFACE ELECTRONICS

Interface electronics for actuating, controlling and sensing of the micro-mechanical structure of the gyroscope are an important part of a gyroscope system. Based on functionality, the electronics for a MB-TFG can be divided into two subsystems – the drive loop and the sense channel. The drive loop electronics are responsible for starting and sustaining an oscillation of the proof-masses along the drive axis with constant amplitude, while the function of the sense channel is to extract the input rotation information from the direct output of the gyroscope. In both the drive loop and the sense channel, a Transimpedance Amplifier (TIA) is used as the front-end for interfacing with the MB-TFG.

4.1 Transimpedance Front-end for Capacitive Detection

As the performance of the micromachined gyroscope itself is continuously improved, its interface circuit becomes critical in determining the overall system performance. The MB-TFG in this work is a capacitive sensor that needs a low-noise front-end stage to detect its very small capacitance changes, which largely depend on the mechanical motion of the proof-masses. A low-noise front-end interface is vital in achieving a high system resolution. Therefore, the first step in developing the interface electronics is to choose an appropriate front-end stage that is able to convert small mechanical signals such as displacement and velocity into useful electrical quantities (current and voltage) for subsequent signal processing.

The minimum detectable rotation rate of the gyroscope depends on the noise floor of the whole system – gyroscope and its interface electronics. It is defined as the resolution of the system and is given by the total noise equivalent rotation (TNEΩ) in Eq. 2.2. The objective in the interface electronics design is to ensure that the electrical noise equivalent rotation (ENEΩ) is less than the mechanical noise equivalent rotation (MNEΩ), i.e., the circuit noise is not the limiting factor in the system performance [3].

The ENEΩ depends on the minimum detectable capacitance change of the sense channel and the capacitive sensitivity (F/°/hr) that relates the parallel-plate capacitance change of the sensor to an input rotation rate

$$ENE\Omega = \frac{\Delta C_{min}}{\frac{\Delta C}{\Omega_z}} \tag{4.1}$$

From the motional current of Eq. 2.6, the capacitive sensitivity can be derived as

$$\frac{\Delta C}{\Omega_z} = \frac{2C_{s0}Q_{EFF}q_d}{\omega_0 d_{s0}} \tag{4.2}$$

For a parallel-plate capacitive transducer, the minimum detectable capacitance change (ΔC_{min}) is proportional to the total input-referred current noise of the interface electronics integrated over the bandwidth of interest, as given by

$$\Delta C_{min} = \frac{I_{noise}\sqrt{BW}}{\omega_0 V_P} \tag{4.3}$$

where V_P is the fixed DC voltage maintained across the sense gap.

Although the ENEΩ can be lowered with the help of high aspect-ratio micromachining technique such as High Aspect-Ratio Combined Poly and Single-Crystal Silicon (HARPSS) in [43], this section concentrates on reducing the total input-referred current noise of the interface electronics from the circuit theory point of view.

Several techniques have been developed in interface front-ends to detect the small capacitive displacement in MEMS gyroscopes. Charge integration using switched capacitor front-ends is employed for static MEMS accelerometers [44, 45], and micromachined gyroscopes [46, 47]. These schemes are suited for gyroscopes with low operating frequencies due to the power budget restriction. Further, the use of a switching voltage on the mechanical structure causes significant feed-through and parasitic electrical coupling [3].

The continuous-time charge integrator front-ends are used in [13, 26], since large AC impedances can be generated using capacitors at the operating frequencies. In addition, there is no kT/C noise associated with the capacitors because they are not switched. However, these integrators require a large resistor to bias the input node and the thermal noise of this large feed-back resistor forms the dominant noise contributor of the front-end and determines the overall performance [3].

For micromechanical resonator-based oscillators in [48], Transimpedance Amplifier (TIA) with a feed-back resistor is used for continuous-time sensing of the motional current. Similarly, in this work, the TIA is employed in the drive loop as the front-end to detect the motional current. Furthermore, it is also used as the low-noise front-end for capacitive Coriolis Detection in the sense channel.

In order to investigate the TIA as the low-noise front-end in both the drive loop and for capacitive detection in the sense channel, its schematic interfacing with a micromachined gyroscope is shown in Fig. 4.1.

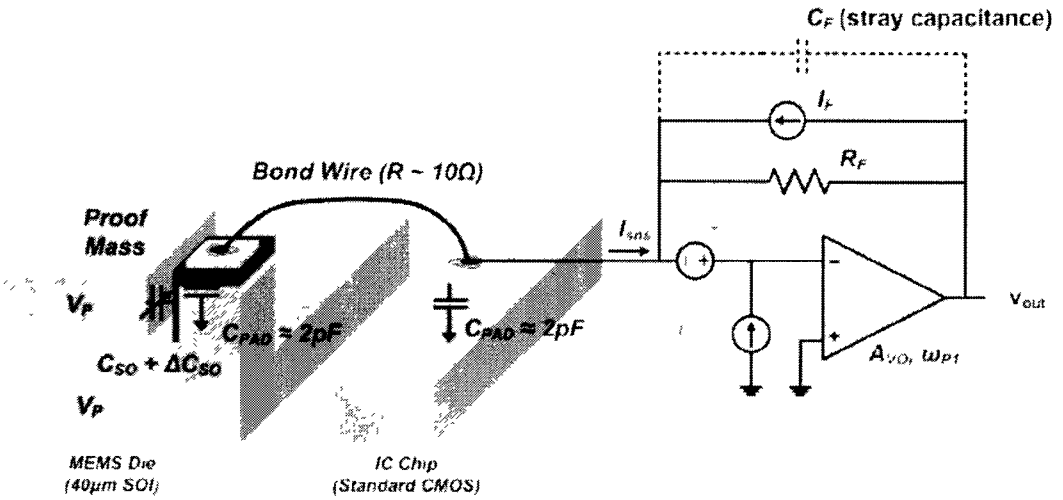

Figure 4.1 [3]: TIA (with noise sources) interfaced with a microgyroscope

In the above figure, a constant DC voltage V_P is maintained on the proof-mass and the substrate. R_F is the feedback resistance and C_F is the associated stray capacitance. At the inverting terminal of the op-amp, there is a lumped parasitic capacitance, C_{TOT}, that is composed of the pad capacitances and the gate capacitance of the input differential pair transistors in the op-amp [3].

The schematic in Fig. 4.1 can be simplified to an op-amp inverting amplifier shown in Fig. 4.2, where R_{MOT} represents the motional resistance of the MB-TFG in either the drive-mode or the sense-mode. Because of the high open-loop DC gain of the op-amp and its negative feedback configuration, the inverting terminal of the op-amp is a good

virtual ground and therefore presents very low input impedance. As a result, the output current signal path is relatively insensitive to the total parasitic capacitance C_{TOT}, thus preventing significant signal loss. This is one advantage of the TIA front-end.

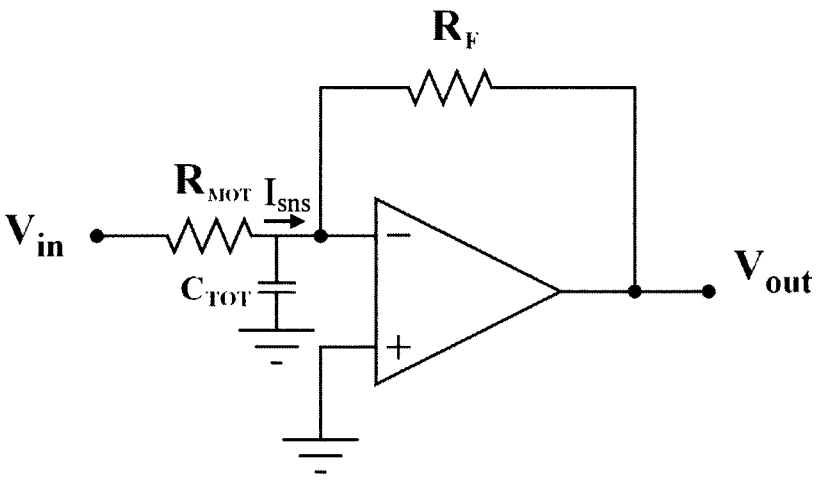

Figure 4.2: Simplified op-amp inverting amplifier

Another advantage of using the TIA front-end is that it also helps reduce the loading effect of the interface electronics on the quality factor of the gyroscope in the drive-mode, because of its low input impedance. Fig. 4.3 illustrates this effect.

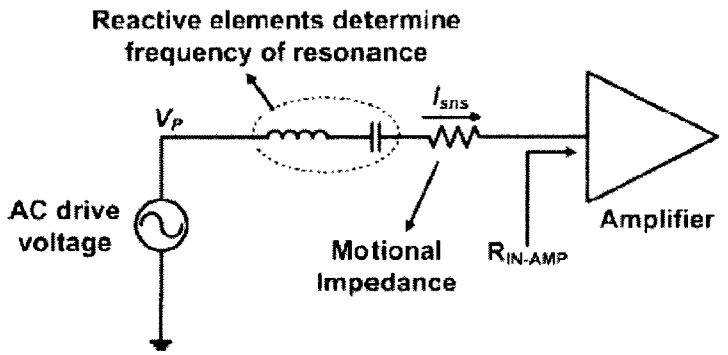

Figure 4.3 [3]: Quality factor loading due to interface electronics

When the drive loop locks into electromechanical oscillations, the loaded drive-mode quality factor (Q_L) is lower than its unloaded value (Q_{UL}) [48]

$$Q_L = \frac{R_{MOT-D}}{R_{MOT-D} + R_{IN-AMP} + R_{OUT}} Q_{UL} \tag{4.4}$$

where $R_{IN\text{-}AMP}$ and R_{OUT} are the input and output impedances seen by the gyroscope from the drive loop electronics. For an immediate TIA front-end interfacing with the gyroscope, $R_{IN\text{-}AMP}$ is approximated by

$$R_{IN-AMP} \approx \frac{R_F}{A_{OL}} \tag{4.5}$$

where A_{OL} is the DC open-loop gain of the op-amp, which is typically between 80 – 100dB. Considering that typical values for R_F are in the MΩ range, the $R_{IN\text{-}AMP}$ can be very low. Therefore, the Q-loading effect can be minimized with a TIA front-end.

Returning to Fig. 4.1, the main noise contributors in the TIA front-end are identified as the input-referred voltage and current noise of the op-amp ($\overline{v_{opamp}^2}$ and $\overline{i_{opamp}^2}$), and the thermal current noise of the feedback resistor R_F which is given by

$$I_F = \frac{4k_BT}{R_F} \tag{4.6}$$

Because the sensor output is a current, then the total equivalent input-referred current noise ($I_{N\text{-}TOT}$) of the TIA front-end determines the minimum detectable capacitance change in Eq. 4.3, and hence the gyroscope resolution. $I_{N\text{-}TOT}$, given by [49], includes effects from the total parasitic capacitance seen at the input node C_{TOT} and the input resistance of the op-amp $R_{IN\text{-}opamp}$

$$\overline{i_{N-TOT}^2} = \overline{i_{opamp}^2} + \overline{v_{opamp}^2} \times \left(\frac{1}{R_F} + \frac{1}{R_{IN-opamp}} + \omega C_{TOT}\right)^2 + \frac{4k_BT}{R_F} \tag{4.7}$$

In the operation bandwidth of the sensor, the equivalent input noise spectrum is assumed white and the thermal noise of the feedback resistor is the dominant noise source. Eq. 4.7 is reduced to

$$I_{N-TOT} \approx \sqrt{\frac{4k_BT}{R_F}} \tag{4.8}$$

Based on Eqs. 4.1 to 4.3, the electronic noise floor ENEΩ of the MB-TFG interfaced with a TIA front-end is given by

$$ENE\Omega = \frac{\Delta C_{min}}{\frac{\Delta C}{\Omega_z}} = \frac{d_{s0} I_{N-TOT}\sqrt{BW}}{2V_P C_{s0} Q_{EFF} q_d} \approx \frac{d_{s0}\sqrt{\frac{4k_BT}{R_F}}\sqrt{BW}}{2V_P C_{s0} Q_{EFF} q_d} \tag{4.9}$$

Now, consider the noise current $I_{Brownian}$ that is due to the random Brownian motion of the proof-mass along the sense axis, which is given by

$$I_{Brownian} = \omega_0 V_P \frac{\partial C_{s0}}{\partial y} y_n \tag{4.10}$$

where the noise displacement y_n is derived in [28] using the Equi-Partition Theorem in [50]

$$\overline{y_n^2} = \frac{4k_BTQ_{EFF}}{M\omega_0^3} \tag{4.11}$$

It is worth noting that using Eqs 4.10, 4.11 and 2.6, the mechanical noise floor MNEΩ can be derived as in Eq. 2.3.

As described in Chapter 2, similar to a drive-mode, the sense-mode of the MB-TFG can also be modeled as a second order system with an equivalent series RLC circuit representation. The Brownian Noise Current can also be expressed as

$$\overline{I_{Brownian}^2} = \frac{4k_BT}{R_{MOT-S}} \tag{4.12}$$

where $R_{MOT\text{-}S}$ is the motional resistance of the sense-mode. If comparing the mechanical Brownian noise current to the total input-referred noise current of the TIA frond-end, the ratio is

$$\frac{I_{Brownian}}{I_{N-TOT}} = \frac{\sqrt{\frac{4k_BT}{R_{MOT-S}}}}{\sqrt{\frac{4k_BT}{R_F}}} = \sqrt{\frac{R_F}{R_{MOT-S}}} \tag{4.13}$$

Therefore, increasing R_F over $R_{MOT\text{-}S}$ makes the total input-referred noise current of the TIA frond-end smaller than the mechanical Brownian Noise Current, which in turn means a smaller ENEΩ than MNEΩ.

From the above analysis, it is evident that an increased R_F is beneficial not only for larger TIA gain, but also for lower input circuit noise. R_F in the sense channel is chosen to be larger than the motional resistance of the sense-mode ($R_{MOT\text{-}S}$) so that the circuit noise is not the limiting factor in determining the system performance of the MB-TFG.

However, as will be seen later, since the overall gain of the drive loop needs to be controlled for the purpose of sustaining a stable oscillation, the feedback resistance of the

TIA front-end in the drive loop cannot be too large. Otherwise, the subsequent circuit stages are not able to tune the overall gain to satisfy the condition for a stable oscillation in the drive loop.

4.2 Drive Loop Electronics

After choosing TIA as the front-end interface, drive loop and sense channel circuits can be built. The purpose of the drive loop circuit is to start up and sustain the oscillation of the proof-masses along the drive axis with constant amplitude. Constant amplitude of the drive-mode vibration is crucial in successful and accurate operation of the gyroscope, since variations of the drive-mode amplitude result in velocity changes of the mechanical structure along the drive axis. Considering this velocity signal is the carrier signal in the amplitude modulation with the input angular rate signal, any fluctuation can lead to false or inaccurate rate output. A key feature of the drive loop circuit in this work is an Automatic Gain Control (AGC) scheme that is used to achieve and maintain constant amplitude in the drive-mode oscillation of the gyroscope.

4.2.1 Electromechanical Resonant Oscillator

The working principle of the drive loop is an electromechanical resonant oscillator circuit that combines the electronics and the MB-TFG device, which is similar to the approach used for micromechanical resonator oscillators in [25]. The drive-mode mechanical resonant frequency is the oscillating frequency of the gyroscope. The drive-mode oscillation with constant amplitude is established by using a positive feedback loop that satisfies the Barkhausen's Criteria, which is illustrated in Figure 4.4.

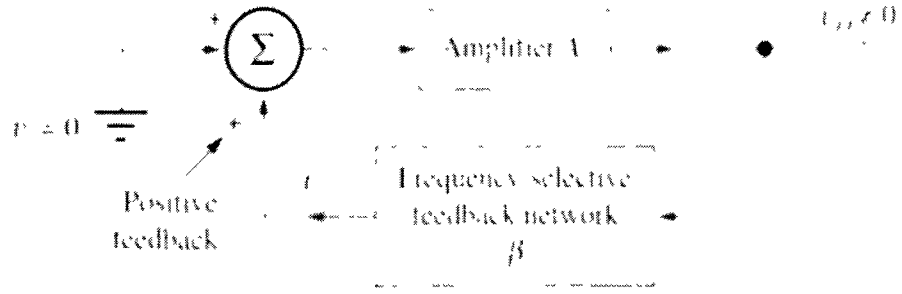

Figure 4.4: A positive feedback loop illustrating the Barkhausen's Criteria

The criteria state that in the feedback loop above, if A(s) is the open-loop gain of the amplifier and β(s) is the transfer function of the feedback path, then βA is the loop gain around the feedback loop and this circuit will sustain steady-state oscillations only at frequencies for which:

1) The loop gain is equal to unity in magnitude, i.e., $|\beta A| = 1$;
2) The phase shift around the loop is zero or an integer multiple of 2π, i.e., $\angle\beta A = 2\pi n$, $n=0, 1, 2, \ldots$

In the drive loop system of this MB-TFG, the gyroscope device is the "Frequency-selective feedback network" β(s) since its frequency response shows that it functions as an analog filter. The rest electronics in the drive loop represent the "Amplifier" A(s), which is responsible for sensing the output current from the gyroscope and providing an input driving voltage to the gyroscope.

The closed-loop gain of the drive loop system is given by

$$A_V(s) = \frac{A(s)}{1 - A(s)\beta(s)} = \frac{A(s)}{1 - T(s)} \tag{4.14}$$

From this equation, when the Barkhausen's Criteria are met, i.e., T(s) = 1, the closed-loop gain goes to infinite. It explains that while there is a finite output, no input is needed, in other words, this system is self-oscillating.

The drive-mode oscillation originates from the inherent mechanical (Brownian) and electronic noise in the system. Although there are many frequency components in a noise signal, due to the filter characteristic of the MB-TFG, only the component that is of the same frequency as the mechanical resonant frequency of the MB-TFG is selected and gets through. By ensuring the satisfaction of the Barkhausen's Criteria, this positive feedback signal has no net phase shift with respect to the initial noise signal of the same frequency. Therefore, it strengthens this initial signal at the mechanical resonant frequency of the MB-TFG, and finally turns it into the oscillation signal of the MB-TFG.

Another important fact states that in order to start up the oscillation in the drive loop, the initial loop gain ($T = \beta A$) must be larger than unity. To understand this point, consider that in this series resonant oscillator design, the loop gain is given by

$$T = \frac{R_{AMP}}{R_{MOT-D} + R_{IN} + R_{OUT}} \approx \frac{R_{AMP}}{R_{MOT-D}} \tag{4.15}$$

where R_{AMP} denotes the total transimpedance gain of the drive loop electronics (TIA front-end and subsequent voltage gain stage), R_{MOT-D} is the equivalent motional resistance of the drive-mode, R_{IN} and R_{OUT} are the input and output resistances seen by the gyroscope from the drive loop electronics. Since R_{MOT-D} can be well over 10MΩ, while R_{IN} and R_{OUT} are typically low from the previous analysis, the loop gain is reduced to a ratio between R_{AMP} and R_{MOT-D}.

Conceptually, the motional resistance R_{MOT-D} represents the transmission loss in the drive loop. To compensate for this mechanical energy dissipation of the MB-TFG, electrical energy is supplied by the sustaining electronics in the drive loop and is represented by the total transimpedance gain R_{AMP}. When the electrical energy supplied is higher than the mechanical energy dissipated in one cycle, i.e., $R_{AMP} > R_{MOT-D}$ and, hence $T > 1$, oscillation occurs. As the cycle goes on, the oscillation signal will be reinforced and built up until either some form of nonlinearity or a designed automatic level control circuit (as in this case) makes $R_{AMP} = R_{MOT-D}$, at which point $T = 1$ and the oscillation is sustained at a certain constant amplitude. Note that throughout the magnitude variation of the loop gain, its net phase shift must remain to be zero so that positive feedback is always guaranteed.

4.2.2 Circuit Configuration

The complete interface electronics for operating the MB-TFG, including both the drive loop and the sense channel, are shown in Fig. 4.5. This section covers only the drive loop configuration, while the sense channel configuration will be discussed later. When the gyroscope is in operation, its two proof-masses are excited into resonant oscillation along the drive axis using the comb-drive electrodes that are located symmetrically on both sides of the MB-TFS, as shown in Fig. 2.1. It is essential that the vibrating proof-masses are anti-phase with respect to each other so that the differential nature of the sensor is retained [3]. The anti-phase movement of the proof-masses also reduces the anchor loss, thus ensuring a high mechanical quality factor of the drive-mode.

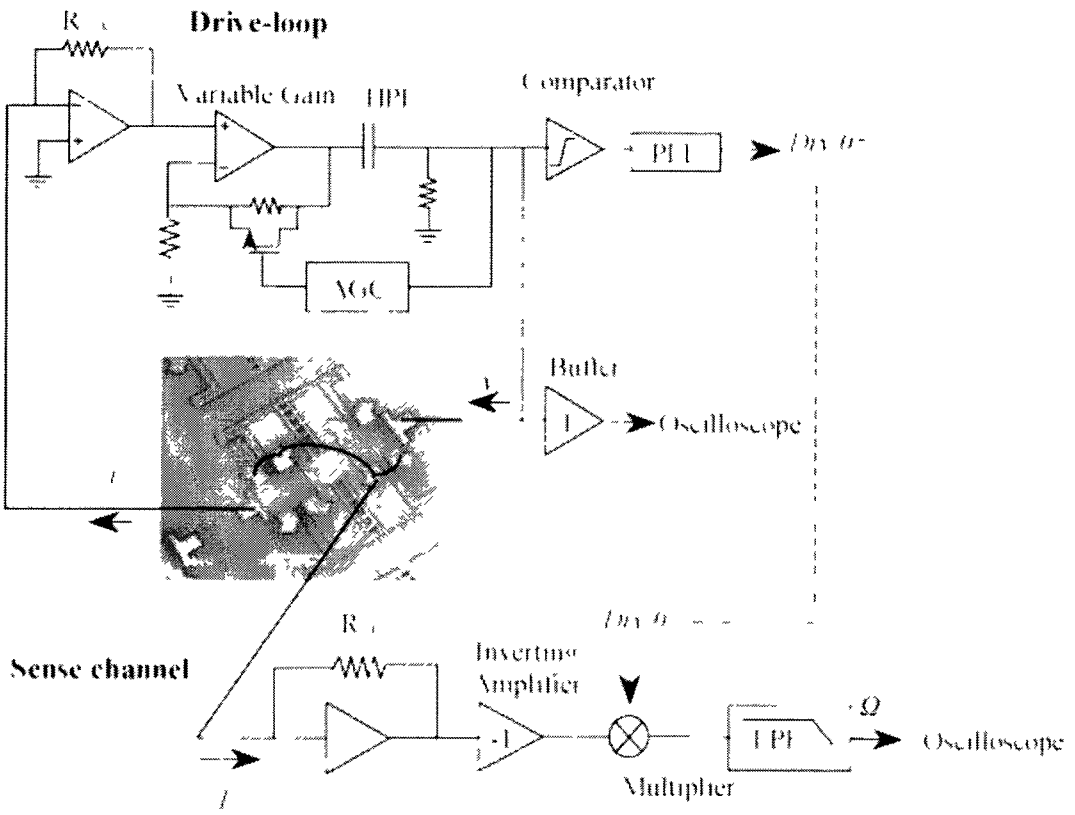

Figure 4.5: Schematic of the interface electronics for operating the MB-TFG

A high drive-Q is desirable in many ways. First, it can significantly ease the design of the drive resonant oscillator. The drive motional resistance of the MB-TFG is sometimes as high as 20MΩ in a vacuum, which requires a very large transimpedance gain from the sustaining circuitry in the drive loop. The high drive-Q reduces this motional resistance and loosens the large gain requirement. Second, a high drive-Q enables the oscillations to be built up and sustained at the required amplitude with much smaller AC voltage levels at the comb-drive electrodes, thereby dissipating less power. Third, the frequency stability of the oscillator is maximized when the drive-Q is maximized [25]. The mechanical structure with a high drive-Q forms an excellent narrow-band filter at the

desired resonant frequency, therefore stabilizes the oscillating frequency and also alleviates the linearity requirement on the driving voltage generated by the sustaining circuitry [3].

In Fig. 4.5, the drive loop configuration is very similar to the architecture presented in [51-53]. The drive motional current output from the MB-TFG is converted into voltage by the TIA front-end described before. This voltage is further amplified by a non-inverting amplifier stage with variable gain control implemented by an AGC circuit. The following RC High Pass Filter (HPF) removes any DC component in the signal and also provides some positive phase shift to help ensure a 0° loop phase shift. After passing the HPF stage, the voltage signal, which serves as the input driving voltage, is applied back to the MB-TFG, thus completing the drive loop. In accordance with Fig. 4.4, "Amplifier" A consists of the TIA front-end, variable gain amplifier, HPF and AGC, while the MB-TFG device is the "feedback network" β. During operation, theoretically, the MB-TFG provides 180° phase shift from the input voltage to output current, and the TIA front-end provides additional 180° phase shift. In practice, the HPF (or LPF) is used to compensate for any unexpected small phase shift. In addition, given that the oscillation frequency is below 20kHz, the bandwidth of the sustaining amplifiers is much larger than the oscillation frequency, so an excess phase shift is prevented.

Besides in the drive loop, the feedback driving signal is fed into a buffer so that it can be monitored using an oscilloscope. The buffer effectively isolates the sustaining feedback loop from other variations. In order to realize the automatic level control function, the feedback driving signal is also the input for the AGC circuitry. Finally, as shown in Fig. 4.5, a voltage comparator converts the driving signal into a rail-to-rail

digital signal and the Phase Locked Loop (PLL) [54] locks on to it and provides an accurate in-phase signal for the sense channel processing.

4.2.3 Automatic Gain Control

The AGC circuit is based on the architecture presented in [55]. It is the key part of the drive loop electronics and is discussed here in detail. At system power-up, the AGC ensures a start-up loop gain of larger than 1 and then reduces it to be equal to 1 so as to keep a constant-amplitude oscillation, thereby preventing false rate outputs.

Fig. 4.6 shows the configuration of the AGC circuit. The peak detector detects the peak level of the input driving voltage signal and outputs it to the difference amplifier, where with the help of an external reference DC voltage V_{REF}, the AGC output voltage is generated. This voltage is then passed through a RC low pass filter to control the gate voltage of a MOS transistor, which is part of the feedback network of the non-inverting amplifier stage. By controlling the gate voltage of the MOSFET, its resistance and hence the gain of the amplifier can be controlled, resulting in a variable gain amplifier. Therefore, it is possible to tune the overall loop gain so that the drive-mode oscillation can be started and vibration amplitude can be controlled, using the AGC circuit.

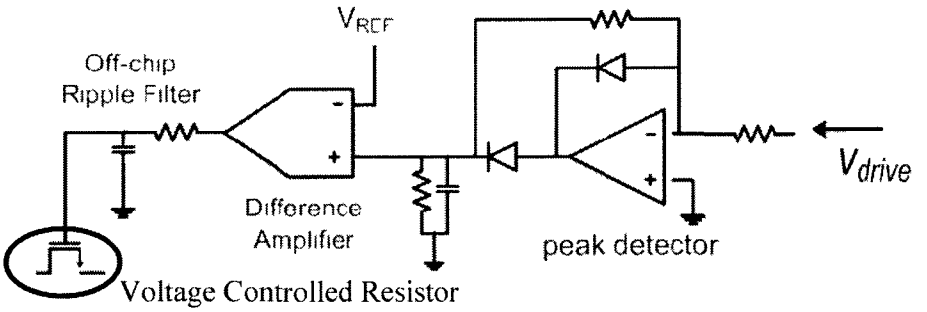

Figure 4.6 [3]: Configuration of the automatic gain control circuit

To gain a better understanding of the AGC circuit, the working principles of the peak detector and the difference amplifier are introduced.

1) Peak Detector

The peak detector measures the strength of an AC signal by its DC output. Although a classic rectifier (series diode) is often used, it cannot rectify a signal that is smaller than its own forward voltage. For small AC signals in this work, a precision half-wave rectifier (peak detector) is built, which combines the rectifying action of a diode and the accuracy of an operational amplifier. The precision rectifier is also known as a super diode. It behaves like an ideal diode or rectifier [56] and is useful in high-precision signal processing. Fig. 4.7 shows the schematic and the transfer characteristic of the precision rectifier.

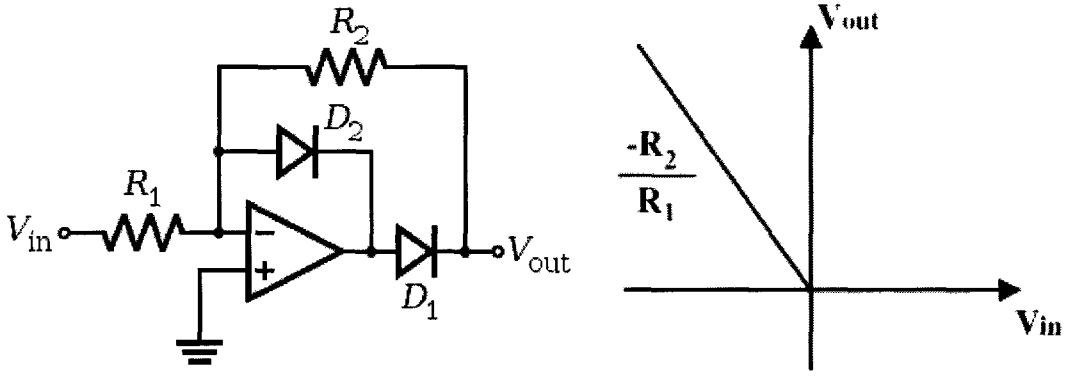

Figure 4.7 [57]: Schematic and transfer characteristic of the precision rectifier

The operation of this circuit is illustrated in Fig. 4.8. During the negative half-cycle of a sine-wave input, the output of the op-amp goes positive forcing D1 to turn on and D2 to shut off. The circuit looks and acts just like an inverting amplifier, except for a diode in

series with the output pin of the op-amp, which adjusts itself higher (by the diode's forward voltage, about 0.6V) to get the right voltage at the V_O. The classic inverting equation applies $V_O = -V_S R_2/R_1$. During the positive half-cycle, the output of the op-amp goes negative forcing D2 to turn on and D1 to shut off. The output voltage V_O is zero, because one side of R2 is connected to V- that is held at the virtual ground, and there is no current through R2, therefore $V_O = V_- = 0V$. During this half-cycle, the output of the op-amp swings negative enough in order to turn on D2 to pull the current through the diode [58].

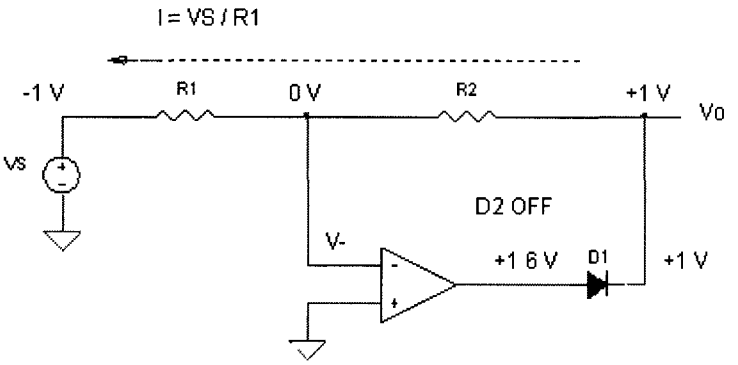

Negative half-cycle

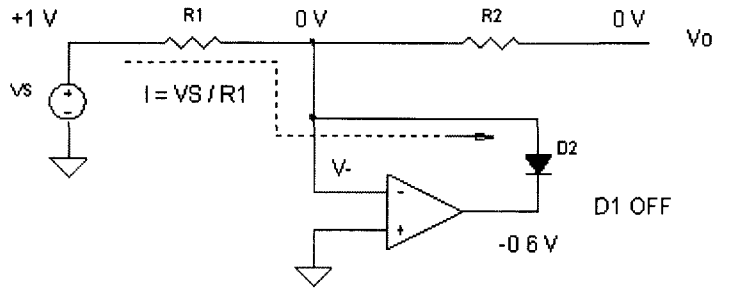

Positive half-cycle

Figure 4.8 [58]: Operations of an inverting precision half-wave rectifier

With a proper RC time constant at the output of the peak detector, the level of the input AC signal is represented by an output DC voltage.

2) Difference Amplifier

A difference amplifier, as the name suggests, is used to amplify the difference between two signals. As illustrated in Fig. 4.9, when all the resistors have the same value, the op-amp produces an output equal to the difference between the two inputs, which means unity gain.

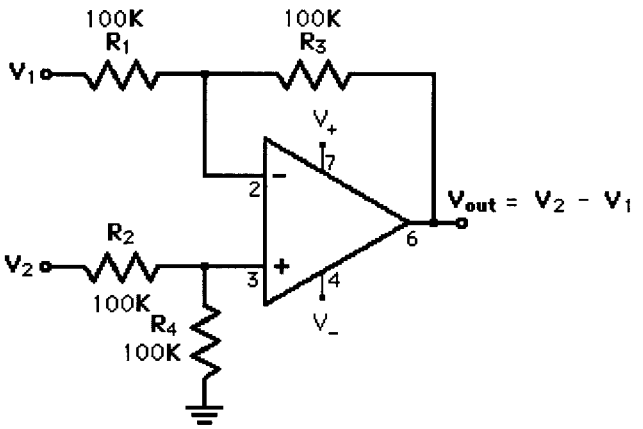

Figure 4.9 [59]: Schematic of a difference amplifier

The required DC level for controlling the resistance of the Metal-Oxide-Semiconductor Field-Effect Transistor (MOSFET) is achieved by connecting the two inputs of the difference amplifier to the peak detector output and an external reference DC voltage V_{REF}, respectively.

4.2.4 PSPICE Simulation

Various circuit simulations are done using Personal computer Simulation Program with Integrated Circuit Emphasis (PSPICE) to investigate the drive loop electronics. These simulations include the transient analysis and AC analysis of the drive oscillation circuit without AGC, study of the MOSFET resistance, transient analysis of the AGC circuit and the complete drive loop circuit. Fig. 4.10 shows the AC analysis of the drive oscillation circuit. Its purpose is to observe the loop gain of the oscillation loop, especially the phase shift of the loop gain. The simulation result in Fig. 4.11 confirms that the phase shift of the loop gain is 0° at the resonant frequency of this circuit, thus a positive feedback loop results. Note that the gyroscope is modeled by a series RLC circuit in the simulation schematic.

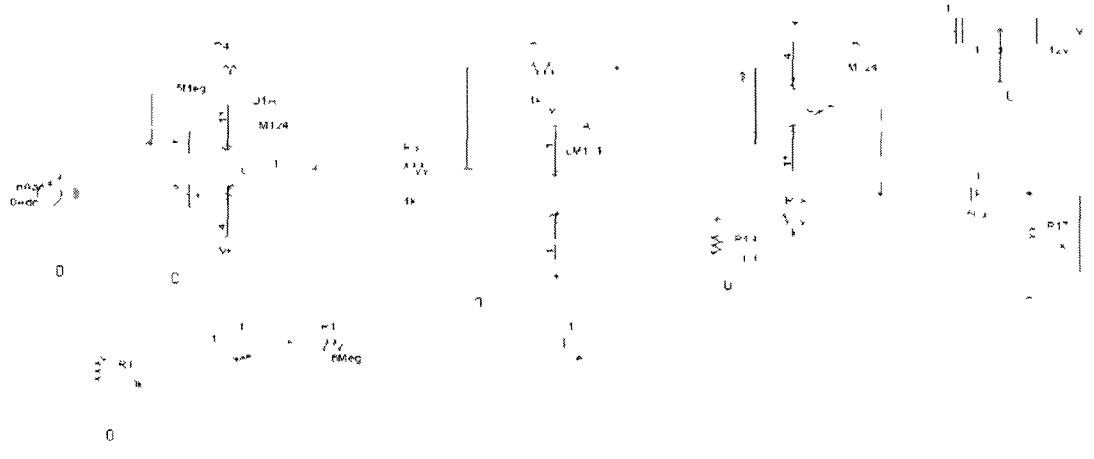

Figure 4.10: Schematic of AC analysis of the drive oscillation circuit

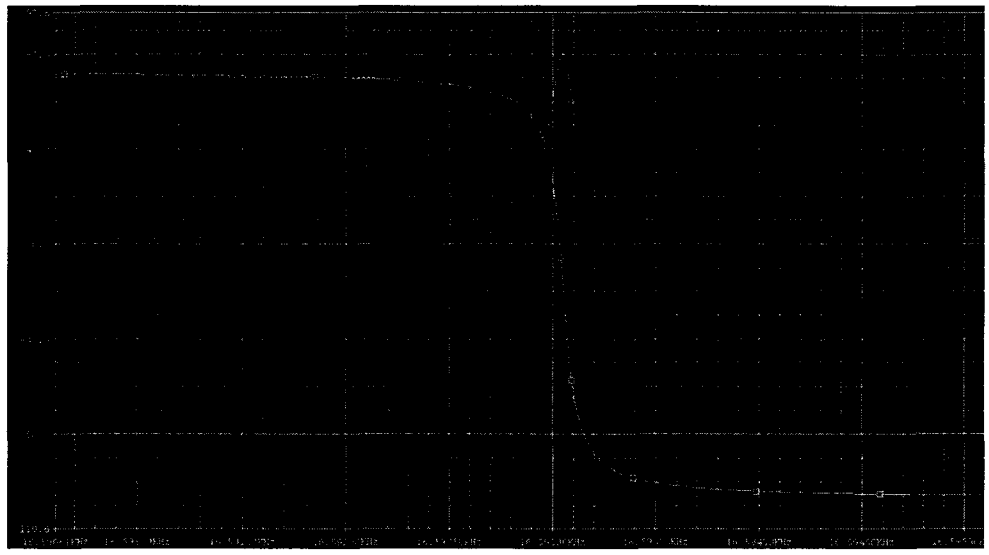

Figure 4.11: Simulation result showing a zero phase shift at the resonant frequency

The transient analysis of the complete drive loop circuit is presented in Fig. 4.12. To start the oscillation, an initial condition of a voltage of 10mV is provided to the capacitor C1 of the gyroscope model. The simulation time length is 1s, from which only the range of 0.9s to 1s is displayed. The simulation result in Fig. 4.13 shows a slowly growing oscillation signal at the drive resonant frequency of the gyroscope.

Accurate simulation of the oscillation with constant amplitude from this drive loop circuit proves to be difficult. However, the following experimental work verifies this design successfully.

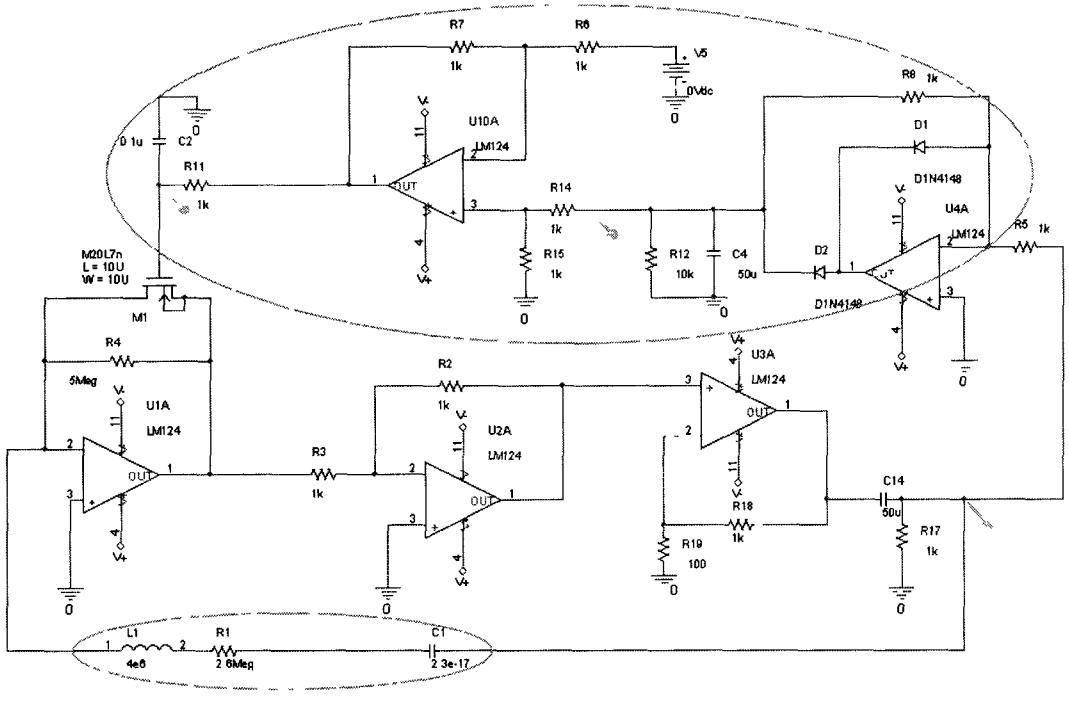

Figure 4.12: Schematic of transient analysis of the complete drive loop circuit

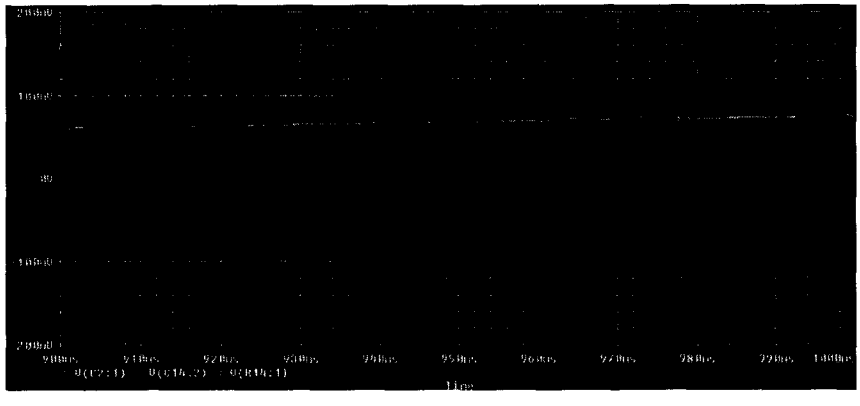

Overview of the oscillation signal

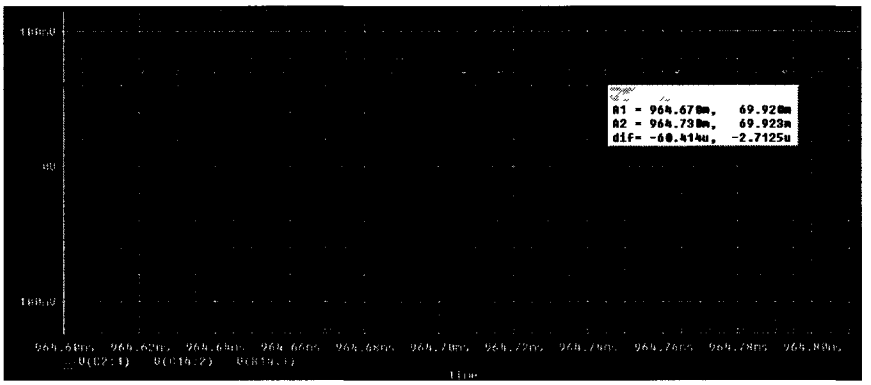

Close-up view of the oscillation signal

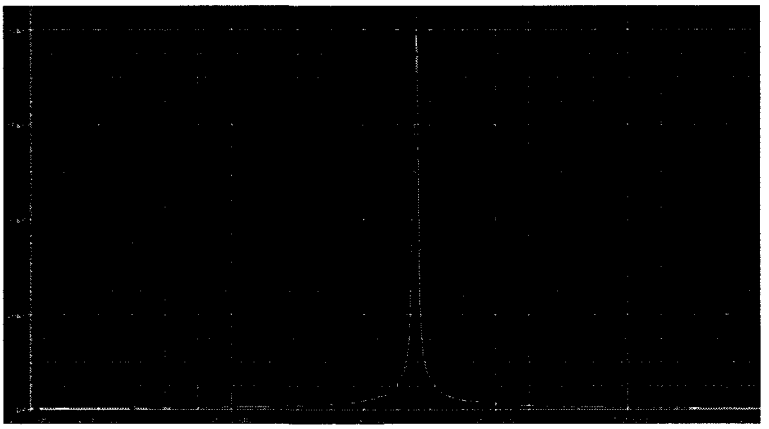

Spectrum of the oscillation signal

Figure 4.13: Simulation result showing the drive oscillation signal and its spectrum

4.3 Sense Channel Electronics

The sense channel is primarily responsible for extracting the input angular rate information from the gyroscope output. Modulated by the input rotation rate, this output is an Amplitude Modulation (AM) Coriolis Signal, and is demodulated using the drive oscillation signal. The final low-pass filtered output signal is proportional to the input rotation rate, and may be further amplified if necessary. Since the synchronous

demodulation technique used allows for phase sensitive detection and rejection of the quadrature error, it is preferred over other techniques such as envelope detection.

4.3.1 Phase Sensitive Demodulation

The MB-TFG in this work is referred to as in the open-loop mode because its sense-mode vibration is monitored but not controlled. When the gyroscope is subject to rotation about the z-axis, its proof-masses vibrate along the sense axis at the resonant frequency of the sensor. The vibration amplitude is modulated by the applied rotation rate signal. The displacement of the proof-masses, however, is attributed to both the Coriolis Acceleration and the quadrature error. These two signals can only be distinguished by the 90° phase difference between them. The reason for this phase difference lies in the fact that the Coriolis Acceleration is proportional to the velocity of the proof-masses along the drive axis, while the quadrature error is proportional to the position of the proof-masses. Therefore, the sense channel uses a synchronous I/Q (In-phase/Quadrature) demodulation technique to extract the input rotation rate information since it can differentiate the Coriolis Acceleration signal from the quadrature error signal, based on their different phase characteristics.

Recall the Coriolis Acceleration signal in Eq. 2.1, which is given again here

$$a_y = 2\Omega_z(t)v_x(t) = 2\Omega_z(t)q_d\omega_x cos(\omega_x t) \tag{4.16}$$

Note that it is actually an AM signal in which the drive-mode velocity of the proof-masses v_x is the carrier signal, while the input rotation rate Ω_z is the modulating signal. The direct output from the sense electrodes also takes this form as an AM signal. Hence,

the rotation rate Ω_z can be extracted by demodulating the sense output using a signal that is in phase with the drive-mode velocity of the proof-masses. In this case, the drive oscillation signal serves as this demodulating signal.

4.3.2 Circuit Configuration

The circuit configuration of the sense channel is included in Fig. 4.5 and is highlighted again here in Figure 4.14. The sense-mode vibration of the proof-masses is reflected by the variation of the parallel-plate sense capacitance that is formed by the proof-masses and the sense electrodes. The output current is an indication of this sense capacitance change and is the input signal to the sense channel electronics. From the previous analysis, a high sense-Q of the MB-TFG is also desirable because it improves the rate resolution and sensitivity of the gyroscope system.

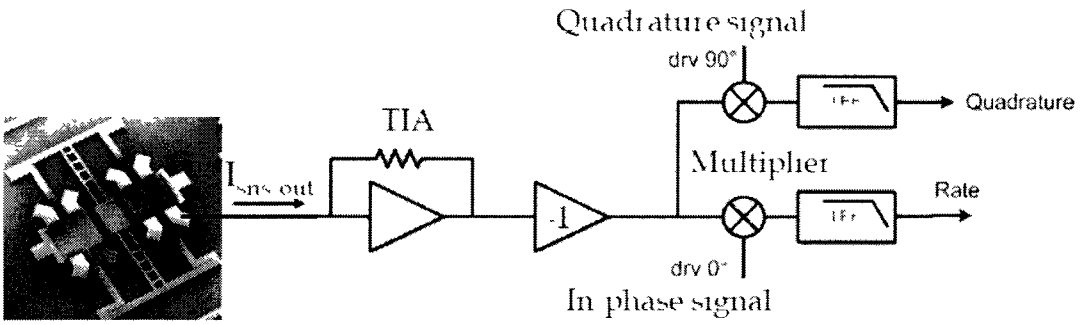

Figure 4.14: Circuit configuration of the sense channel

As in the drive loop, a TIA front-end converts the sense current into a voltage. The following stage of an inverting amplifier makes this voltage in phase with the sense current, thereby retaining the original phase characteristic of the Coriolis Acceleration

signal. The demodulation takes place at the multiplier stage, where the voltage is multiplied with the in-phase drive oscillation signal (drv 0°) from the PLL output in the drive loop. Mathematically, the trigonometric identities state that when multiplying two in-phase sinusoids with the same frequency, it gives

$$\sin(\omega t)\sin(\omega t) = \frac{1}{2}[\cos(\omega t - \omega t) - \cos(\omega t + \omega t)] = \frac{1}{2}[1 - \cos(2\omega t)] \tag{4.17}$$

$$\cos(\omega t)\cos(\omega t) = \frac{1}{2}[\cos(\omega t - \omega t) + \cos(\omega t + \omega t)] = \frac{1}{2}[1 + \cos(2\omega t)] \tag{4.18}$$

which implies that the multiplication results in a constant DC signal and a sinusoid signal with a doubled frequency. On the contrary, when multiplying two sinusoids with the same frequency but 90° phase difference, it gives

$$\sin(\omega t)\cos(\omega t) = \frac{1}{2}[\sin(\omega t + \omega t) + \sin(\omega t - \omega t)] = \frac{1}{2}\sin(2\omega t) \tag{4.19}$$

which implies that the multiplication results in a sinusoid signal with a doubled frequency only. In both cases, the double-frequency sinusoid can be removed by a Low Pass Filter (LPF). This means that during the demodulation, if the drv 0° signal from the PLL is used, then the input rotation rate information is retained while the quadrature error information is removed; if the drv 90° signal from the PLL is used, then the quadrature error information is retained while the input rotation rate information is removed. In this way, both the input rotation rate and the quadrature error signals can be monitored from the sense channel, as illustrated in Fig. 4.14.

This work only extracts the input rotation rate information. An active LPF is used to filter out the double-frequency component in the multiplier output so that the final output

is proportional to the input rotation rate Ω_z only. Additionally, a simple RC LPF stage could be added to smooth this voltage output if necessary.

The second-order active LPF employs a Sallen-Key Topology, which uses a unity-gain amplifier (0dB gain), as shown in Fig. 4.15. The Sallen-Key Topology is simple but has the advantage of a sharp transition between the pass and stop bands so that the interfering signal can be effectively reduced without degrading the desired signal. When $R_1 = R_2 = R$ and $C_1 = C_2 = C$, the cutoff frequency is given by $f_c = 1/2\pi RC$.

Table 4.1 summarizes the key electrical parameters of the sensor.

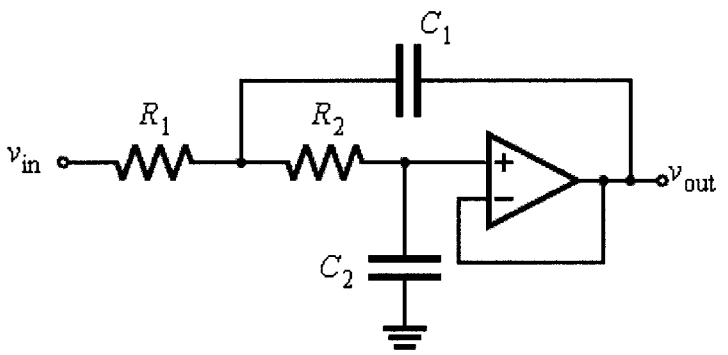

Figure 4.15 [60]: A unity-gain low-pass filter implemented with a Sallen–Key Topology

Table 4.1: Summary of the key electrical parameters of the sensor

Parameter	Measured Value
Sensor capacitive sensitivity	$4.1aF/°/s$
Amplitude of drive voltage applied	$170mV$
Minimum detectable ΔC (at 16.8kHz)	$0.46aF/\sqrt{Hz}$
System rate sensitivity	$80\mu V/°/s$
Output voltage noise level at 4Hz	$9\ \mu V/\sqrt{Hz}$
System rate noise floor	$400°/hr/\sqrt{Hz}$
Power supply	$\pm 5V$

CHAPTER V

PERFORMANCE CHARACTERIZATION OF THE MB-TFG

This chapter analyzes and examines the performance parameters of the prototype Silicon-On-Insulator (SOI) MB-TFGs. The main performance parameters include the quality factors in both the drive-mode and sense-mode, rate sensitivity, rate resolution and the overall bias stability of the system. Results from various characterization experiments of the MB-TFG system are highlighted and discussed.

5.1 Quality Factor Characterization

As stated before, quality factors in both vibration modes are a primary parameter for predicting the performance of a MB-TFG prototype, because it is closely related to almost all the important performance specifications of a gyroscope system such as the rate resolution, rate sensitivity and bias drift. This section presents an analysis of the quality factor and experimental results showing high Qs from both operation modes of the fabricated MB-TFGs.

5.1.1 Theoretical Analysis

In physics and engineering, the quality factor is a dimensionless parameter that describes how under-damped an oscillator or resonator is [61]. A higher Q indicates a lower rate of energy loss relative to the stored energy of the oscillator, and therefore, the oscillations die out more slowly.

For resonators, Q is defined as the ratio of the energy stored in the resonator to the energy supplied by a generator per cycle, in order to keep the signal amplitude constant at the resonant frequency f_0. The stored energy is constant with time

$$Q = 2\pi \times \frac{Energy\ Stored}{Energy\ dissipated\ per\ cycle} = 2\pi f_0 \times \frac{Energy\ Stored}{Power\ Loss} \tag{5.1}$$

As shown in Fig. 5.1, the quality factor also characterizes the bandwidth Δf of a resonator relative to its center resonant frequency f_0 [62]. For high values of Q, the following definition is mathematically accurate

$$Q = \frac{f_0}{\Delta f} \tag{5.2}$$

The bandwidth Δf is defined in terms of the frequency difference between the two -3dB points, where the vibration energy is half of the maximal value. A higher Q would result in a narrower and sharper peak in this figure.

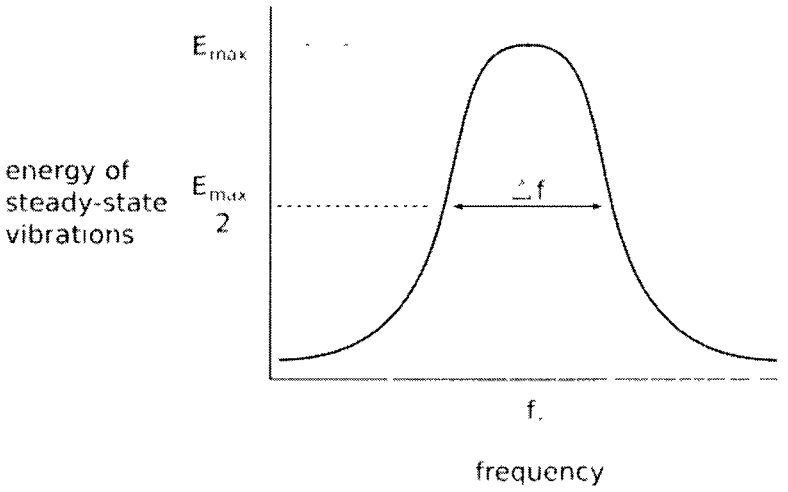

Figure 5.1 [63]: Definition of the Q factor of an oscillator

In electrical systems, the stored energy is the sum of energies stored in lossless inductors and capacitors, while the lost energy is the sum of the energies dissipated in resistors per cycle. Consider an ideal series RLC circuit, which is the electrical model of the MB-TFG, its Q is given by

$$Q = \frac{1}{R}\sqrt{\frac{L}{C}} \tag{5.3}$$

Similarly, in a single damped mass-spring mechanical system, the stored energy is the sum of the potential and kinetic energies stored in masses and springs, while the lost energy is the work done by an external force per cycle to counterbalance the effect of the damping force, so as to maintain constant vibration amplitude. The Q in this system is given by

$$Q = \frac{\sqrt{kM}}{D} \tag{5.4}$$

Eq. 5.3 and Eq. 5.4 are interchangeable according to the explanation of these model parameters in Chapter 2.

With regard to this gyroscope, the MB-TFS employed here is designed with an operation frequency above 10kHz to avoid any environmental noise [37] and below 20kHz to keep the operation voltage at a relatively low level [2]. Since the MB-TFG is operated in vacuum, the energy loss mechanisms in the MB-TFS mainly include the Thermal-Elastic Damping (TED), anchor loss, and surface loss. The measured overall mechanical quality factor of a tuning-fork gyroscope in each operation mode is based on the sum of these losses [42]:

$$\frac{1}{Q_{measured}} = \frac{1}{Q_{TED}} + \frac{1}{Q_{anchor}} + \frac{1}{Q_{surface}} \tag{5.5}$$

where Q_{TED}, Q_{anchor} and $Q_{surface}$ denote the Q related to TED, anchor loss and surface loss, respectively. From the previous work [17, 42], it has been found that: 1) surface loss is negligible for a tuning-fork gyroscope, as compared to TED and anchor loss; 2) from the design perspective, TED is the sole dominant loss in a similar tuning-fork structure with a flexural structure of three beams in parallel; 3) however, significant amount of anchor loss is introduced to the structure by over-etching silicon dioxide underneath an anchor. Therefore, as compared to these similar tuning-fork structures [17, 42], a flexural structure of four beams in parallel is incorporated in this MB-TFS design, in order to further reduce its TED and meanwhile keep the operation frequency in the desired range of 10kHz ~ 20kHz. The anchor loss can be significantly reduced by the improved mask design, as discussed in Chapter 3.

To ensure a low TED in the MB-TFS design, a numerical model of TED based on a thermal-energy method is developed to evaluate the Q_{TED} in the two operation modes. Based on the work in [42, 64], the distribution of TED in the two operation modes of the MS-TFS with a beam width of 9.8μm is shown in Fig. 5.2. As illustrated in this figure, TED mainly occurs in the beams along the drive axis in the drive-mode, and along the sense axis in the sense-mode. This is expected since the beams along the drive axis function as the mechanical spring for the drive-mode, while the beams along the sense axis act as the mechanical spring for the sense-mode. The simulated resonant frequency and Q_{TED} of the drive-mode and sense-mode are 15.69kHz and 260,023 for the drive-mode, and 15.841kHz and 211,740 for the sense-mode.

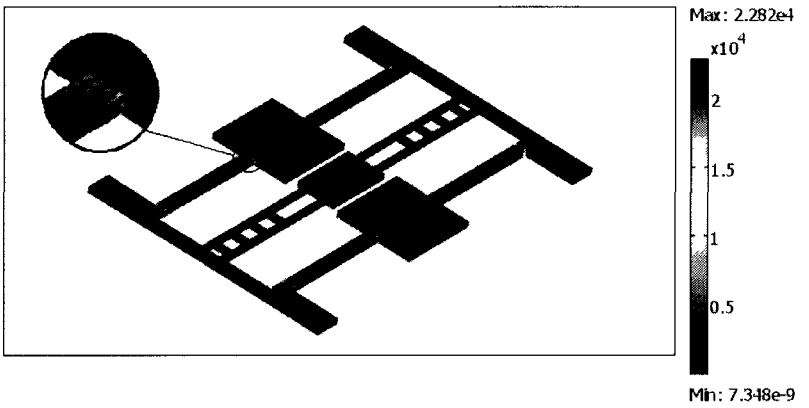

(a) Drive-mode

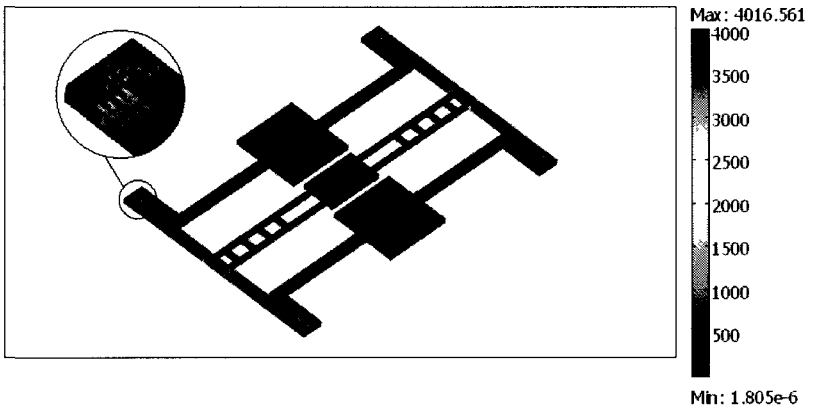

(b) Sense-mode

Figure 5.2: Distribution of TED in two operation modes of the MB-TFS

With the proof-masses being kept at the same dimension, the curved lines in Fig. 5.3 show that Q_{TED} in both operation modes decreases with the beam width and the resonant frequency. The Q_{TED} of the drive-mode is slightly higher than that of the sense-mode for a MB-TFS, because the MB-TFS experiences more dilatation in the sense-mode than in the drive-mode, under the same vibration amplitude. The different dots in Fig. 5.3 are the measured values of this design for comparison with the simulated results and will be explained later.

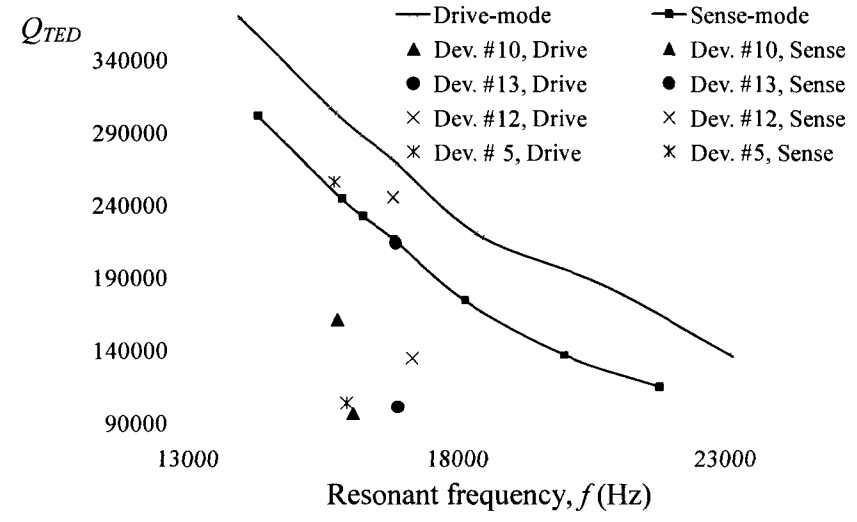

(a)

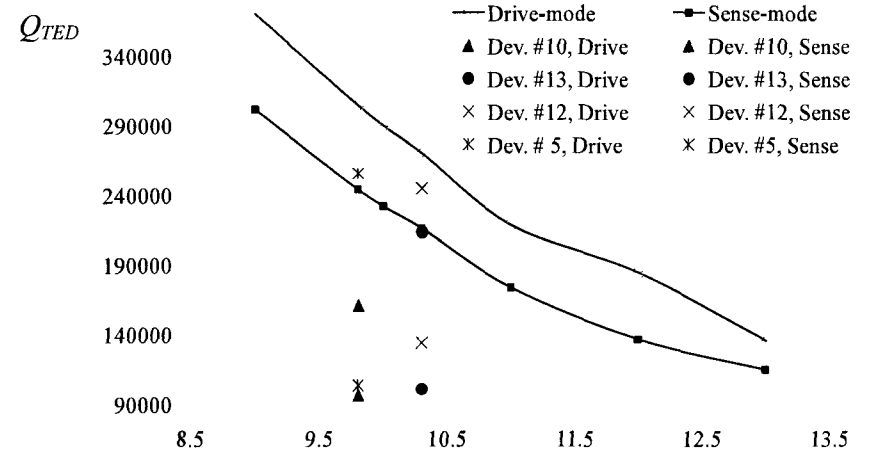

(b)

Figure 5.3: The relation of the calculated Q_{TED} of the drive-mode and the sense-mode versus (a) resonant frequency and (b) beam width of the MB-TFS (the proof-masses are kept at 400μm × 400μm × 30μm), together with measured Q values of this design provided in Table 5.2.

Anchor loss is caused by the load at the clamped region of a mechanical structure during vibrations. In the drive-mode vibrations, the normal stress at the clamped region of the MB-TFS gives rise to anchor loss, as shown in Fig. 5.4. According to the previous

work on anchor loss in a tuning-fork gyroscope [42], the Q related to anchor loss in the drive-mode is expected to be well above 9×10^{15}, simply due to the symmetric structure and the symmetric mode shape. As shown in Fig. 5.5, since there is a net torque applied on the anchor in the sense-mode vibrations of the MB-TFS, the Q related to anchor loss in the sense-mode is expected to be much smaller than its counterpart in the drive-mode.

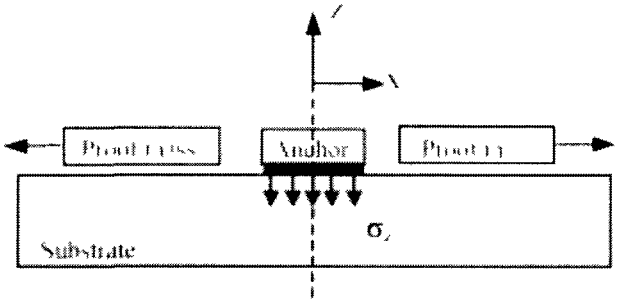

Figure 5.4: Schematic view of the normal stress along the *z*-axis at the anchor giving rise to anchor loss in the drive-mode (out of proportion for clear illustration)

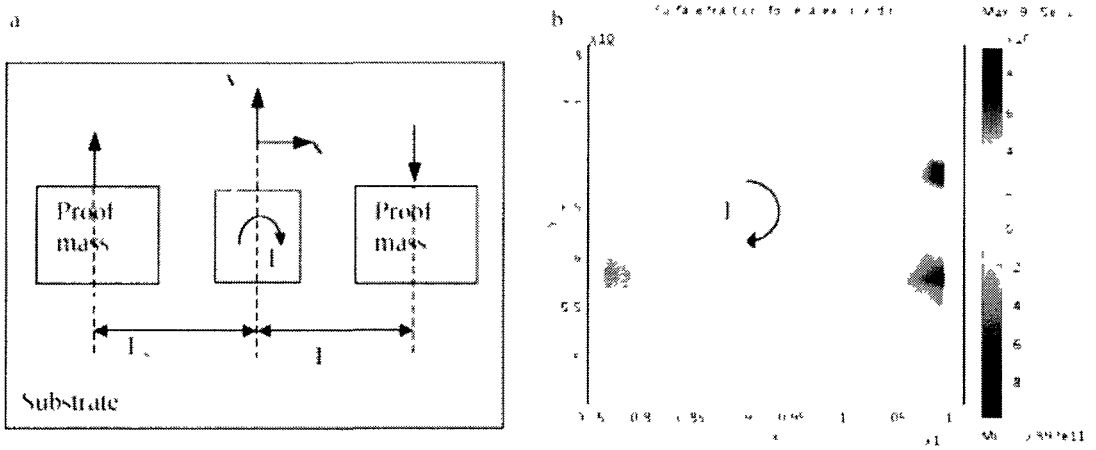

Figure 5.5: The torque about the *z*-axis at the anchor giving rise to anchor loss in the sense-mode (a) schematic view (out of proportion for clear illustration) and (b) simulated distribution of the normal stress along the sense-mode direction

5.1.2 Frequency Response of the MB-TFG

Following fabrication of the MB-TFGs, the frequency response measurement is performed to find out the resonant frequencies and the quality factors of the drive-mode and sense-mode. Figs. 5.6 and 5.7 show a schematic view and a picture of the experimental setup for measuring the drive-mode frequency response of a MB-TFG in vacuum. The device is tested in vacuum condition in order to eliminate the effect of air damping. A die of the fabricated gyroscopes is fixed on a Printed Circuit Board (PCB) and a MB-TFG device is wire-bonded to the pads that are connected to a TIA front-end with a feedback resistor of $R_F = 5.1M\Omega$. The PCB is then placed in a customized vacuum chamber and an Agilent 4395A network analyzer is connected to the device in a two-port configuration for measuring its frequency response in vacuum. This configuration is presented in Fig. 2.4. With a polarization DC voltage $V_P = 20V$ applied on the tuning-fork structure, an AC drive voltage signal v_{in} is applied on one comb-drive electrode, and then a sense current signal i_{out} can be detected from the other comb-drive electrode, which is further converted into a voltage output v_{out} through the TIA front-end. Likewise, to measure the sense-mode frequency response of the device, an AC voltage signal v_S is applied to the tuning electrodes and the sense current signal i_S can be detected from the four sense electrodes.

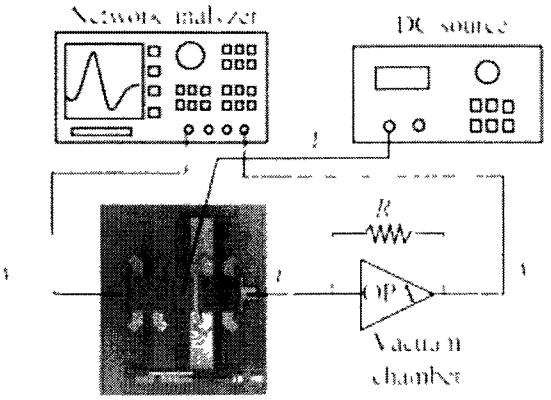

Figure 5.6: Schematic view of the experimental setup for measuring the frequency response of a MB-TFG

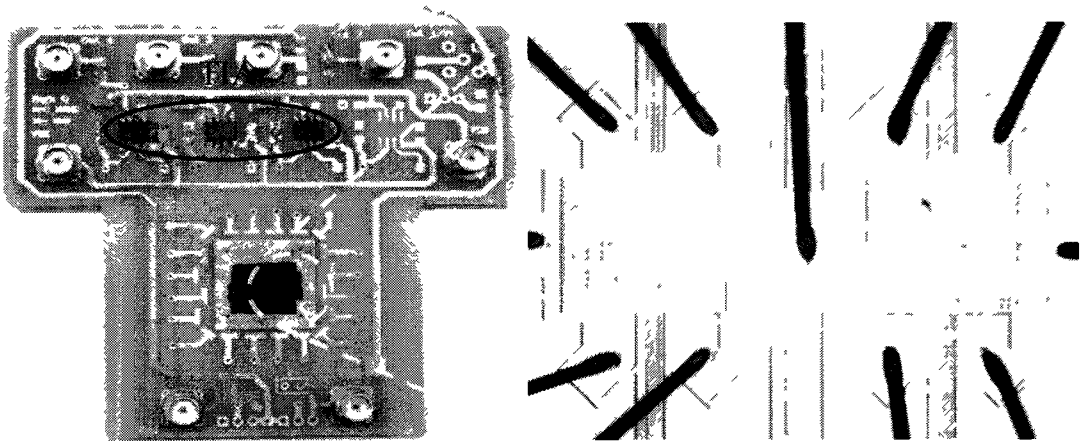

Figure 5.7: Picture of the PCB used in frequency response measurement and a close-up view of the wire-bonded MB-TFG device on the die

Before discussion on the measured Q values, the loading effect of the interface electronics on the mechanical Q of the MB-TFG is revisited. As stated in Chapter 4, the Q-loading effect can be minimized with a TIA front-end because of its low input impedance. This can be confirmed by considering the damping from the experimental

electronics or $Q_{electronics}$. As described in [42], from the perspective of a mechanical system, $Q_{electronics}$ is given by

$$Q_{electronics} = \frac{\sqrt{kM}}{V_P^2(\frac{dC}{dx})^2 R_{IN}} \tag{5.6}$$

while from the perspective of an equivalent electrical system, $Q_{electronics}$ is given by

$$Q_{electronics} = \frac{\omega L_{io}}{R_{IN}} \tag{5.7}$$

These two equations are essentially the same but from different perspectives. Since the R_{IN} for a TIA front-end is very low, $Q_{electronics}$ is at least on the order of 10^6, which means a negligible influence to the measured Q values. Therefore, the term of $Q_{electronics}$ is omitted in the right hand side of Eq. 5.5 above.

Fig. 5.8 shows the measured highest Q values, 255,550 in the drive-mode and 103,390 in the sense-mode, of a MB-TFG at the resonant frequency of 15.7kHz (corresponding to Device #5 in Table 5.2). From the measured Insertion Loss (IL) of the gyroscope at resonance, its motional resistance can be extracted using the following expression [25]

$$R_{motional} = R_F \times 10^{-\frac{IL}{20}} \tag{5.8}$$

Because the motional resistance of the MB-TFG, together with the TIA stage, forms an inverting amplifier, and the IL measured by the network analyzer becomes the magnitude of the voltage gain of $R_F / R_{motional}$ in dB.

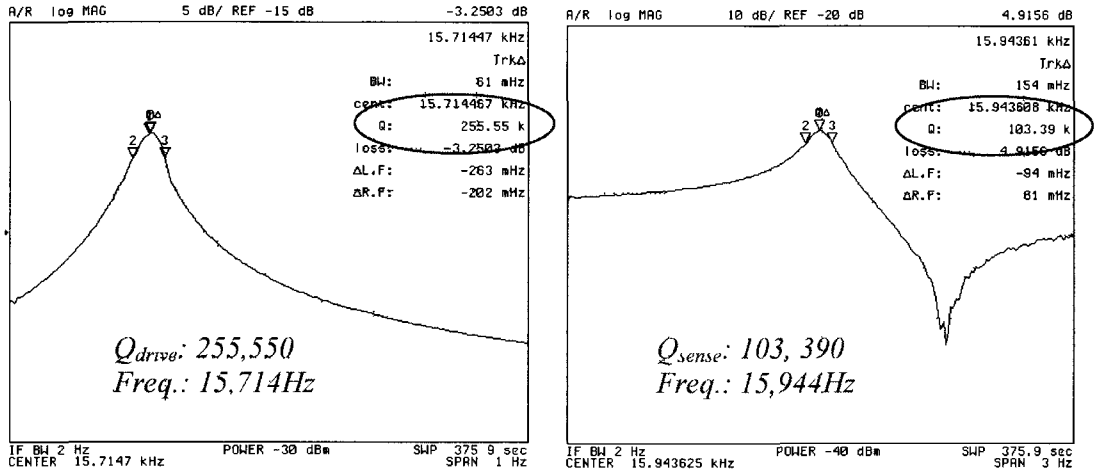

(a) Drive-mode (b) Sense-mode

Figure 5.8: Measured frequency response of Device #5 in Table 5.2, with the polarization voltage of $V_P = 20V$.

Table 5.1 provides the measured results of the drive-mode and sense-mode frequency response of this fabricated MB-TFG and compares them with the designed values. Based on Eq. 2.15 and Eq. 2.22, and from the measured motional resistances and Qs, the actual fabricated sense/tuning gap is calculated to be $d_{s0} = 4.9\mu m$ and the gap between comb fingers to be $g = 6.9\mu m$, which are consistent with the dimensions shown in Fig. 3.7.

The measured resonant frequencies, Qs, and motional resistances of fabricated MB-TFGs from two wafers, are summarized in Table 5.2, clearly showing that, for each wafer, the fabrication variation has a very trivial effect on the resonant frequency, but significant influence on the Q value and consequently on the motional resistance. Based on the measured resonant frequency, the beam width is found to be 9.8μm and 10.3μm for the fabricated gyroscopes on Wafer #1 and Wafer #2, respectively. Overall, the measured frequency response of the fabricated devices is consistent across a wafer, in the sense that

the Qs of the drive-mode are typically about 200k, while the Qs of the sense-mode are around 100k. The motional resistances in both modes show a similar consistency.

The measured Q values of four devices are included in Fig. 5.3 for comparison. Devices #5 and #12 demonstrate the highest measured Qs from the two wafers, while Devices #10 and #13 are used for rate sensitivity characterization in the following subsection. The same symbol is used for a device. The symbol with a lower value represents the measured Q in the sense-mode and the one with a higher value represents the measured Q in the drive-mode. The comparison between the measured Q values and the simulated Q_{TED} values clearly shows once again that TED is the dominant loss in the drive-mode and is also significant in the sense-mode.

Table 5.1: Summary of the designed and measured parameters of the drive-mode and sense-mode of the MB-TFG from the frequency response with polarization voltage of $V_P = 20V$

Parameter	**Designed value**		**Measured value (V_P=20V)**		**Symbol (unit)**
	Drive-mode	Sense-mode	Drive-mode	Sense-mode	
Resonant frequency	15.694	15.842	15.714	15.944	*f (kHz)*
Equivalent stiffness	243	337	-	-	*k* (μN/μm)
Equivalent mass	25	34	25	34	*M* (μg)
Q_{TED}	260,023	211,740	-	-	-
$Q_{measured}$	-	-	255,550	103,390	-
Electromechanical coupling coefficient	0.0664[a]	0.307[a]	0.0385	0.115	η (μN/V or pC/μm)
	0.0385[b]	0.115[b]			
Equivalent inductance	5.67[a]	0.36[a]	-	-	*L* (MH)
	16.87[b]	2.57[b]			
Equivalent resistance	2.19[a]	0.35[a]	7.41	2.90	$R_{motional}$ (MΩ)
	6.52[b]	2.47[b]			
Equivalent capacitance	1.81×10^{-5} [a]	2.83×10^{-4} [a]	-	-	*C* (pF)
	6.08×10^{-6} [b]	3.94×10^{-5} [b]			

[a] Value calculated using the designed comb finger gap of 4μm or the designed sense/tuning gap of 3μm

[b] Value calculated using the fabricated gap between comb fingers of 6.9μm or the fabricated sense gap of 4.9μm

Table 5.2: Summary on the measured resonant frequencies, Qs, and motional resistances of fabricated MB-TFGs from two wafers, with the polarization voltage of V_P = 20V

Device No.	Drive-mode			Sense-mode		
	f(kHz)	Q	$R_{motional}$ (MΩ)	f(kHz)	Q	$R_{motional}$ (MΩ)
Wafer #1						
Device # 1	15.683	210.81k	9.1	16.237	106.5k	3.5
Device # 2	15.752	143.8k	11.2	16.166	157.81k	2.8
Device # 3	15.914	231.8k	8.9	15.988	105.42k	2.8
Device # 4	15.702	201.46k	9.4	15.797	144.48k	2.9
Device # 5	15.714	255.55k	7.4	15.944	103.39k	2.9
Device # 6	15.673	201.32k	10.4	15.666	116.43k	3.0
Device # 7	15.771	247.48k	6.9	15.911	107.79k	2.5
Device # 8	15.841	197.43k	8.9	15.976	100.20k	3.6
Device # 9	15.972	236.34k	11.0	16.189	88.569k	3.6
Device # 10	15.761	168.48k	8.2	16.056	96.225k	3.1
Wafer #2						
Device # 11	16.868	178.47k	8.5	17.146	84.605k	2.8
Device # 12	16.800	244.97k	7.2	17.162	134.14k	1.8
Device # 13	16.842	213.75k	10.7	16.884	100.7k	2.2

5.2 Rate Sensitivity Measurement

Upon finishing the quality factor characterization, the MB-TFG system is set up and run in vacuum in order to measure its rate sensitivity. As mentioned earlier, reducing the frequency difference between the two operation modes is critical for achieving high rate sensitivity in a gyroscope. Therefore, electrostatic frequency tuning must be performed prior to measuring the rate sensitivity, so that the sense-mode frequency, which is designed to be slightly higher, can be tuned down to match with the drive-mode frequency. Note that this step is still carried out using the PCB in Fig. 5.7, since it is also a frequency response measurement. The DC polarization voltage V_P on the tuning-fork structure and the DC tuning voltage V_T on the four tuning electrodes are adjusted to meet this need, as shown in Fig. 5.9. However, due to inadequate electrodes dedicated to quadrature error nulling, perfect matched-mode condition (0Hz frequency split) is not

achievable, resulting in a minimal finite frequency difference between the two operation modes.

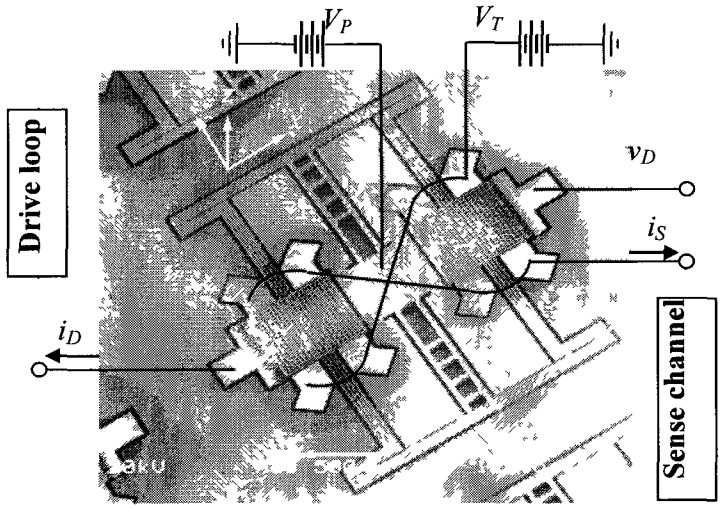

Figure 5.9: Signal configuration of the MB-TFG for rotation rate detection

Two MB-TFGs, Devices #10 and #13 (in Table 5.2), are tested for their frequency response in order to find out the values of V_P and V_T, at which the minimal frequency difference is reached. Device #10's frequency difference can be monitored by applying an AC voltage to the set of the sense electrodes and feeding the output signal from one comb-drive electrode into the network analyzer, which corresponds to using v_S as the input and i_D as the output in Fig. 2.4. Both the V_P and V_T are adjusted manually to reduce this frequency difference. With V_P at 70V and V_T at ground level, a minimum frequency difference of Δf = 7Hz is achieved at about 15.7kHz, as plotted in Fig. 5.10 (a). The two modes show similar magnitudes because they are realized by the same mechanical structure and thus interfere with each other under a small frequency difference. At this

frequency difference, the frequency response of the drive-mode and sense-mode of the MB-TFG is measured again, using still the signal configuration for frequency response shown in Fig. 2.4. The results are shown in Figs. 5.10 (b) and 5.10 (c) for obtaining their Qs and motional resistances, since these parameters are functions of the two DC voltages, V_P and V_T. Here the drive and sense Qs are 95,000 and 26,000, respectively. The same procedure for frequency tuning is implemented on Device #13. For this device, V_T is also at ground level and V_P is at 29V when a minimum frequency difference of Δf = 4Hz is achieved at about 16.8kHz, as plotted in Fig. 5.11 (a). The frequency responses of both modes under this frequency difference are shown in Figs. 5.11 (b) and 5.11 (c), respectively, showing a drive Q of 90,000 and a sense Q of 92,000. Based on these measured results, the theoretical rate resolution and rate sensitivity of both MB-TFGs are calculated and listed in Table 5.3. The theoretical rate sensitivity included in this table is calculated using Eq. 2.6, with the assumption that the frequency difference is Δf = 0Hz and the measured Q in the sense-mode listed in the table serves as the Q_{EFF}.

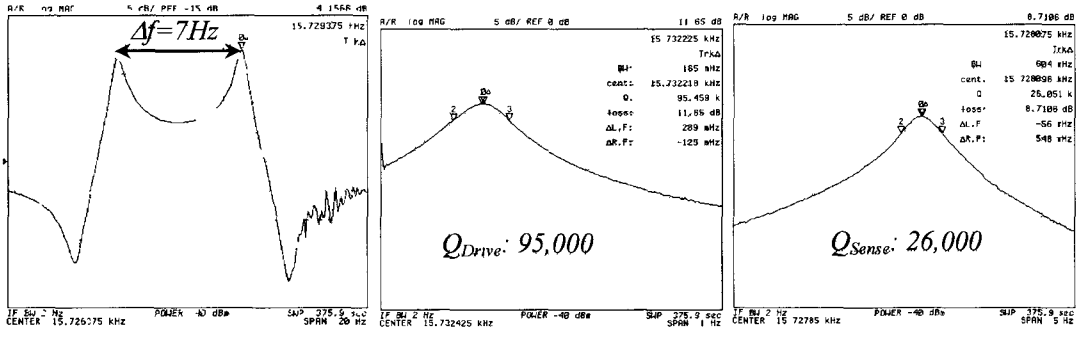

(a) (b) (c)

Figure 5.10: Frequency tuning for Device #10, (a) a minimum frequency difference of Δf=7Hz at about 15.7kHz, with V_P=70V and V_T=0V (b) measured frequency response of the drive-mode at Δf=7Hz and (c) measured frequency response of the sense-mode at Δf=7Hz

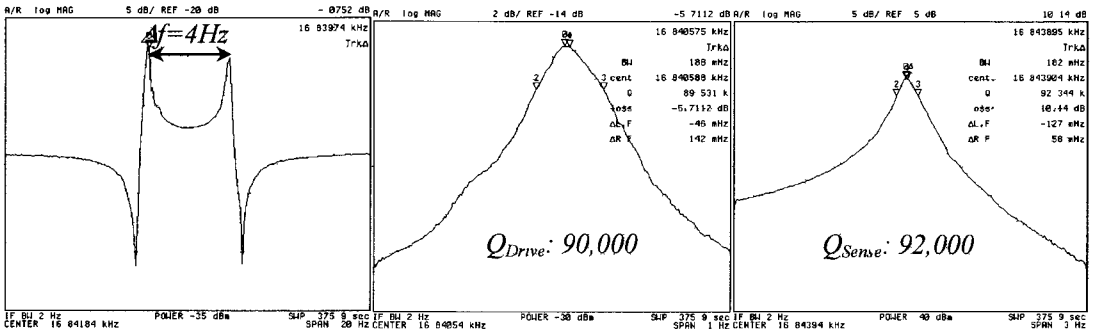

(a) (b) (c)

Figure 5.11: Frequency tuning for Device #13, (a) a minimum frequency difference of Δf=4Hz at about 16.8kHz, with V_P=29V and V_T=0V (b) measured frequency response of the drive-mode at Δf=4Hz and (c) measured frequency response of the sense-mode at Δf=4Hz

When the required polarization voltage V_P and tuning voltage V_T for a MB-TFG device to reach its minimal frequency difference between the two operation modes are found, the interface electronics can be added to the gyroscope to set up the angular sensor system shown in Fig. 5.9. According to the circuit analysis in Chapter 4, this system was first built and tested based on a PCB and a circuit breadboard, as shown in Fig. 5.12. The self-generated oscillation signal at the mechanical resonant frequency of the MB-TFG and the corresponding in-phase PLL signal shown in Fig. 5.13 prove that the system is successful.

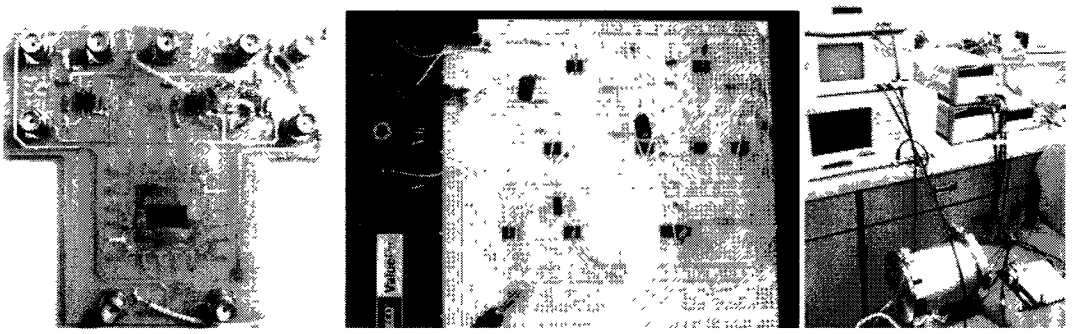

Figure 5.12: Picture of the sensor system on a PCB and a circuit breadboard

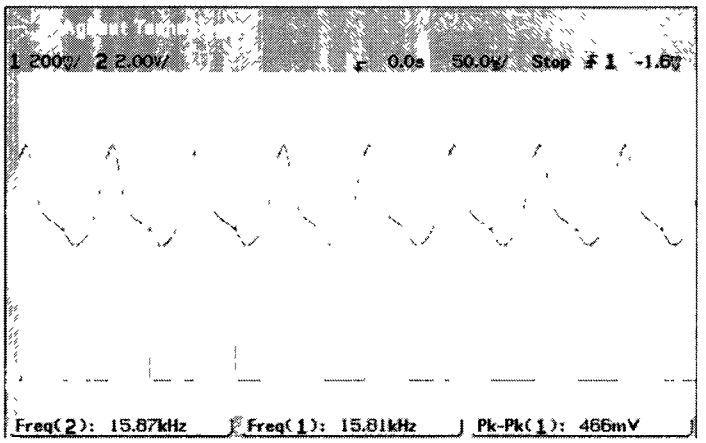

Figure 5.13: Preliminary result from the system showing the oscillation signal at mechanical resonance and the in-phase PLL signal

Since the breadboard circuit is easily disturbed by noises, a compact PCB design containing the complete interface electronics is necessary. The new PCB is designed using Protel DXP. Schematics of the drive loop and sense channel are created, based on which component footprints and their logic connections are automatically generated. The actual layout of the circuit board can be done manually or automatically. Fig. 5.14 shows the different function blocks in the complete schematic design. Fig. 5.15 shows the

manual-routed layout of the circuit board, and a picture of the new PCB with the complete sensor system installed.

The specific electrical components used to implement this system are listed in Table 5.3. The TIA front-end in the drive loop uses a 5MΩ potentiometer as the feedback resistor to provide extra flexibility for the loop gain tuning, while the TIA in the sense channel uses a 5.1MΩ feedback resistor, which is typically much larger than the motional resistance of the sense-mode, thus satisfying the requirement in Eq. 4.13 for low electronic noise. The non-inverting amplifier stage in the drive loop can provide a variable voltage gain up to about 8, therefore generating a maximum TIA gain of about 40MΩ in the drive loop. In experiment, C1 and R4 are actually implemented as a LPF, primarily for the loop gain phase concern. The inverting input of the voltage comparator 393 is directly grounded and a 6.8kΩ pull-up resistor is used at its open-collector output. The phase detector used in the HC4046 PLL is configured as the XOR phase detector [54]. The cutoff frequency of the Sallen-Key LPF in the sense channel is calculated to be 159Hz.

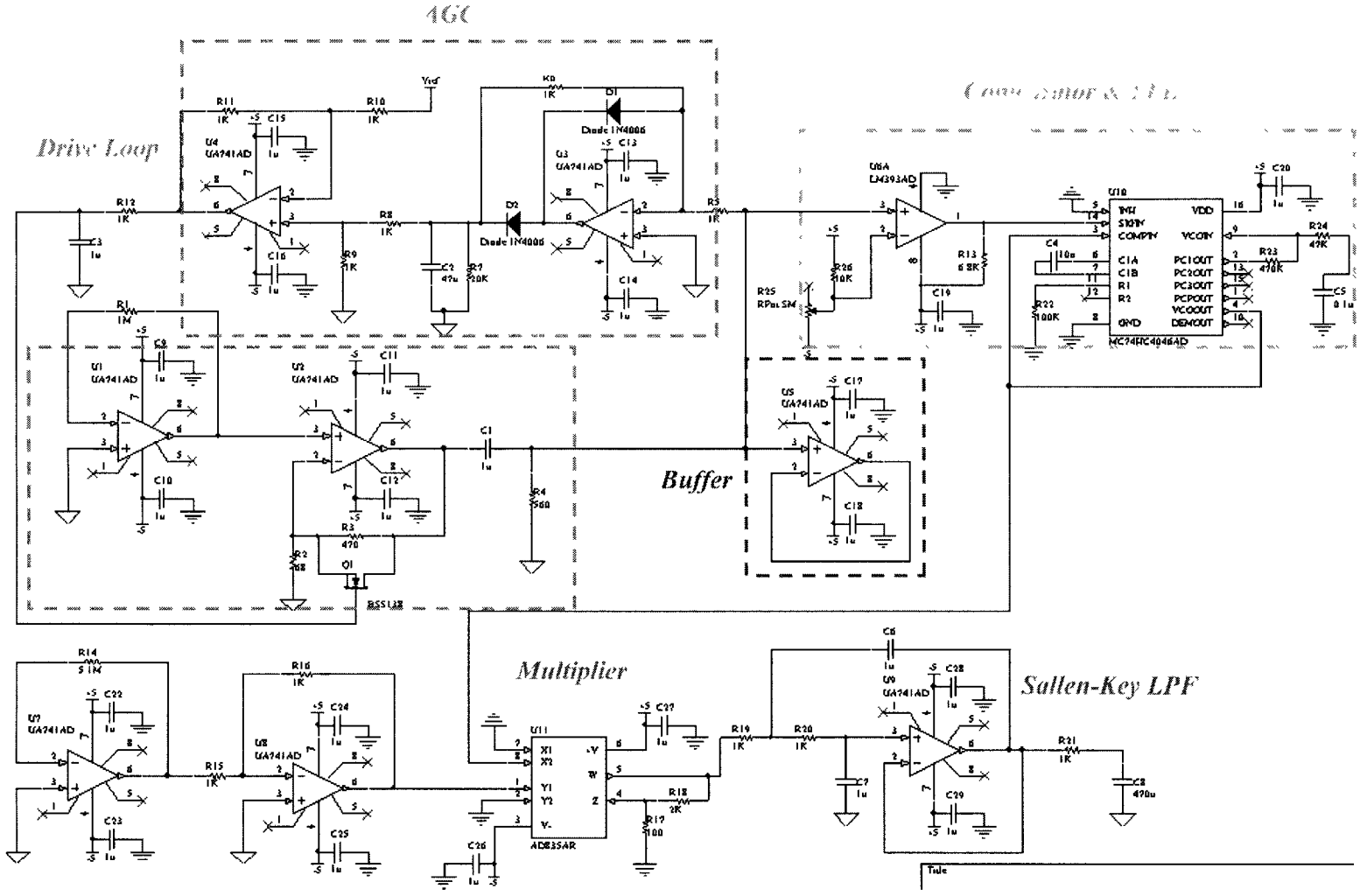

Figure 5.14: Schematics for the interface electronics

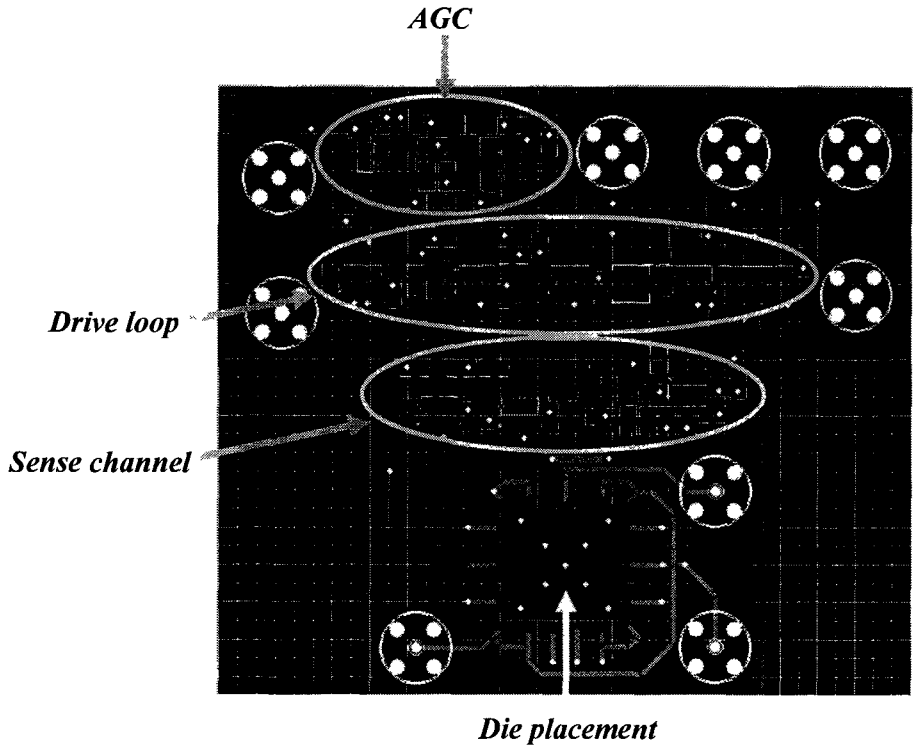

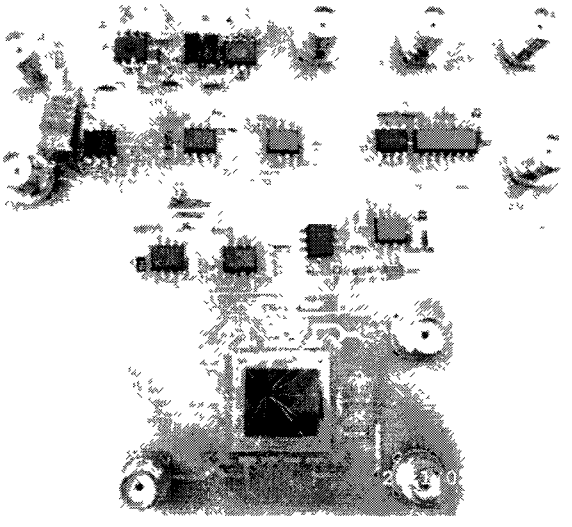

Figure 5.15: Manual-routed layout of the circuit board and picture of the new PCB with complete sensor system

Table 5.3: List of components used in the interface electronics

Component	Value or Name
U1, U2, U3, U4, U5, U7, U8, U9	OPA656U
U6	393
U10	HC4046AG
U11	AD835A
R1	5MΩ Potentiometer
R2	68Ω
R3	470Ω
R4, R5, R6, R8, R9, R10, R11, R12, R15, R16, R19, R20	1KΩ
R7	20KΩ
R13	6.8KΩ
R14	5.1MΩ
R17	100Ω
R18	2KΩ
R21, R26	10KΩ
R22	100KΩ
R23	470KΩ
R24	47KΩ
R25	Potentiometer
C1	4.7nF
C3, C6, C7, C9, C10, C11, C12, C13, C14, C15, C16, C17, C18, C19, C20, C22, C23, C24, C25, C26, C27, C28, C29	1μF
C2, C8	47μF
C4	10nF
C5	0.1μF
Q1	BSS138
D1, D2	ES1D

Using the new PCB system, the rate sensitivity of the two MB-TFGs, Devices #10 and #13, can be measured. Before running the system, by breaking the drive loop at the voltage feedback point, its loop gain characteristic can be observed by the network analyzer. The magnitude of the loop gain can be controlled by the VGA stage, while the total phase shift around the loop should be close to 0°. The magnitude and phase plots of the loop gain are presented in Fig. 5.16, showing that a positive feedback loop has been established.

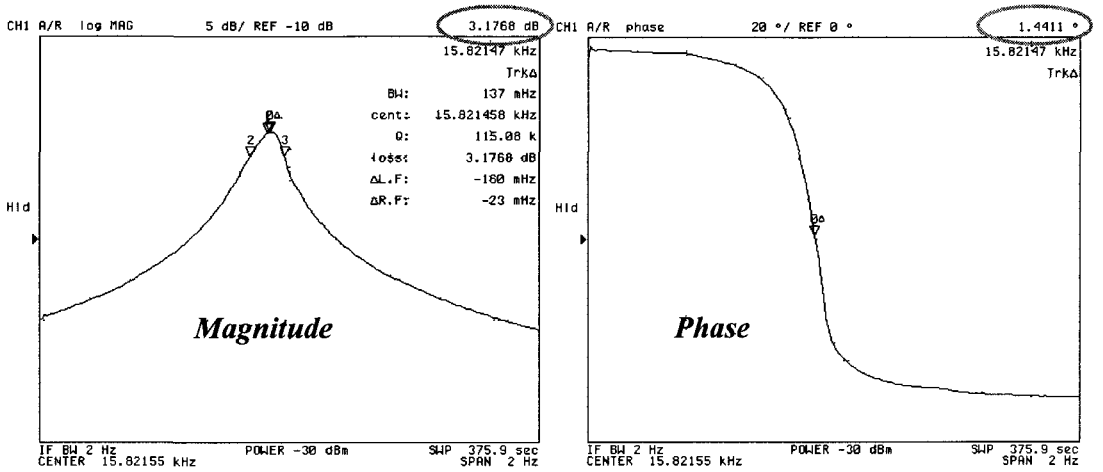

(a) (b)

Figure 5.16: Magnitude and phase plots of the loop gain showing a positive feedback drive loop

Figs. 5.17 (a) and 5.17 (b) show the buffered closed-loop oscillation waveforms with constant amplitudes of Devices #10 and #13, respectively. The oscillation frequency is 15.7kHz for Device #10 and 16.8kHz for Device #13, which correspond to their respective mechanical resonant frequency. The glitches at the peak and valley of the waveforms are due to electronic feed-through on the PCB. According to Eq. 2.16, the peak-to-peak voltage levels (V_{pp}) of 120mV and 347mV indicate that the drive-mode vibration amplitude of both devices is about 3.0μm. The drive-mode vibration amplitude can also be calculated using the measured motional current in the drive-mode, based on Eq. 2.17. Comparing to high drive voltages used in [13], the high drive-Q here allows for low drive voltages to achieve a large vibration amplitude in the drive-mode. Figs. 5.17 (c) and 5.17 (d) show the measured results of both MB-TFGs from the sense channel output in response to an input rotation rate signal of 45°/sec.

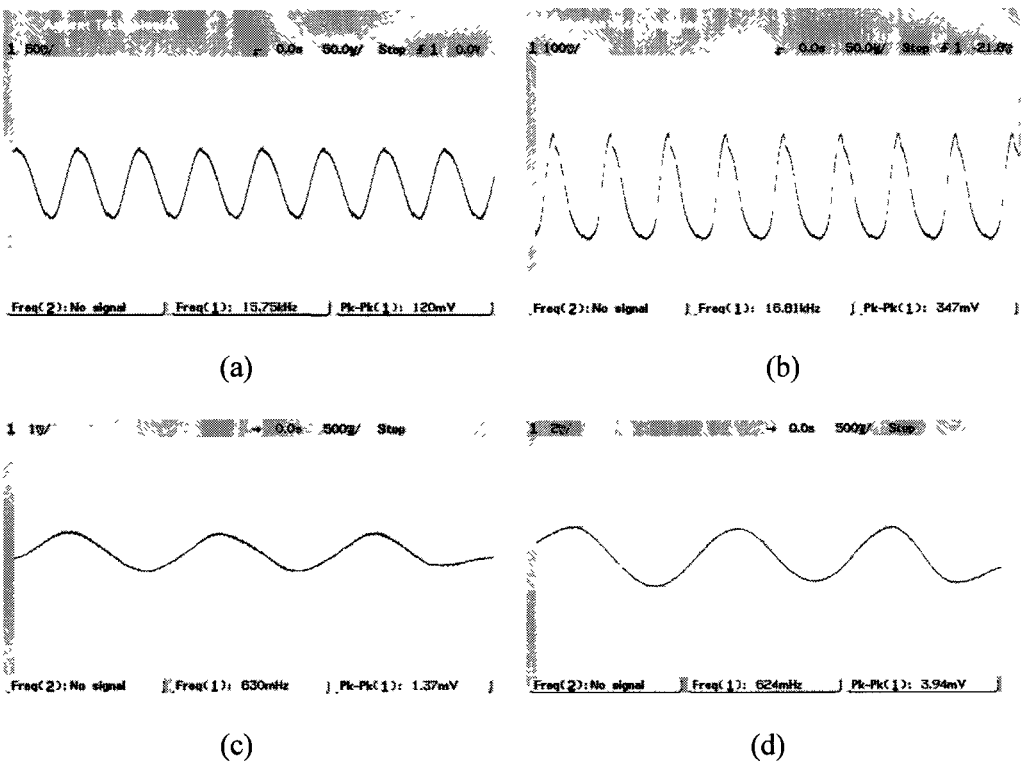

Figure 5.17: Measured results related to the rate sensitivity of the MB-TFG (a) Device #10: oscillation signal of the drive-mode vibration, V_{pp}=120mV corresponding to q_{Drive}=3.1μm (b) Device #13: oscillation signal of the drive-mode vibration, V_{pp}=347mV corresponding to q_{Drive}=3.0μm (c) Device #10: oscilloscope output, Vpp=1.37mV in response to a rotation rate signal of 45°/s (d) Device #13: oscilloscope output, Vpp=3.94mV in response to a rotation rate signal of 45°/s

As plotted in Fig. 5.18, the measured rate sensitivity is 30μV_{PP}/°/sec for Device #10 and 80μV_{PP}/°/sec for Device #13. The larger rate sensitivity of Device #13 is due to a larger Q in the sense-mode and a smaller frequency difference of the two operation modes, which means a better mode-matching. In order to get a clear output signal, the first-order LPF at the end of the sense channel has a very low cutoff frequency and therefore attenuates the observed signal level. Overall, the rate sensitivity for the two devices is obtained with an equivalent TIA gain of about 6MΩ in the sense channel.

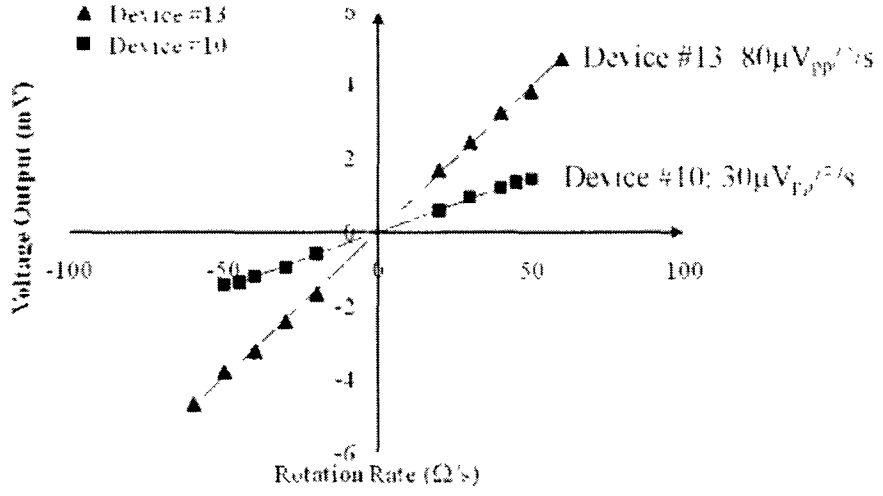

Figure 5.18: measured rate sensitivity of Device #10 with Δf=7Hz and Device #13 with Δf=4Hz

Table 5.4 summarizes the operation parameters and the key performance parameters of both MB-TFGs. Because of the difference between the polarization voltages, Device #10 has a motional resistance of only 1.33MΩ in the drive-mode, while it is 9.84MΩ for Device #13. This means a much larger effective TIA gain is needed in the drive loop for Device #13. Their motional resistances in the sense-mode are comparable (1.87MΩ for Device #10 and 1.59MΩ for Device #13), since although V_P is larger for Device #10, its sense-mode quality factor is much smaller than that of Device #13. The theoretical rate resolutions and rate sensitivities of Devices #10 and #13 can be calculated using Eqs. 2.2, 2.3, 2.4 and 2.7, and these results are also included in Table 5.4. ENEΩ is lower than MNEΩ basically because R_F (5.1MΩ) in the sense channel is larger than $R_{MOT\text{-}S}$.

From the foregoing results, it can be seen that the MB-TFG is a device with high sensitivity. Take Device #13 for example, for a given input rotation rate of 30°/s, the vibration amplitude of the proof-masses along the sense axis is only about 0.01μm.

Table 5.4: Summary of the operation parameters and performance parameters of two MB-TFGs

Parameter	Device #10	Device #13
Drive-mode vibration amplitude (q_{Drive})	3.1μm	3.0μm
Operation frequency (f_0)	15.7kHz	16.8kHz
Frequency difference (Δf, also BW)	7Hz	4Hz
Q in the drive-mode (Q_D)	95,000	90,000
Q in the sense-mode (Q_S)	26,000	92,000
Polarization voltage/tuning voltage (V_P, V_T)	70V,0V	29V, 0V
Measured Motional resistance in the drive-mode	1.33MΩ	9.84MΩ
Measured Motional resistance in the sense-mode	1.87MΩ	1.59MΩ
Equivalent impedance in the sense channel (R_{TIA})	6MΩ	6MΩ
Theoretical mechanical noise (MNEΩ)	0.614°/hr/√Hz	0.324°/hr/√Hz
Theoretical electrical noise (ENEΩ)	0.243°/hr/√Hz	0.177°/hr/√Hz
Theoretical total noise (TNEΩ)	0.66°/hr/√Hz	0.37°/hr/√Hz
Theoretical rate sensitivity with Δf=0Hz	4.313mV/°/s	5.913mV/°/s
Measured rate sensitivity	30μVpp/°/s	80μVpp/°/s

CHAPTER VI

BIAS DRIFT IN MEMS GYROSCOPES

Bias drift is another very important performance specification of the MB-TFG. It is used to refer to the bias stability or instability of a gyroscope system. This chapter focuses on this critical parameter and introduces the Allan Variance Technique for characterizing bias drift.

6.1 Introduction to Bias Drift

The output of a gyroscope in the absence of an input rotation rate is referred to as Zero Rate Output (ZRO) or gyroscope bias. Expressed in terms of angular rate (°/hr or °/s), the bias is an accurate measure of the long-term stability of a gyroscope. Bias drift is the variation of the gyroscope bias, which has systematic and random components. The systematic component is related to environmental conditions such as temperature, pressure, voltage fluctuations, and mechanical vibration. In many cases, these could be calibrated and compensated for in a system. The other component, however, cannot be compensated for because of its randomness, and is therefore of concern. The random variation of the gyroscope bias, computed over specified finite sample time and averaging time intervals, is referred to as the bias stability or instability, and is related to the noise build up in the sensor.

Bias instability of a gyroscope forms the fundamental limit that determines if the sensor is capable of navigation grade performance [65-68]. Lower bias instability means smaller angular e rror over time, and better overall heading accuracy of the inertial

navigation system. Typically, the accumulated error over time is corrected in the system by periodic calibration with an external reference, such as GPS [65]. However, it is desirable to limit communications with external references to prevent electronic jamming and reduce computational complexity. A gyroscope with low bias instability allows for longer time between calibrations. The analysis of the bias drift of a MEMS gyroscope offers insights into the inherent noise mechanisms in the sensor.

6.2 Allan Variance Technique

Bias drift is a function of the long-term average of the ZRO data, instead of a single data point. It is a statistical phenomenon that can be modeled by stochastic methods. Bias drift had been previously specified as a single Root-Mean-Square (RMS) number over time. However, this was a very conservative estimate, and did not offer any particular insight into the actual noise mechanisms. Subsequently, since bias drift is related to random noise in a system, the Power Spectral Density (PSD) was used to characterize it. The output of the gyroscope in the absence of any rotation input is recorded in the time domain, and Fourier Analysis yields the two-sided PSD ($S_\Omega(f)$).

A time-domain method that determines the angular error characteristics over time provides more insight for navigation applications, to determine the long-term stability of a gyroscope. One such method is the Allan Variance Technique, which has been used extensively to study drift, both in fiber-optic gyroscopes and Coriolis-based vibratory gyroscopes. This technique, developed in the 1960's by David Allan, is a time-domain (TD) analysis, which was initially introduced to study frequency stability of oscillators [69]. It aids in understanding the underlying random processes that give rise to data noise,

and also enables identification of each noise term in the collected data. The Allan Variance Method relies on the principle that each noise component has its own characteristic PSD, and thereby is able to correlate each random component based on a specific averaging time. Currently, the Allan Variance Technique is used as the standard for drift characterization in MEMS gyroscopes [7].

6.3 Computing the Allan Variance

The Allan Variance is defined as follows: the quantity expressed by one half the mean value of the square of the difference of adjacent time averages from a time series as a function of averaging time [70] and is expressed mathematically as

$$\sigma^2(\tau) = \frac{1}{2(n-1)} \sum_i (y(\tau)_{i+1} - y(\tau)_i)^2 \tag{6.1}$$

where $\sigma(\tau)$ is the root Allan Variance as a function of averaging time τ, n is the total number of data clusters, and y_i is the average value of the measurement in cluster i.

The procedure to compute the root Allan Variance consists of repeatedly averaging the data over varying clustering/bin times. The iterative procedure to compute Allan Variance can be summarized as follows:

1) Data Collection: The ZRO from the CVG is sampled at a specified sampling interval (τ_0) for a given period of time, which is at least a few hours at constant temperature to gain any meaningful information.
2) Data Clustering: The long sequence of data is divided into finite clusters based on an averaging time, τ (an integer multiple of the initial sampling interval τ_0).

3) Data Averaging: All the data points in each cluster are summed up and averaged over the length of that cluster.

4) Variance Computation: The difference of the averages in successive clusters is evaluated and squared. The values are then summed up and divided by the rescaling factor. The square root of this result provides a quantitative measure of how much the average has changed at that particular value of averaging time. This term is referred to as the Allan Deviation or root Allan Variance.

5) Repeated Averaging: The final step of the calculation involves revisiting the ZRO data and increasing the τ, and repeating steps 1 through 4. The final cluster length should be at least 10 times the original one.

The Allan Variance can be computed from the PSD of the collected data [70], as given by

$$\sigma_{\Omega}^{2}(\tau) = 4\int_{0}^{\infty} S_{\Omega}(f)\frac{sin^{4}(\pi f\tau)}{(\pi f\tau)^{2}} \tag{6.2}$$

This can be interpreted as the Allan Variance being directly proportional to the output noise power of the gyroscope when the output is passed through a filter with a transfer function $\sin^4(\pi f\tau)/(\pi f\tau)^2$. This particular transfer function arises due to the nature of the process used for computing the Allan Variance, i.e., the data clustering and averaging. The filter bandwidth depends on the sampling time τ. Therefore, by varying τ, different types of random processes, and therefore different properties associated with the noise, can be evaluated.

6.4 Noise Components in CVGs

The values of the root Allan Variance of the ZRO data are plotted as a function of the averaging time τ. Fig. 6.1 is adapted from [70] and plots the typical Allan Variance Curve of a CVG. The time-domain data from the CVG contains contributions from various noise terms. It has been observed and verified that the noise terms are correlated with different averaging times, and hence correspond to different portions on the Allan Variance curve. The Allan Variance curve allows for easy identification of the various random processes that exist in the gyroscope output, and is therefore preferred for CVG drift analysis.

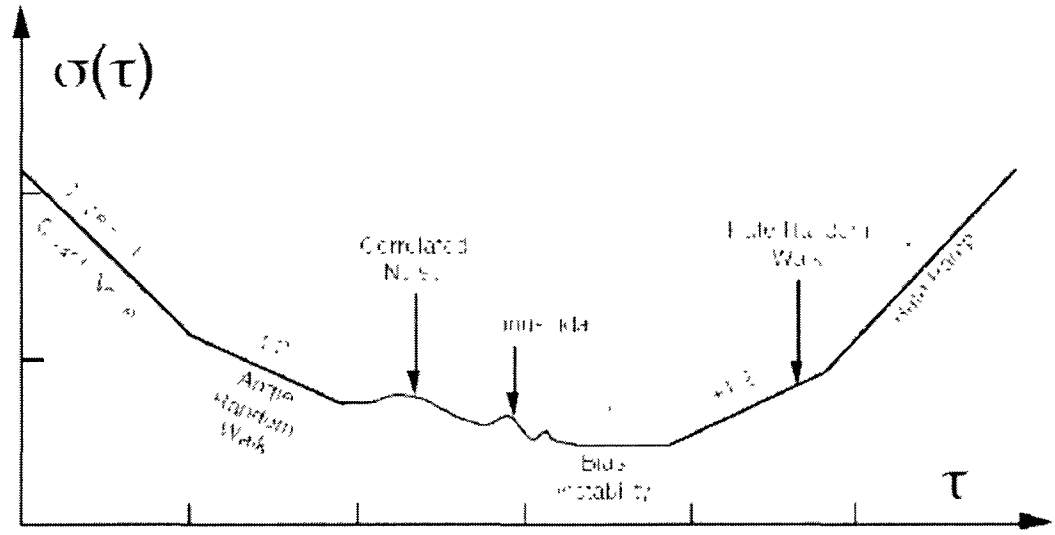

Figure 6.1: Sample plot of Allan variance analysis highlighting sections of the graph that correspond to various noise sources

It is observed in Fig. 6.1 that there are four distinct regions along the Allan Variance curve, which correspond to the following noise terms:

1. Quantization Noise

2. Angle Random Walk (ARW)

3. Bias Instability

4. Rate Random Walk (RRW)

The random processes that contribute to these noise terms can be assumed to be uncorrelated (i.e., statistically independent). The total Allan Variance at a given sampling time τ can be obtained by the RMS sum of the magnitude of each of these components at that τ, as

$$\sigma^2_{Total}(\tau) = \sigma^2_{Quantization}(\tau) + \sigma^2_{ARW}(\tau) + \sigma^2_{Bias\ Instability}(\tau) + \sigma^2_{RRW}(\tau) \tag{6.3}$$

6.4.1 Quantization Noise

The quantization noise is one of the errors introduced into an analog signal by encoding it in digital form. This noise is caused by the small differences between the actual amplitudes of the points being sampled and the bit resolution of the analog-to-digital converter [71]. For a gyro output, the source of this noise is the sampling of the output to record the value of the bias over time. Since the sampling is at a relatively higher frequency than other gyro time constants, this noise term corresponds to small values of τ in the time domain. The angle PSD for such a process is given in [72] as

$$S_\theta(f) = \tau Q_N^2 \left[\frac{\sin(\pi f \tau)}{\pi f \tau}\right]^2 \tag{6.4}$$

where Q_N is the quantization noise coefficient. Its theoretical limit is set to S/√12 [73], where 'S' is the gyroscope scale-factor. The rate PSD is related to the angle PSD (by differentiation process) through the following

$$S_\Omega(f) = (2\pi f)^2 S_\theta(f) = \frac{4Q_N^2}{\tau}\sin^2(\pi f \tau) \tag{6.5}$$

Substituting Eq. 6.5 into Eq. 6.2 and performing the necessary integration yields

$$\sigma^2_{Quantization}(\tau) = \frac{3Q_N^2}{\tau^2} \tag{6.6}$$

Therefore the root Allan Variance of the quantization noise when plotted in the log-log scale is represented by a slope of -1. The quantization noise has a short correlation time (i.e. high frequency). Since the high-frequency noise can usually be filtered out because of low bandwidth of the vehicular motion in most applications, it is not considered a major source of error/concern [74].

6.4.2 Angle Random Walk

The Angle Random Walk (ARW) is a result of integrating a wideband rate PSD noise. It is a measure of the angular error build up with time that is due to white noise in angular rate. In CVGs, the source of this noise is the Brownian motion of the mec hanical structure. This component corresponds to the flat region of the PSD plot in the frequency domain because it is white. The associated PSD for wideband rate noise can be represented as

$$S_\Omega(f) = N^2 \tag{6.7}$$

where N is the angle random walk coefficient usually expressed in °/hr/√Hz. Substituting Eq. 6.7 into Eq. 6.2 and performing the appropriate integration yields

$$\sigma_{ARW}^2(\tau) = \frac{N^2}{\tau} \tag{6.8}$$

Therefore the root Allan Variance of the ARW when plotted in the log-log scale is represented by a slope of -0.5. The numerical value of N can be obtained by fitting a -0.5 slope line to the portion of the root Allan Variance plot that varies as a function of $\tau^{-0.5}$, and reading its value at τ = 1s. N/60 gives the magnitude of the ARW component in the gyroscope output, yielding a measure of the total white noise. This noise error term is typically expressed in °/√hr and is an accurate indicator of the short-term stability of the system. Often, the ARW is converted to noise density by multiplying its value by 60 (Eq. 2.5), and expressed in °/hr/√Hz. The noise density refers to the TNEΩ of the vibratory gyroscope system and is commonly expressed in datasheets. Being a measure of short-term system stability, the ARW is significant at start-up, as it can prevent the initial biases of the system from being measured accurately.

Note that if the ARW is expressed in °/√s, it is equivalent to the unit of °/s/√Hz in noise density, without the multiplication of 60 needed.

6.4.3 Bias Instability

The origin of this noise is the electronics or other components that are susceptible to random flickering. Because of its low-frequency nature, it is indicated as the bias fluctuations in the data [75]. The rate PSD associated with this noise is known as the 1/f noise. By derivation, the bias instability value can be read on the root Allan Variance Plot

at the region where the slope is 0. The numerical value is the minimum value on the Allan Deviation Curve. Bias instability represents the minimum attainable bias drift of the vibratory gyroscope system (when sampled at the averaging time corresponding to the minimum of the root Allan Variance Curve). In data sheets, the minimum value of the Allan Variance Curve is quoted as the bias drift of the gyro.

6.4.4 Rate Random Walk

The Rate Random Walk (RRW) represents the drift-rate error build-up with time that is due to the white noise of the angular acceleration component in the vibratory gyroscope. The exact origin of this noise is still uncertain, but consists of random processes with very long correlation times. The rate PSD associated with this noise has a $1/f^2$ characteristic, and the Allan Variance corresponding to this noise term is given by

$$\sigma_{RRW}^2(\tau) = \frac{K^2}{3}\tau \tag{6.9}$$

where K is the Rate Random Walk coefficient. This indicates that RRW is represented by a slope of 0.5 on a log-log plot, where K is usually in $°/hr^2/\sqrt{Hz}$.

6.5 Bias Drift of the MB-TFG

The MB-TFG is locked into drive resonance using the electromechanical drive loop, and the Allan Variance analysis performed on the ZRO data provides a methodology to quantify its stability or instability over time. It must be noted that since the bias drift is a DC phenomenon, nonlinearity at large input rotation rates is not an issue. The DC value of the ZRO was sampled using an Agilent 34405A digital multimeter. The root Allan

Variance was computed for various sampling times, using the MATLAB code shown in Appendix A.

Fig. 6.2 shows the measured voltage output of a 30μm-thick SOI MB-TFG (Device #13 in Chapter 5), under a zero-rate input. This ZRO value, exhibiting a noise level of approximately 1mV peak-to-peak is sampled every 200ms for a period of about 3 hours.

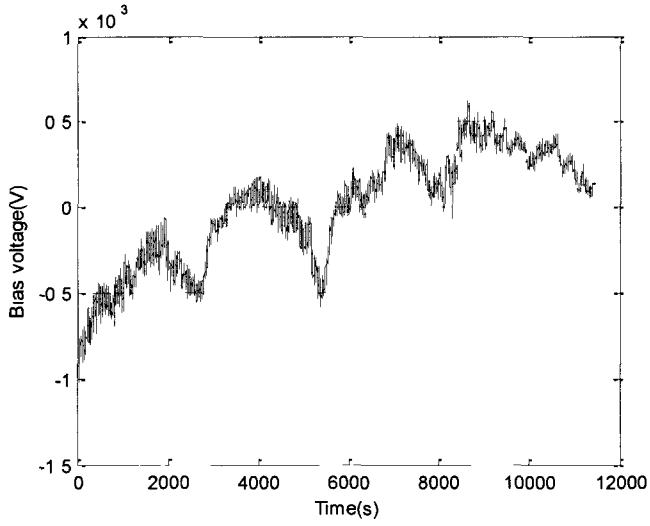

Figure 6.2: ZRO plot of Device #13 for a period of about 3 hours

The root Allan Variance Plot of this MB-TFG is then plotted in Fig. 6.3. In this figure, the -0.5 slope line fitted with the Allan Variance Curve at τ = 1s gives 400°/hr/√Hz, which corresponds to a measured noise floor of $9\mu V_{PP}/\sqrt{Hz}$. The output-referred total equivalent noise density (TNEΩ) of the gyroscope system is therefore 400°/hr/√Hz, and dividing this number by 60 yields the ARW of 6.67°/√hr, which reflects the white noise in the system. The bias drift of the system is given by the minimum of the Allan Variance Curve, which is 95°/hr in this case. The bias instability is expected to be greatly reduced

by employing integrated interface electronics with flicker (1/f) noise suppression techniques.

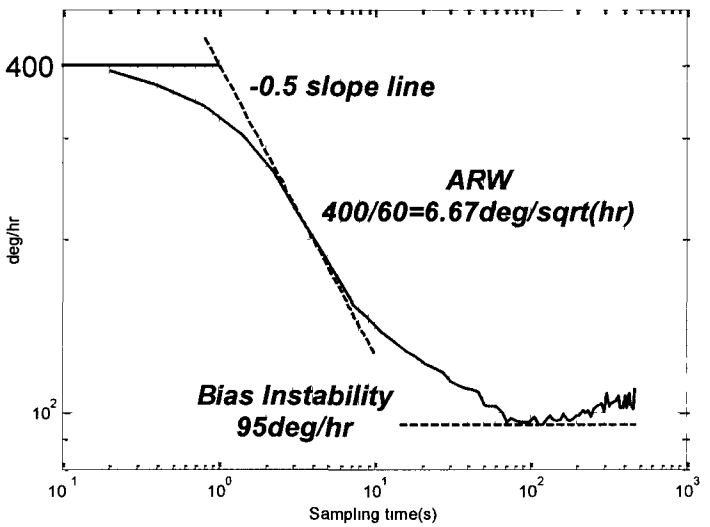

Figure 6.3: Root Allan Variance Plot of the MB-TFG (Device #13)

From these measurement results, it can be seen that this MB-TFG is still a rate grade gyroscope, according to Table 1.1. The performance of this MB-TFG is also compared with other research work, as shown in Table 6.1.

Table 6.1: Comparison of this MB-TFG and other reported TFGs

	This work	**TFG [38] (2010)**	**TFG [20] (2009)**	**TFG [37] (2009)**	**TFG [17] (2008)**	**TFG [39] (2007)**
Sensitivity (mV/°/s)	0.08	17.8	0.131	0.028	83	2.4
ARW (°/√hr)	6.67	1.2	1.15	5.4	0.007	0.6
Bias drift (°/hr)	95	180	131	288	0.15	25200

To better understand how noise sources with different spectral characteristics are mapped onto the root Allan Variance Plot, considering that in a typical noise spectrum, the flicker noise from electronics is a low-frequency phenomenon and dominates low-frequency regions, while higher frequency regions are dominated by the white noise from other sources (mechanical thermal noise). On the root Allan Variance Plot, at regions where the sampling time τ is short, the ZRO signal can be regarded as a "high frequency" signal, thus the ARW extracted from these regions is strongly related to the white noise in the system; at regions where τ is longer, the ZRO signal can be regarded as a "low frequency" signal, therefore the bias instability observed from these regions is correlated with the amount of flicker noise in the system.

The bias drift is closely related to the sensitivity and bandwidth of the gyroscope. As shown from the experimental work in [76], bias drift varies inversely with sensitivity. Therefore, smaller bandwidth leads to higher sensitivity and lower bias drift. In addition, lowering the total system noise floor by a larger mass, increasing the effective quality factor and the capacitive sensitivity of the sensor, and techniques to reduce the flicker noise all result in an improved bias stability.

CHAPTER VII

CONCLUSIONS AND FUTUER WORK

7.1 Summary of Research Project

This dissertation has focused on the design, fabrication, and performance evaluation of a MEMS Coriolis Vibratory Gyroscope (CVG) based on SOI wafers. A list of the technical contributions made through this research project is summarized as follows:

(1) Design and Development of the Multiple-Beam Tuning-Fork Gyroscope (MB-TFG): the MB-TFG relies on the Coriolis Effect to transfer energy between two in-plane operation modes – the drive-mode and the sense-mode. The drive-mode vibration is excited using a pair of comb-drive electrodes to apply electrostatic force on the proof-masses. When subject to a rotation rate about the out-of-plane z-axis, the sense-mode vibration is excited and can be detected from a capacitive output. The design of the Multiple-Beam Tuning-Fork Structure (MB-TFS) is based on a numerical model of the Thermo-Elastic Damping (TED), to ensure high quality factors (Qs) in both operation modes. A comprehensive theoretical analysis of the MB-TFG design is conducted to relate the design parameters to its operation parameters and further performance parameters. The MB-TFG prototypes were fabricated on 30μm-thick Silicon-On-Insulator (SOI) substrate using a simple one-mask fabrication process.

(2) Mask design improvement to enhance Qs in both modes: the fabrication process involves two steps – DRIE and HF acid etching. The original mask design

induced much anchor loss that greatly reduced the Q values, basically because of the over-etching of the silicon dioxide underneath the anchor during the HF acid etching step. An improved mask design defines the MB-TFG devices through a trench feature, which limits the exposure of the silicon dioxide to the HF acid, thus alleviating the severe fabrication effect on anchor loss and significantly increasing the Q values. The DRIE step was done at Cornell's Nanofabrication Facility (CNF) using PT770 etcher and the HF acid etching step was performed at Micro Devices and Micromechanics Laboratory of Old Dominion University. The 30μm-thick high-Q devices were fabricated with an optimal HF acid etching time that was determined through repetitive experiments.

(3) Interface electronics design and implementation for operating the high-Q MB-TFG in vacuum: an electromechanical drive loop based on the Barkhausen's Criteria for self-oscillation is designed and implemented on Printed-Circuit-Board (PCB) level, to start up and sustain oscillations along the drive axis of the MEMS structure. A synchronous phase sensitive demodulation technique, which is capable of rejecting the quadrature error, is implemented for sensing the input rotation rate. When operating the gyroscope, the DC polarization voltage applied on the MB-TFS is adjusted to reduce the sense-mode resonant frequency in order to achieve an almost matched-mode condition (4Hz frequency split at 16.8kHz). The matched-mode condition is highly desirable since the circuit and system developed in this research leverage on the inherently high mechanical gain (Q) of the coupled resonant systems, and the effective Q is maximized when the operation modes are completely matched in frequency. High Qs in both modes

benefit the sensor performance in many aspects such as high resolution, high sensitivity and low bias drift.

(4) Transimpedance Amplifier (TIA) front-end design for motional current detection from the MB-TFG: the TIA has been chosen as the low-noise front-end that is interfaced with the MB-TFG. It also minimizes the Q-loading effect in the drive loop. The input-referred current noise of the TIA is measured to be as low as $1.4pA/\sqrt{Hz}$, which corresponds to a minimum detectable capacitance of $0.46aF/\sqrt{Hz}$. The feedback resistance of this TIA is in the range of 1 – 5MΩ, while the following Variable Gain Amplifier (VGA) can increase the overall TIA gain in the drive loop to over 20MΩ. Comparing to the T-network-based TIA in [3], where the large TIA gain is realized on a single stage, this work has more flexibility in the gain tuning to meet the self-oscillation need in the drive loop.

(5) Performance characterization of the assembled MB-TFG system: the fabricated MB-TFG devices are first measured for their frequency response in order to observe the resonant frequencies and Q values of both operation modes. The measured resonant frequency is around 16 – 17kHz and the measured highest Qs are over 200k for the drive-mode and 100k for the sense-mode. To operate this MB-TFG, the polarization voltage is adjusted so that a minimum frequency difference of 4Hz is achieved between the drive-mode and sense-mode, at a center frequency of 16.8kHz. The effective Q of the gyroscope is around 90k. Using the PCB level interface electronics, the rate sensitivity is measured to be $80\mu V_{PP}/°/s$, with an equivalent TIA gain of about 6MΩ. Finally, the bias drift phenomenon is

investigated. The impact of different noise sources such as flicker noise and white noise on the bias drift behavior of a MEMS gyroscope is modeled and analyzed. A time-domain analysis of the Zero Rate Output (ZRO) data using the Allan Variance Technique is described in detail. The measured Angle Random Walk (ARW) and bias drift of the MB-TFG system are 6.67°/√hr and 95°/hr, respectively.

7.2 Future Work

Through the study and analysis in this work, several paths can be followed to improve and optimize the performance of this gyroscope. These possible future directions are briefly discussed.

(1) Quadrature error minimization: the quadrature error in the output signal from the sense channel can be really large, according to Eq. 2.30. Although in this work, the quadrature error signal has been rejected by the phase sensitive demodulation technique, it still hinders a perfect mode-matching (0Hz frequency split), thus decreasing the effective Q and degrading the system performance. Therefore, electrostatic electrodes dedicated to the minimization of the quadrature error can be added into the MB-TFG design. Note that the usage of these electrodes must not interfere with the electrostatic frequency tuning of the sense-mode frequency, so they should be included in the form of the comb-drive electrode used in the drive-mode. These electrodes were incorporated in [3] and helped achieve a perfect mode-matching condition that led to a high-precision mode-matched tuning fork gyroscope.

(2) Bandwidth increase: the bandwidth of the gyroscope is a function of the mode separation as well as the inherent quality factor of the resonant modes. Since the bandwidth of this MB-TFG is only a few Hz, techniques for increasing the bandwidth are necessary.

The electrical way is by Q-loading, which involves electronically loading the quality factor of the gyroscope in mode-matched condition. Q-loading decreases the Q_{EFF} but maintains the gyroscope in mode-matched condition. Since the BW is inversely proportional to Q_{EFF} and Q_{EFF} is lowered without frequency change, then bandwidth is increased. Electronic Q-loading can be achieved by varying the input impedance of the TIA front-end that the micromechanical device sees, according to Eq. 4.4. By providing an alternate feedback path, the normally low input impedance provided by the shunt-shunt feedback can be increased, thereby loading the quality factor.

The mechanical way is to design a micromechanical structure with two frequency peaks in the sense-mode, as shown in [37]. With the drive-mode peak right in between the two sense-mode peaks, the bandwidth is increased. The drawback in this design is a very complicated structure.

(3) Sensitivity increase: in this work, the output motional current in the sense-mode is from a group of four parallel-plate sense electrodes that are of the same nature – their sense capacitive gap increases or decreases at the same time. The other group of four sense electrodes, by comparison, has an opposite nature in that their sense capacitive gap change is in opposite direction as to that of the first group. Noting this, we can take advantage of the differential nature of the motional

currents that are generated from these two groups of sense electrodes. By using an instrumentation amplifier, the rate sensitivity of the system can be doubled, as shown in [21]. The duty of frequency tuning for the other group of sense electrodes can be relieved because the polarization voltage alone is enough for fulfilling this purpose.

(4) Reduction in power consumption: since this work is done using a discrete-level system with on-shelf electrical components, the power consumption is high. With the same circuit principle, the interface electronics can go to an integrated level, which will reduce the power consumption significantly.

REFERENCES

[1] A. Burg, *et al.*, "MEMS Gyroscopes and their Applications."

[2] N. Yazdi, *et al.*, "Micromachined Inertial Sensors," *Proceedings of the IEEE,* vol. 86, pp. 1640-1659, 1998.

[3] A. Sharma, "CMOS Systems and Circuits for Sub-degree per Hour MEMS Gyroscopes," Ph. D. dissertation, Georgia Institute of Technology, 2007.

[4] A. Lawrence, *Modern Inertial Technology*. New York: NY: Springer-Verlag, 1993.

[5] "IEEE Standard for Inertial Sensor Terminology," *IEEE,* 2001.

[6] S. Nasiri, "A Critical Review of MEMS Gyroscopes Technology and Commercialization Status," InvenSense.

[7] "IEEE Standard Specification Format Guide and Test Procedure for Coriolis Vibratory Gyros," *IEEE,* 2004.

[8] "GG1320AN Digital Laser Gyro," Honeywell 2007.

[9] "GG5300 Three Axis MEMS Rate Gyro," Honeywell 2006.

[10] M. Weinberg and A. Kourepenis, "Error Sources in In-Plane Silicon Tuning-Fork MEMS Gyroscopes," *Journal of Microelectromechanical Systems,* vol. 15, pp. 479-491, 2006.

[11] J. Bernstein, *et al.*, "A Micromachined Comb-drive Tuning Fork Rate Gyroscope," in *Proceedings of IEEE MEMS 1993, An Investigation of Micro Structures, Sensors, Actuators, Machines and Systems*, Fort Lauderdale, FL, pp. 143-148, 1993.

[12] M. Weinberg, *et al.*, "Microelectromechanical Instrument and Systems Development at the Charles Stark Draper Laboratory, Inc," in *AIAA/IEEE 16th Digital Avionics Systems Conference (DASC)*, Irvine, CA, pp. 8.5-33-40, 1997.

[13] J. Geen, *et al.*, "Single-Chip Surface-Micromachined Integrated Gyroscope with 50 deg/hr root Allan Variance," in *Digest of Technical Papers, 2002 IEEE International Solid-States Circuits Conference (ISSCC)*, San Francisco, CA, pp. 426-427, 2002.

[14] A. Sharma, *et al.*, "A High-Q In-Plane SOI Tuning Fork Gyroscope," in *Proceedings of IEEE, Sensors, 2004*, pp. 467-470, 2004.

[15] M. Zaman, *et al.*, "High Performance Matched-Mode Tuning Fork Gyroscope," in *IEEE 19th International Conference on MEMS 2006*, Istanbul, Turkey, pp. 66-69, 2006.

[16] A. Sharma, *et al.*, "A 0.1 deg/hr Bias Drift Electronically Matched Tuning Fork Microgyroscope," in *IEEE 21st International Conference on MEMS 2008*, Tucson, AZ, pp. 6-9, 2008.

[17] M. Zaman, *et al.*, "A Mode-Matched Silicon-Yaw Tuning-Fork Gyroscope with Subdegree-Per-Hour Allan Deviation Bias Instability," *Journal of Microelectromechanical Systems,* vol. 17, pp. 1526-1536, 2008.

[18] R. Wang, *et al.*, "A SOI-based Tuning-Fork Gyroscope with High Quality Factors," in *SPIE Conference, Sensors and Smart Structures Technologies for Civil, Mechanical, and Aerospace Systems*, San Diego, CA, 2009.

[19] A. Trusov, *et al.*, "Micromachined Rate Gyroscope Architecture with Ultra-high Quality Factor and Improved Mode Ordering," *Sensors and Actuators A: Physical,* 2010.

[20] K. Sahin, *et al.*, "A Wide-Bandwidth and High-Sensitivity Robust Microgyroscope," *Journal of Micromechanics and Microengineering,* vol. 19, pp. 1-8, 2009.

[21] A. Sharma, *et al.*, "A 104-dB Dynamic Range Transimpedance-Based CMOS ASIC for Tuning Fork Microgyroscopes," *IEEE Journal of Solid-State Circuits,* vol. 42, pp. 1790-1802, 2007.

[22] W. Watson and T. Henke, "Coriolis Gyro Configuration Effects on Noise and Drift Performance," in *Gyro Symposium*, Stuttgart, Germany, pp. 927-935, 2002.

[23] M. W. Putty, "A High Aspect-Ratio High-Performance Polysilicon Vibrating Ring Gyroscope," Ph. D. dissertation, University of Michigan, 2000.

[24] S. D. Senturia, *Microsystem Design*: Kluwer Academic Publishers, 2001.

[25] C. T. C. Nguyen and R. T. Howe, "An Integrated CMOS Micromechanical Resonator High-Q Oscillator," *IEEE Journal of Solid-State Circuits,* vol. 34, pp. 440-455, 1999.

[26] W. A. Clark, "Micromachined Vibratory Rate Gyroscopes," Ph.D. dissertation, University of California, Berkeley, 1997.

[27] M. Zaman, *et al.*, "The Resonating Star Gyroscope," in *IEEE International Conference on Micro ElectroMechanical Systems, (MEMS'05)*, Miami, FL, pp. 355-358, 2005.

[28] F. Ayazi and K. Najafi, "A HARPSS Polysilicon Vibrating Ring Gyroscope," *IEEE Journal of Microelectromechanical Systems,* vol. 10, pp. 169-179, 2001.

[29] W. C. Tang, *et al.*, "Electrostatically Balanced Comb Drive for Controlled Levitation," in *Tech. Digest of Solid-State Sensors, Actuators and Microsystems Workshop, 1990*, Hilton Head Island, SC, pp. 23-27, 1990.

[30] M. Zaman, *et al.*, "Towards Inertial Grade Vibratory Microgyros: A High-Q In-Plane Silicon-On-Insulator Tuning Fork Device," in *Tech. Digest of Solid-State Sensors, Actuators and Microsystems Workshop, 2004*, Hilton Head Island, SC, pp. 384-385, 2004.

[31] Z. Hao, *et al.*, "Energy Loss Mechanisms in a Bulk-Micromachined Tuning Fork Gyroscope," in *Proc. of 5th IEEE Conference on Sensors, Sensors' 06*, Daegu, S. Korea, pp. 1333-1336, 2007.

[32] R. Wang, *et al.*, "A Multiple-Beam Tuning-Fork Gyroscope with High Quality Factors," *Sensors and Actuators A: Physical,* 2011.

[33] I. Prikhodko, *et al.*, "Foucault Pendulum on a Chip: Angle Measuring Silicon MEMS Gyroscope," in *IEEE MEMS 2011*, Cancun, Mexico, 2011.

[34] S. Zotov, *et al.*, "Frequency Modulation Based Angular Rate System," in *IEEE MEMS 2011*, Cancun, Mexico, 2011.

[35] A. Trusov, *et al.*, "Ultra-High Q Silicon Gyroscopes with Interchangeable Rate and Whole Angle Modes of Operation," in *IEEE Sensors 2010 Conference* Waikoloa, Hawaii, 2010.

[36] A. Trusov, *et al.*, "Vacuum Packaged Silicon MEMS Gyroscope with Q-Factor above 0.5 Million," in *IMAPS 6th International Conference and Exhibition on Device Packaging*, Scottsdale, AZ, 2010.

[37] A. Trusov, *et al.*, "Performance Characterization of A New Temperature-Robust Gain-Bandwidth Improved MEMS Gyroscope Operated in Air," *Sensors and Actuators A: Physical,* vol. 155, pp. 16-22, 2009.

[38] Z. Guo, *et al.*, "A Lateral-Axis Microelectromechanical Tuning-Fork Gyroscope With Decoupled Comb Drive Operating at Atmospheric Pressure," *Journal of Microelectromechanical Systems,* vol. 19, pp. 458- 468, 2010.

[39] S. Alper, *et al.*, "A High-Performance Silicon-On-Insulator MEMS Gyroscope Operating at Atmospheric Pressure," *Sensors and Actuators A: Physical,* vol. 135, pp. 34-42, 2007.

[40] H. Mendez, "Silicon-On-Insulator - SOI Technology and Ecosystem - Emerging SOI Applications," 2009.

[41] *MEMS Technology*. Available: http://www.memx.com/technology.htm

[42] Y. Xu, *et al.*, "Numerical models and experimental investigation of energy loss mechanisms in SOI-based tuning-fork gyroscopes," *Sensors and Actuators A: Physical,* vol. 152, pp. 63-74, 2009.

[43] F. Ayazi and K. Najafi, "High Aspect-Ratio Combined Poly and Single-Crystal Silicon (HARPSS) MEMS Technology," *Journal of Microelectromechanical Systems,* vol. 9, pp. 288-294, 2000.

[44] M. Lemkin, *et al.*, "A 3-axis Surface Micromachined Sigma-Delta Accelerometer," in *Digest of Technical Papers IEEE International Solid-State Circuits Conference, (ISSCC'97)*, San Francisco, CA, pp. 202-203, 1997.

[45] B. Amini and F. Ayazi, "A 2.5-v 14-bit CMOS SOI Capacitive Accelerometer," *IEEE Journal of Solid-State Circuits,* vol. 39, pp. 2467-2476, 2004.

[46] X. Jiang, *et al.*, "A Monolithic Surface Micromachined Z-axis Gyroscope with Digital Output," in *Digest of Technical Papers Symposium on VLSI Circuits, 2000*, Honolulu, HI, pp. 16-19, 2000.

[47] V. Petkov and B. Boser, "A Fourth-order Interface for Micromachined Inertial Sensors," *IEEE Journal of Solid-State Circuits,* vol. 40, pp. 1602-1609, 2005.

[48] C. T. Nguyen, "Micromechanical Signal Processors," Ph.D. dissertation, University of California, Berkeley, 1994.

[49] P. R. Gray, *et al.*, *Analysis and Design of Analog Integrated Circuits*. Hoboken, NJ: Wiley, 2001.

[50] T. Gabrielson, "Mechanical-Thermal Noise in Micromachined Acoustic and Vibration Sensors," *IEEE Trans. Electron Devices,* vol. 40, pp. 903-909, 1993.

[51] S.-H. C. Paik, "A Mems-based Precision Operational Amplifier," Masters of Engineering, Department of Electrical Engineering and Computer Science, Massachusetts Institute of Technology, Cambridge, MA, 2004.

[52] J. S. Shafran, "A MEMS-based High-Resolution Electric-Field Meter," Masters of Engineering, Department of Electrical Engineering and Computer Science, Massachusetts Institute of Technology, Cambridge, MA, 2005.

[53] A. A. Aina, "High Performance Amplifier Topologies Implemented with a Micro-Machined Vibrating Capacitor," Ph.D. thesis, Department of Electrical Engineering and Computer Science, Massachusetts Institute of Technology, Cambridge, MA, 2003.

[54] "HC4046 Phase Locked Loop," ON Semiconductor.

[55] S. Lee and C. T. C. Nguyen, "Influence of Automatic Level Control on Micromechanical Resonator Oscillator Phase Noise," in *Proceedings of the 2003 IEEE International Frequency Control Symposium and PDA Exhibition Jointly with the 17th European Frequency and Time Forum*, pp. 341-349, 2003.

[56] P. Horowitz and W. Hill, *The Art of Electronics*, 2nd ed. Cambridge: Cambridge University Press, 1989.

[57] *Precision Rectifier*. Available: http://en.wikipedia.org/wiki/Precision_rectifier

[58] *Op Amp Precision Half-wave Rectifier*. Available: http://www.ecircuitcenter.com/Circuits/op_HW_recitifier/Op_HW_Rectifier.htm

[59] *Difference Amplifier*. Available: http://hyperphysics.phy-astr.gsu.edu/HBASE/Electronic/opampvar6.html#c1

[60] *Sallen-Key Topology*. Available: http://en.wikipedia.org/wiki/Sallen%E2%80%93Key_topology

[61] J. H. Harlow, *Electric Power Transformer Engineering*: CRC Press, 2004.

[62] M. H. Tooley, *Electronic Circuits: Fundamentals and Applications*: Newnes, 2006.

[63] *Q factor*. Available: http://en.wikipedia.org/wiki/Q_factor#cite_note-1

[64] Z. Hao, *et al.*, "A Thermal-Energy Method for Calculating Thermoelastic Damping in Micromechanical Resonators," *Journal of Sound and Vibration,* pp. 822-870, 2009.

[65] B. Hofmann-Wellenhof, *et al.*, *Navigation, Principles of Positioning and Guidance*: Springer, 2003.

[66] G. Beck, *Navigation Systems*: Van Nostrand Reinhold, 1979.

[67] C. Lin, *Modern Navigation, Guidance, and Control Processing*: Prentice-Hall, 1991.

[68] O. Woodman, "An Introduction to Inertial Navigation," University of Cambridge, 2007.

[69] D. Allen, "Statistics of Atomic Frequency Standards," in *Proceedings of IEEE*, pp. 221-230, 1966.

[70] "IEEE Standard Specification Format Guide and Test Procedure for Single-Axis Laser Gyros," *IEEE,* 1995.

[71] *Quantization Error*. Available: en.wikipedia.org/wiki/Quantization_error

[72] J. Papoulis, *Probability, Random Variables, and Stochastic Processes*: McGraw-Hill, 1991.

[73] N. El-Sheimy, *et al.*, "Analysis and Modeling of Inertial Sensors using Allan Variance," *IEEE Transactions on Instrumentation and Measurement,* vol. 57, pp. 140-149, 2008.

[74] H. Hou, "Modelling Inertial Sensors Errors using Allan Variance," Masters Thesis, University of Calgary, 2004.

[75] M. S. Keshner, "1/f Noise," *Proc. IEEE,* vol. 70, pp. 212-218, 1982.

[76] A. Sharma, *et al.*, "A Sub-0.2deg/ hr Bias Drift Micromechanical Silicon Gyroscope With Automatic CMOS Mode-Matching " *IEEE Journal of Solid-State Circuits,* vol. 44, pp. 1593-1608, 2009.

APPENDIX A

BIAS DRIFT MEASUREMENT

MATLAB code used for Allan Variance computation

```
clear ;
close ;
format      ;
sig2=[];
tau=[];
D=[];
vavg=[];
vavg_mean=[];
zro=[];
bin_size=0;

vavg_all=load('                                                    ');
vavg_raw=vavg_all(:,2);


                    ,'    ',' ',


vavg_mean=vavg_raw(1:end)-mean(vavg_raw(1:end));
sens=2.2e-8;
zro=vavg_mean./sens;
n=length(zro);
tau0=0.2;
total_time=n*tau0;
ctr=1;
scale=0.1;
bin_size=1;
while bin_size<floor((n/25)*tau0);
    fprintf(' ');
    m=10*scale;
    bin_size=m*tau0;
    tau(ctr)=bin_size;
    for i=0:floor(n/m)-1
        bin_ave(ctr,i+1)=mean(zro((1+round(m)*i):(i+1)*round(m)));
    end;
    ctr=ctr+1;
    scale=scale+(ctr-1)*0.1;
end;

n_tau=length(tau);
for i=1:n_tau
    diff_bin=bin_ave(i,:);
    diff_bin_sqr=(diff(diff_bin)).^2;
    diff_bin_ms=(0.5)*mean(diff_bin_sqr);
    sig2(i)=sqrt(diff_bin_ms);
```

```
end;
save '
   ;



t_seconds=tau0*(1:n);
figure(1);
plot(t_seconds,vavg_mean,'-
hold   ;
grid   ;
xlabel('
ylabel('
figure(2);
loglog(tau,sig2,'-
hold   ;
grid   ;
x=0.8:0.1:10;
y=400*x.^(-0.5);
loglog(x,y,'--
xlabel('
ylabel('

bias_drift=min(sig2);
```

VITA

Ren Wang received his B.S. and M.S. degrees in Electrical Engineering from Wuhan University, China and Delft University of Technology, Netherlands, in 2004 and 2006, respectively. He is currently a Ph.D. candidate in the Department of Mechanical Engineering, Old Dominion University, Norfolk, USA. His research interests are developing MEMS sensors and designing their associated interface circuits.